SYNTHESIS AND DEVELOPMENT OF $Sm_2SrAl_2O_7$ BASED AIR PLASMA SPRAYED CERAMIC THERMAL BARRIER COATINGS: OXIDATION, HOT CORROSION AND HIGH TEMPERATURE EROSION STUDY

Thesis

Submitted in partial fulfillment of the requirements for the degree of

DOCTOR OF PHILOSPHY

by

BASKARAN T

(145059 MT14F02)

DEPARTMENT OF METALLURGICAL AND MATERIALS ENGINEERING
NATIONAL INSTITUTE OF TECHNOLOGY KARNATAKA,
SURATHKAL, MANGALURU - 575025
APRIL, 2018

D E C L A R A T I O N

I hereby *declare* that the Research Thesis entitled "**Synthesis and Development of $Sm_2SrAl_2O_7$ Based Air Plasma Sprayed Ceramic Thermal Barrier Coatings: Oxidation, Hot Corrosion and High Temperature Erosion Study**", which is being submitted to the National Institute of Technology Karnataka, Surathkal in partial fulfillment of the requirements for the award of the Degree of **Doctor of Philosophy in the Department of Metallurgical and Materials Engineering**, is a *bonafide report of the research work carried out by me*. The material contained in this Research Thesis has not been submitted to any University or Institution for the award of any degree.

Place: NITK, Surathkal

Date:

Name: **BASKARAN T**

Register Number: **145059 MT14F02**

Department of Metallurgical and

Materials Engineering

CERTIFICATE

This is to certify that the Research Thesis entitled "**Synthesis and Development of $Sm_2SrAl_2O_7$ Based Air Plasma Sprayed Ceramic Thermal Barrier Coatings: Oxidation, Hot Corrosion and High Temperature Erosion Study**", submitted by **Mr. Baskaran T (Register Number: 145059 MT14F02)** as the record of the research work carried out by him, is *accepted as the Research Thesis submission* in partial fulfillment of the requirements for the award of degree of Doctor of Philosophy.

Research Guide
Dr. Shashi Bhushan Arya
Assistant Professor
Department of Metallurgical and
Materials Engineering
NITK, Surathkal

Chairman-DRPC

Date:

ACKNOWLEDGEMENTS

It is with great and profound sense of gratitude I thank my guide **Dr. Shashi Bhushan Arya,** Assistant professor, Department of Metallurgical and Materials Engineering, NITK, Surthkal for his valuable guidance, excellent research supervision and valuable discussions throughout my research work.

I am especially indebted to **Dr. Udaya Bhat K,** Associate professor and Head, **Dr. Jagannath Nayak,** Ex Head, Department of Metallurgical and Materials Engineering, NITK, Surathkal for allowing me to use the necessary facilities in the department.

I express my gratitude to my RPAC members **Dr. Nityananda Shetty**, Department of chemistry and **Dr. Jagannath Nayak,** Ex Head, Department of Metallurgical and Materials Engineering, NITK, Surathkal, for their valuable suggestions and comments during the research work.

I would like to thank the **Ministry of Human Resources Development (MHRD)**, **Government of India**, for a research fellowship.

I wish to thank **M/s. Metallizing Equipment Co. Pvt. Ltd, Jodhpur**, India for coating the specimens.

I would like to thank the non-teaching staff of the Metallurgical and Materials Engineering department for their valuable help during the research work.

My special thanks to my parents and brother **Dr. T. Pandiyarajan** for their support and encouragement to complete this work. Finally, I acknowledge the encouragement and help received from all of my colleagues and friends.

BASKARAN T

ABSTRACT

Samarium Stronium Aluminate (SSA) ceramic oxide was synthesized by molten salt method and coated on a bond coat (NiCrAlY)/Inconel 718 superalloy by air plasma spray (APS) process. The pre-oxidation, oxidation, hot corrosion and high temperature erosion tests were conducted at elevated temperatures. The pre-oxidation study was carried out to examine the role of thermally grown oxide (TGO) thickness on the oxidation kinetics of thermal barrier coatings (TBCs). TGO thicknesses were controlled at different pre-oxidation times of 10, 20 and 30 h at 1050 ºC in the argon atmosphere, the highest TGO thickness being found for 30 h pre-oxidized samples. Among these three pre-oxidation times, 20 h pre-oxidized SSA TBCs showed 65% higher oxidation resistance as compared to conventional Yttria stabilized zirconia (YSZ) TBCs (20 h) after oxidation at 1100 ºC in air mainly due to the presence of highly enriched α-Al_2O_3 at the interface. Electrochemical impedance spectroscopy was carried out and it was noticed that the highest charge transfer resistance and lowest capacitance about 0.48×10^6 Ohm cm^2 and 1.1 nF cm^{-2} respectively were observed for 20 h of pre-oxidation. The impedance response was reduced significantly after oxidation at 1100 ºC for 10 h pre-oxidized specimen as compared to 20 and 30 h due to the compositional change of pure α-Al_2O_3 based TGO into more conductive $NiCr_2O_4$. The lowest diffusion coefficient, D_{Cr}^{3+} in the NiO lattice which reduced the formation of metal ion vacancies at the TGO-top coat interface caused to exhibit higher TGO resistance for 20 h pre-oxidized specimens over 10 and 30 h after oxidation at 1100 ºC. The hot corrosion resistance of SSA TBCs showed approximately 8-39% lower than conventional YSZ in hot corrosion environments of (i) 50 wt.% Na_2SO_4 + 50 wt.% V_2O_5 and (ii) 90 wt.% Na_2SO_4 + 5 wt.% V_2O_5 + 5 wt.% NaCl at 700 and 900˚C. The lower hot corrosion life of SSA TBCs was mainly due to the basicity of SrO. It is much higher than Sm_2O_3, Y_2O_3 and Al_2O_3, which indicates SrO has higher tendency followed by Sm_2O_3, Y_2O_3 and Al_2O_3 to react with molten salt at 700 and 900 ˚C. The high temperature erosion test was conducted in air jet erosion tester at an impingement angle of 30 and 90˚ for different testing temperatures of 200, 500, and 800 ˚C. The test was performed on pre-oxidized SSA and YSZ TBCs at 1050 ˚C for 10 h. The SSA TBCs exhibited 50% lower erosion resistance than conventional YSZ TBCs. The observed lower resistance is mainly due to the formation of mud-cracks during pre-oxidation treatment.

Keywords: Thermal barrier coatings, Oxidation, Electrochemical impedance spectroscopy (EIS), Hot corrosion, High temperature erosion

TABLE OF CONTENTS

LIST OF FIGURES

LIST OF TABLES

LIST OF ABBREVIATIONS

TBCs	Thermal barrier coatings
REs	Rare earths
CTE	Coefficient of thermal expansion
TGO	Thermally grown oxide
APS	Air plasma spray
EB-PVD	Electron beam physical vapor deposition
HVOF	High velocity oxy fuel
YSZ	Yttria stabilized zirconia
t-Zirconia	Tetragonal zirconia
m-Zirconia	Monoclinic zirconia
XRD	X-ray diffractometer
SEM	Scanning electron microscope
FE-SEM	Field emission scanning electron microscopy
EDX	Energy dispersive x-ray spectroscopy
XPS	X-ray photoelectron spectroscopy
SSA	Samarium strontium aluminate
EIS	Electrochemical impedance spectroscopy

CHAPTER 1

INTRODUCTION

Thermal barrier coatings (TBCs) are typically ceramic oxide materials which are applied over the hot gas flow regions of combustors cans, vane platforms in aero engines and land based gas turbines (Padture et al. 2002). Total TBC system is a mixture of metallic bond coat (MCrAlY type) and ceramic top coat (e.g. Yttria Stabilized Zirconia-YSZ) on the superalloy substrate. Formation of thermally grown oxide (TGO) takes place at the interface between the top coat and metallic bond coat due to the presence of enrich oxygen at higher temperature (Chen et al. 2008). The ceramic top coat material play a vital role on the formation of Al_2O_3 based TGO at the interface. During thermal cycles, the mechanical properties (Young's modulus and hardness) of top coat may change due to the formation of pores and cracks (Bertrand et al. 2008). The formation of pores and interconnected cracks in the ceramic top coat is found to be increased the strain tolerance of coatings and thereby, reduced the residual thermal stresses (Evans et al. 2001). However, the oxidation resistance of porous ceramic layer is inferior as compared to dense and pore free microstructure. In recent years, much effort have been directed to improve the oxidation resistance of metallic bond coat and formation of alumina enriched TGO at the bond coat and top coat interface through pre-oxidation treatment (Chen et al. 2008). It is still difficult to assess how the TGO thickness and composition affect the TBCs after oxidation at higher temperature. However, electrochemical impedance spectroscopy (EIS) technique being widely used as a non-destructive tool to examine the top coat ceramic and TGO degradations through its resistance and capacitance measurements after oxidation tests at elevated temperature (Jayaraj et al. 2004). The ceramic top coat is also majorly degraded by solid particle impingement leads to higher erosion of turbine blade and other hot section components of air craft engines, especially in the presence of corrosion and sandy environments (Janos et al. 1999).

The hot corrosion resistance of TBCs depends on chemical stability of top coat materials in the presence of several molten salts (Na_2SO_4, V_2O_5 and NaCl) at elevated temperatures. The phase transformation of YSZ top coat from tetragonal (t-ZrO_2) to monoclinic (m-ZrO_2) occurred during hot corrosion test which resulted 3-5% volume change within the coating and it caused catastrophic failure of TBCs (Habibi et al. 2012). Hence, much effort has been directed to seek for new ceramic material with better thermal-physical properties than YSZ (Vassen et al. 2000, Dai et al. 2006, and Chen et al. 2011). Recently, double perovskite slab-rocksalt layer $Ln_2SrAl_2O_7$ (Ln=La, Nd, Sm, Eu, Gd or Dy), more particularly the Samarium strontium aluminates ($Sm_2SrAl_2O_7$ - SSA) has been proposed as new thermal barrier coating material due to its high melting point (~1950 ºC), low thermal conductivity (2.6 W $m^{-1}K^{-1}$), higher thermal expansion coefficient [12-14×10^{-6} K^{-1} (~1000 ºC)] and phase stability (Feng et al. 2012). The reported literature of SSA ceramic was focused on thermo-physical properties, very limited works noticed on coating development, oxidation kinetics, hot corrosion and erosion behavior for TBCs application.

1.1 SCOPE OF THE WORK

The research work on coatings developments, oxidation kinetics, hot corrosion, and high temperature erosion study of SSA TBCs are not examined by researchers. So, it is interesting to address the issues of oxidation, hot corrosion, and erosion behavior at elevated temperatures for new SSA TBCs.

1.2 OBJECTIVES

1. To synthesis and develop the SSA top coat by molten salt method and atmospheric plasma spray process respectively.
2. To study role of thermally grown oxide on the oxidation resistance of SSA based ceramic TBCs.
3. To examine the influence of ceramic top coat and thermally grown oxide microstructures of SSA based TBCs on the electrochemical impedance behavior.
4. To study the hot corrosion resistance of SSA TBCs in vanadates and chlorides environments at elevated temperature.

5. To study high temperature erosion behavior of SSA TBCs at different impingement angles and temperatures.

1.3 ORGANISATION OF THE THESIS

Chapter 1 deals brief introduction of thermal barrier coating with pre-oxidation, oxidation, hot corrosion and high temperature erosion behavior of TBC, scope and objectives of the present work.

Chapter 2 contains detailed literature review of synthesis of ceramic, coating methods, TGO growth during oxidation, hot corrosion and high temperature erosion studies. Also electrochemical impedance behavior of TBCs has been discussed in detail.

Chapter 3 contains description of the experimental tools used and procedures followed for synthesis of SSA ceramic, deposition of the coatings, pre-oxidation and oxidation, hot corrosion and high temperature erosion studies.

Chapter 4 describes the results and discussion of role of TGO growth of air plasma sprayed SSA TBCs during pre-oxidation and oxidation at 1050 and 1100 ˚C, respectively.

Chapter 5 describes the results and discussions of role of top coat and TGO microstructure of oxidized SSA TBCs on the electrochemical impedance behavior.

Chapter 6 describes the results and discussion of the hot corrosion study of SSA and YSZ TBCs in vanadates and chlorides molten salt environments at 700 and 900 ˚C.

Chapter 7 describes the results and discussion of high temperature erosion study of pre-oxidized SSA and YSZ TBCs at different impingement angles and temperatures.

Chapter 8 summarizes the salient conclusions resulting from the present investigations and followed by scope for future work.

CHAPTER 2

2 LITERATURE REVIEW

This chapter describes the importance of thermal barrier coating (TBC), various constituents of thermal barrier coatings, synthesis of ceramic oxides, oxidation, hot corrosion and erosion behaviors of TBC at elevated temperatures.

2.1 Introduction

The main function of thermal barrier coating (TBC) is to provide thermal insulation against hot gases in engines and turbines and reduce the surface temperature of the underlying alloy components (Uzun et al. 1999). It is widely used in hot sections of gas turbines as a thermal insulation to promote their operating temperature and enhance the engine efficiency (Padture et al. 2002). TBCs are now commonly used on combustors, flame holders, high pressure gas turbine blades, nozzles and hot section components. The thickness of TBCs varies from 100 μm to 1 mm with the presence of defects such as pores and cracks in the microstructures. These coatings impart the desirable properties of low thermal conductivity and high strain tolerance at elevated temperature (Wortman et al. 1989). The properties such as higher melting point, low thermal conductivity, matching thermal expansion coefficient and chemical stability are required for good TBC material. Fig. 2.1 shows a TBC system applied on the turbine blade and temperature drop across the TBC thickness. The turbine blade also contains internal hollow channels for coolant gas flow to remove the heat being conducted through the ceramic coatings (Karaoglanli et al. 2013).

2.2 Components of TBCs

A typical TBC system consists of (i) a super alloy substrate, (ii) a bond coat (BC), usually MCrAlY (M=Ni, Co or Ni+Co), (iii) thermally grown oxide (TGO) and (iv) the ceramic outer layer, usually 6-8 wt. % Yttria stabilized zirconia deposited

either by air plasma spray (APS) or electron beam-physical vapor deposition (EB-PVD) processes (Sohn et al. 2001). In the following sections the above mentioned TBCs components are discussed as:

2.2.1 Substrate materials

Substrate materials must have satisfied at least two important characteristics namely a high strength and resistance to aggressive environment at elevated temperature. The range of strengths of various metallic and nonmetallic materials as a function of temperature is shown in Fig. 2.2.

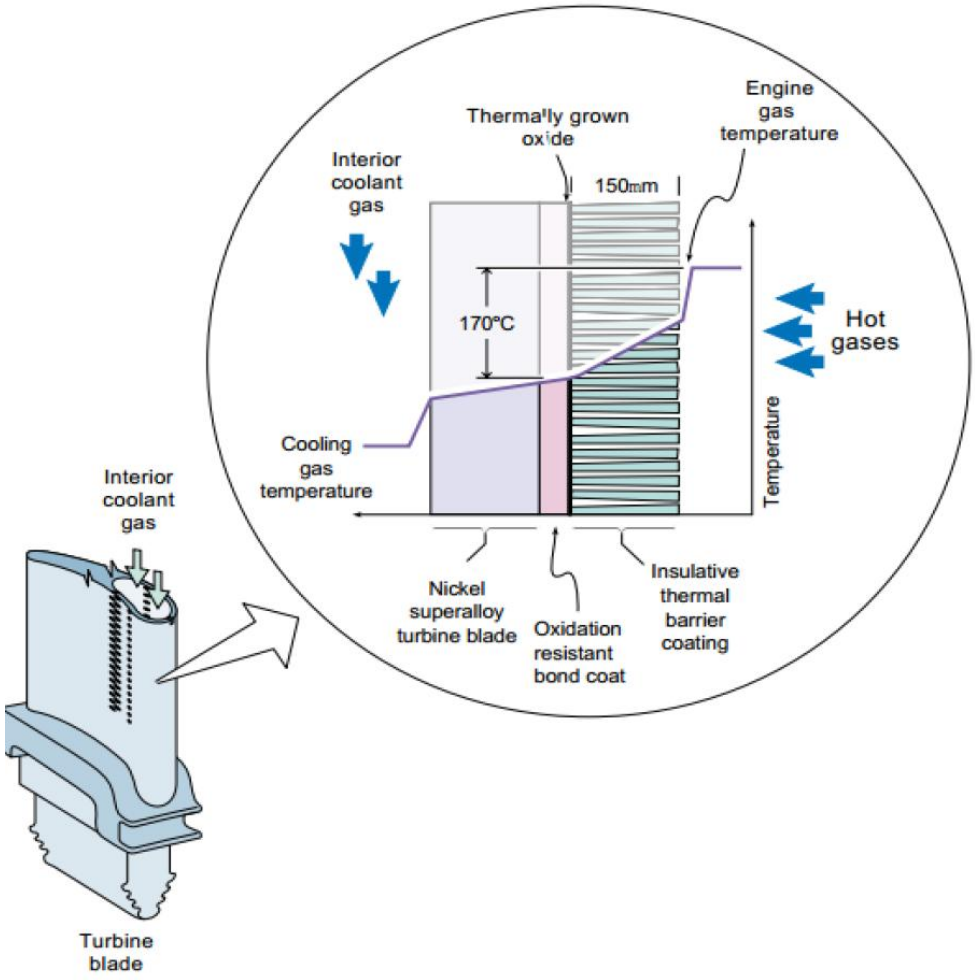

.

Fig. 2.1: Schematic diagram of TBC applied to the gas turbine blade (Karaoglanli et al. 2013).

Nickel and cobalt based super alloys are the most advanced metallic alloy which is used at high pressure and temperature environment. The important point to use substrate materials they must have to be extraordinary mechanical properties (strength, toughness, creep and fatigue), suitable alloy design (high Ni, Cr, Mo, Ti, Al, V, W, Co and rare-earth elements) and support high coating tendency & integrity (surface roughness, adhesiveness, etc.) at high temperature.

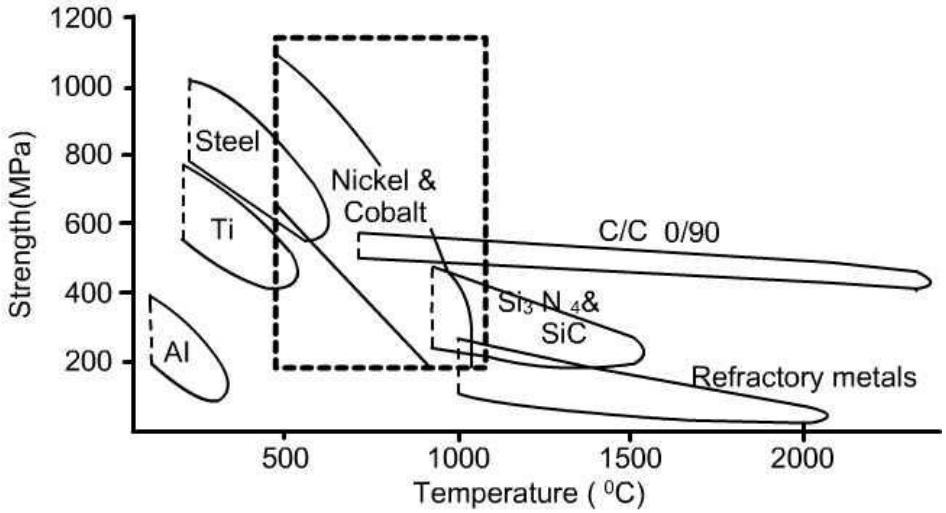

Fig. 2.2: Temperature capabilities of several classes of alloys (Meetham, 1988).

2.2.2 Metallic bond coat

The most important function of bond coating is to provide a gradual transition of coefficient of thermal expansion (CTE) mismatch between the metallic substrate and ceramic top coat. Bond coat materials not only enhance resistance to inter-diffusion with the substrate, and high creep strength with suitable ductility but also it provides oxidation protection of the substrate with the improved adhesion of the ceramic topcoat (David et al. 2000). Bond coat materials mainly consists of variety of diffusion-aluminide or MCrAlY alloys (M = Ni and/or Co). Nickel is used to enhance oxidation resistance however; cobalt provides high resistance to corrosion. The presence of aluminium acts as a local reservoir to provide slow growing thermally grown oxides (TGO), α-alumina during service conditions to provide oxidation protection. Presence of chromium in MCrAlY alloy enhances oxidation and

corrosion resistance. Yttrium control protection from sulfur diffusion into the coating by acting as a gettering site and also promoting formation of alumina based TGO at the interface.

Fig. 2.3 shows the role of high chromium contents in various types of bond coat materials (alumindes and NiCoCrAlY) and its oxidation resistance, this figure clearly shows a small Cr content in NiCrAlY alloy reduced the oxidation and hot corrosion behavior as compared to others bond coats materials.

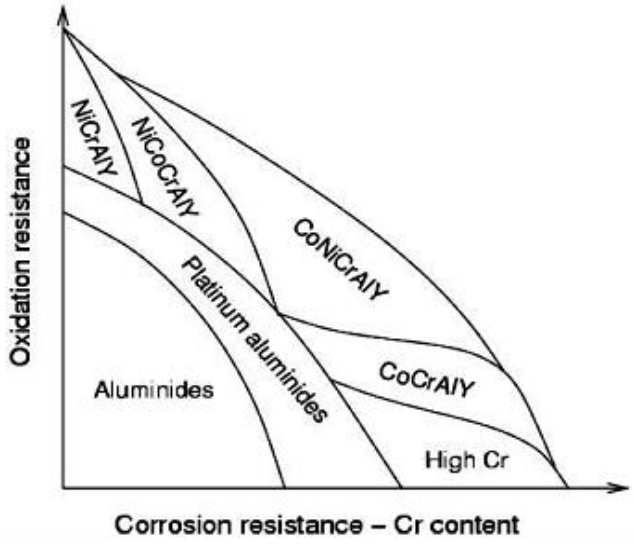

Fig. 2.3: Optimum coating composition in relation to oxidation and hot-corrosion resistance (Schütze, 2000).

2.2.3 Thermally grown oxide (TGO)

TGO layer formation take place near the topcoat-bond coat interface due to the oxidation of bond coat in service conditions results in the formation of a TGO. The foremost oxide formed due to the oxidation of bondcoat (typically MCrAlY) is alumina. However, other types of oxides such as spinel ($Ni(Cr,Al)_2O_4$ and nickel oxide (NiO) are also formed along with pure alumina. Presence of vacancies and the interconnected porosity network present within the topcoat allows free flow of oxygen (air) and induces the formation of TGO.

The formation of TGO layer mostly occurred either by outward diffusion of metal ions or inward transport of oxygen ions through oxide layer (Rangaraj et al. 2003). This oxide allows minimum transport of oxygen ions to underlying substrate and reduces the oxidation of substrate materials. As these oxides posses a high thermodynamic stability, allow to grow slowly and formed easily on the surface of bond coat. Toscano et al. (2006) have studied the two different types of bond coat materials such as Ni and Co alloy, the SEM images of both the conditions are shown in Fig. 2.4 after oxidation test at 1100 ˚C for 111 h. Both the figures clearly show TBC layer at the top, bond coat layer at the bottom and formed TGO layer at the interface. TGO thickness was noted approximately 3.1 and 3.8 µm for NiCoCrAlY and CoNiCrAlY bond coat respectively.

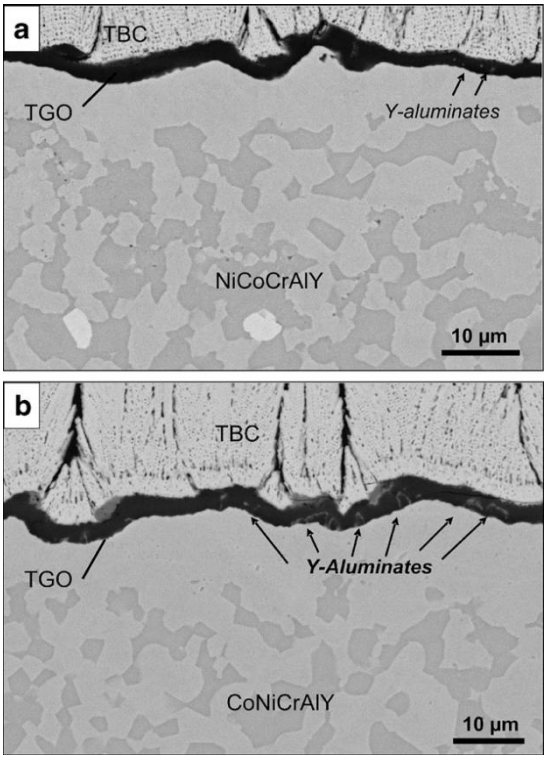

Fig. 2.4: Cross sectional SEM image of a) NiCoCrAlY, b) CoNiCrAlY bond coats after exposure to 1100 ºC for 111 h of oxidation in air. Note: TGO containing pure alumina on NiCoCrAlY than on CoNiCrAlY bond coat, i.e., it shows minor amounts of Y/Al oxide precipitates in TGO (Toscano et al. 2006).

2.2.4 Ceramic top coat material

The ceramic topcoat materials predominantly provide thermal insulation to the metal substrate underneath and control total integrity of TBC system due to good thermal stability, a low thermal conductivity, high coefficient of thermal expansion (CTE) in combination with a high fracture toughness. Presently, 6-8 wt.% yttria stabilized zirconia (YSZ) top coat ceramic material is one of the promising thermal barrier coating materials because of its low thermal conductivity, relatively high CTE and adequate toughness. However, YSZ also shows limitation and found to be unstable in high temperature corrosive atmosphere and forms YVO_4 and monoclinic-ZrO_2 (destabilization). Destabilization causes the volume change and lead to spallation of the coating significantly (Vaβen et al. 2000, 2010).

Search for alternative TBC materials is a great importance in order to improve both the performance and durability of the TBC component. Even lower thermal conductivity, higher operating temperature, better sintering behavior and phase stability at higher temperature are required for alternate thermal barrier oxides. There are various new type of ceramic materials are developed to contend against existing conventional YSZ due to specific characteristics such as high melting points, low thermal conductivity, high thermal expansion coefficients and high temperature phase stability which is shown in Fig. 2.5 (Feng et al. 2012, Wan et al. 2010).

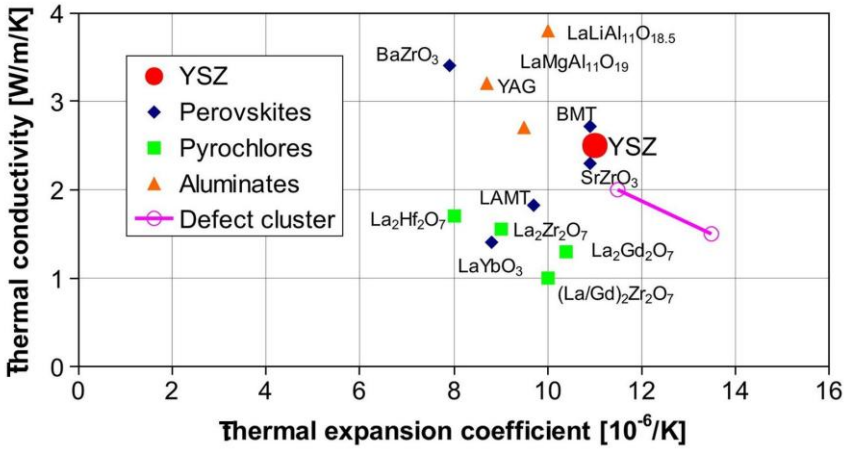

Fig. 2.5: Plot of thermal conductivity and thermal expansion coefficient of new ceramic thermal barrier coating materials (Vaβen et al. 2010).

TBC candidate materials which have been reported include garnets ($Y_3Al_5O_{12}$; YAG) (Su et al. 2004), hexaluminates (Chen et al. 2011), YSZ-Ta_2O_5/Nb_2O_5 composite (Raghavan et al. 2004) and Gd_2O_3 stabilized zirconia (Raghaman et al. 2006). A patent by David et al. (2000) proposed zirconia stabilized yttria, ceria, calcia, magnesia, india and erbia as TBCs materials.

Most recently, perovskite (ABO_3) and pyrochlores ($A_2B_2O_7$) type ceramic oxides have attracted a lot of attention (Yamanaka et al. 2005, Ma et al. 2008, Liu et al. 2010, Feng et al. 2012, Qu et al. 2012) owing to their interesting properties. Generally, pyrochlores possess low thermal conductivity, low sintering and excellent thermal stability. Among the investigated pyrochlores, $La_2Zr_2O_7$ and $Gd_2Zr_2O_7$ have low thermal conductivity of 1.56 W $m^{-1}K^{-1}$ at 1000 ºC and thermal stability up to 2000 ºC. The drawback is the relatively low thermal expansion coefficient of ~ 10 x 10^{-6} K^{-1} which gives rise to higher thermal expansion mismatch than YSZ. It has been reported that double layer system with inner YSZ and top $La_2Zr_2O_7$ layer improves the life time and extends the high temperature capability in thermal gradient cyclic test. Though, loss of La_2O_3 during thermal spraying of $La_2Zr_2O_7$ may have harmful effect on the coating performance. Apart from pyrochlores, perovskite have also been proposed as promising candidates for TBC applications. It has been found that $BaZrO_3$ has relatively shorter lift time than YSZ due to the poor thermal and chemical stability, while $SrZrO_3$ exhibits better performance during thermal cycling (Ma et al, 2008). Unfortunately, it undergoes transformation at intermediate temperature accompanied by a change in volume. The lists of components coated by conventional YSZ ceramic and relevant industries are listed in Table 2.1:

Table 2.1: lists of components coated by conventional YSZ ceramic and relevant industries

Sl.No	List of components	Industries
1	Turbine guide vane in turbofan engine	Rolls-Royce, General Electric, Pratt and Whitney and Siemens
2	IC engine pistons, valves and Exhaust pipes in automotive applications	Nissan motors and Praxair Surface Technologies

2.3 Synthesis of ceramic oxides

In general conventional powder metallurgical method is being used to fabricate the large scale production of ceramic powder from its solid phase at higher temperature (>1300 ˚C). But in the literatures several methods are reported for the preparation of ceramic oxides as seen in Table 2.2.

Table 2.2: Various methods of synthesis of ceramic and their merits and demerits (Sikalidis, 2011)

Sl. No	Method of powder preparation	Merits	Demerits
1	Mechano-chemical route	Fine particle size, good for non-oxides	Limited purity and homogeneity
2	Solid state route	Simple apparatus (required compacting)	It requires higher operating temperature, limited homogeneity for multi-component system
3	Precipitation, sol-gel, spray pyrolysis and sol-gel process	High purity and small particle size	Expensive and powder agglomeration a common problem
4	Molten salt route	High purity, in expensive and suitable for bulk production	Powder agglomeration

As compared to other synthesis methods molten salt route can be economically viable and it's more suitable for bulk production of the ceramic at laboratory level. In molten salt synthesis, the salts with higher melting point is added to the reactants of ceramic and heated above the melting point of salts. Hence this molten salt act as a solvent and this enhances the reaction rate of reactants. One of the examples of used salt in molten synthesis is chlorides and sulfates. The product morphology, size and shape are mainly controlled by selecting temperature and duration of synthesis process (Kimura, 2011).

Lin et al. (2015) have synthesized $LiNbO_3$ ceramic powder by molten salt method at 650 ˚C for 5 min to 3 h. The weight ratio of oxides to salt was fixed to about 2:1. Results showed that particle growth is mainly controlled by diffusion process and size was controlled by amount of salt with increase in temperature.

Fig. 2.6 shows the XRD patterns of as synthesized $LaNbO_3$ powder at different temperatures from 650 to 800 ˚C. The spectrum revealed that the diffraction peaks intensity gradually increased with increasing temperature, increased the particle size.

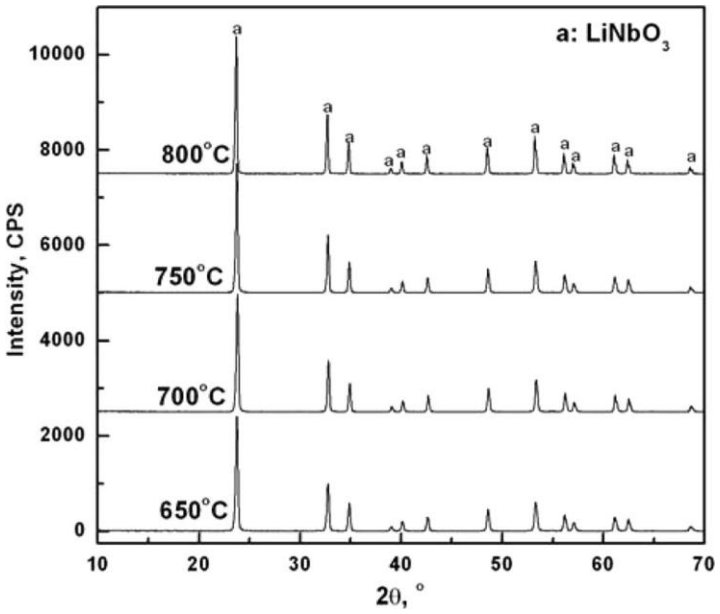

Fig. 2.6: XRD patterns of $LaNbO_3$ synthesized at different temperatures in Li_2SO_4–Na_2SO_4 molten salt (Lin et al. 2015).

Molten salt synthesis of tin lanthanum zirconate titanate stannate (PLZTS) ceramic powder was synthesized by Zhao et al. (2006). $LiSO_4$-Na_2SO_4 and NaCl-KCl molten salts were used for the synthesis process. They found that among these two salts chloride flux is preferential to the formation of single phase tetragonal PLZTS at 900 ˚C due to higher mobility of species. The average particle size was obtained by this synthesis to have a uniform distribution with no agglomerates (Zhao, et al. 2006).

2.4 Deposition of ceramic oxides and metallic bond coat by thermal spray process

Thermal spray process is a surface modification technology in which ceramics and metals are heated to molten and semi-molten state, then melted particles accumulated onto the surface of substrate thereby forming a coating. Most of the particles become a spray and scattered from the substrate during the coatings process

at high temperature. Thermal spraying process and its important characteristics such as formation of oxide films, molten particles impacting capability of particles, mechanical fitting, formation of oxide film, un-melted particles and pores formation are shown in Fig 2.7.

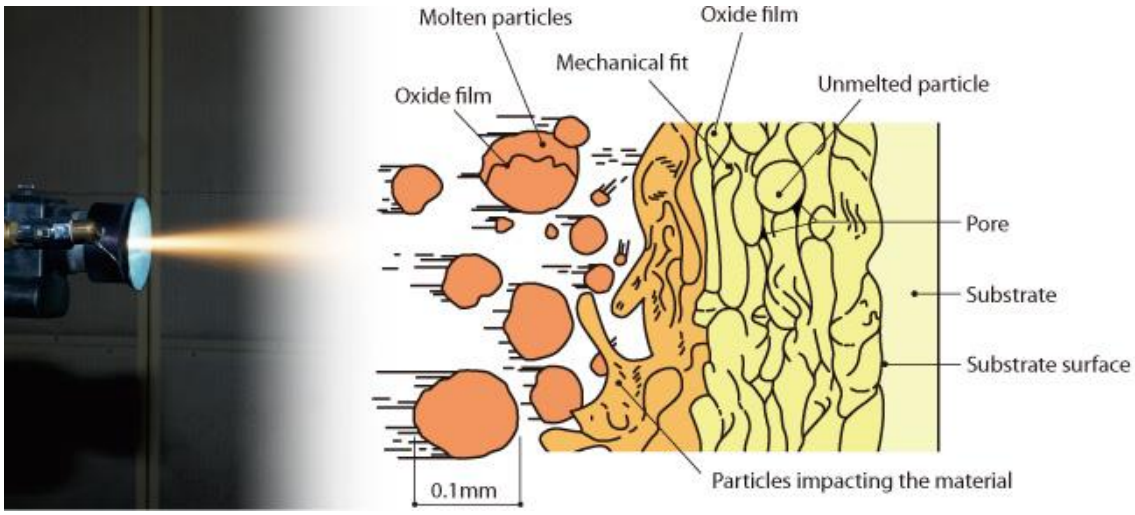

Fig. 2.7: Schematic representation of thermal spraying process (http://www.ofic.co.jp/en/r_and_d/thermalspraying/).

The all above characteristics are also depends on feeding rate, distance of gun from substrate and gun velocity. The different types of thermal spray process are explained in the following section as:

2.4.1 Types of thermal spray processes

The thermal spray processes can be classified into four major types,

1. Flame spray process
   - (i) High velocity oxy fuel process (HVOF)
   - (ii) Wire flame process
   - (iii) Detonation gun process
2. Electric arc or wire arc process
3. Kinetic energy process

(i) Cold spray process

4. Plasma arc process

(i) Air or atmospheric plasma process (APS)

(ii) Vacuum plasma spray process (VPS)

The salient features of the above processes are mentioned in Table 2.3.

Table 2.3: Comparison of thermal spray processes (http://www.oerlikon.com/metco)

Technique/Parameter	Temperature	Velocity of material	Type of material	Type of coating
HVOF	2500-3100 ˚C	400-800 m/s	Wire or powder	Dense coating
Wire flame	~3100 ˚C	Upto 200 m/s	Wire (metal)	Porous coating
Detonation gun	2500-3100 ˚C	Supersonic velocity (800-1200 m/s)	Wire or powder	Dense coating
Electric arc process	~4000 ˚C	~150 m/s	Wire	Porous coating
Cold spray	~800 ˚C	300-1200 m/s	Powder	Dense coating
Vacuum plasma process	5000-16,000 ˚C	200-400 m/s	Powder	Porous coating

Among all thermal spray processes the HVOF, cold spray and plasma spray processes are widely used for bond coat and top coat materials respectively. In order to make a dense bond coat with negligible porosity, HVOF and cold spray processes are more suitable than plasma spray process due to its high impact particle velocity. The deposition of top ceramic coat can be done only by plasma spray process due its higher flame temperature and moderate velocity to get porous top coat.

2.4.1.1 Air plasma spray process

Air plasma spray deposition technique is commonly utilized to deposit TBCs onto components such as combustors, turbine outer air seal ring segments, and gas turbine blades (Kisi et al. 1998). Air plasma spray process is extensively used

technique for TBC deposition due to low operational cost as compared to EB-PVD (Miller, 1997).

In this process, plasma jet melts the raw materials in the form of powder which is filled in powder chamber of spray setup (Fig. 2.8). The plasma is created in a plasma gun. This process is conducted in air and known as an air plasma spray (APS) process (Jones, 1997). The qualities of coating depend on particle size and morphology of used bond coat and top coat powders. The required particle size of the powder should be in the range of 30-50 μm to get better control. However, when the particles are very fine (< 10 μm), which is difficult to penetrate the plasma, to flow in plasma velocity and to reach at the surface of substrate. The morphology of the powders is also important factor which determines the ability to flow and melt. It was found that the best ability to flow using a spherical shape powders (Xie et al. 2007).

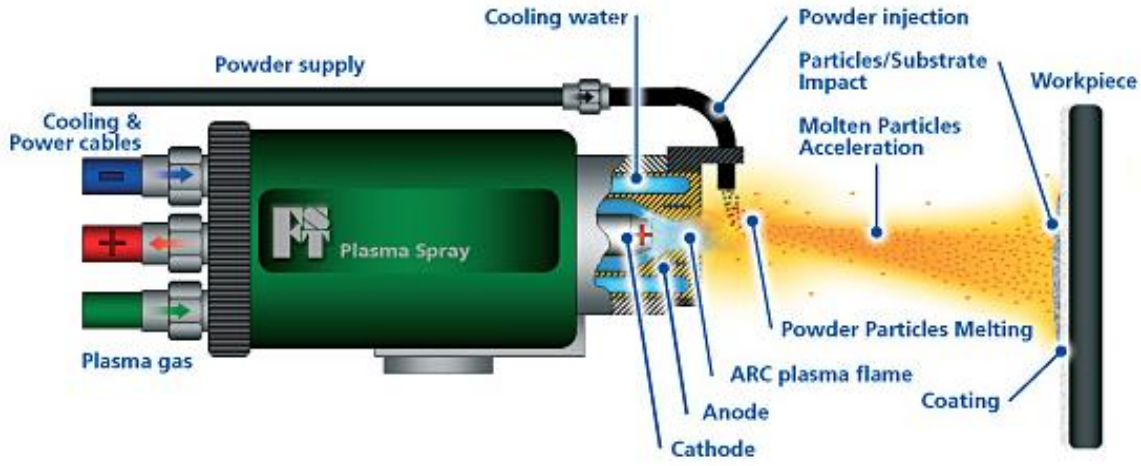

Fig. 2.8: Schematic illustrations of plasma spray process (http://www.fst.nl/plasma-spray/).

The ceramic top coat deposited by APS process, mostly contains 10 to 15 vol. % porosity. These porosities can be controlled by finer powder particle size and closer spray distance. The microstructure of ceramic top layer consists of splats (melted particle) and defects such as pores and cracks. The formation of pores and interconnected cracks in the ceramic top coat is found to increase the strain tolerance of coatings and thereby, reduced the residual thermal stresses (Evans et al. 2001). The major air plasma spray parameters are summarized in Table 2.4.

Table 2.4: The major air plasma spray parameters.

Plasma gas	These gases are used to generate the plasma jet: 1.Primary gas: Ar or N_2 2. Secondary gases: He or H_2
Torch power	The voltage or current must be modulated to achieve the appropriate power the plasma gases must also be modulated for uniform coating.
Torch velocity	Velocity of the torch may be controlled through the controller. Slower velocities will produce thicker coatings per pass. The torch velocity must be in the range of 200 to 400 m/s.
Stand-off distance	Stand-off distance is the distance between the torch and substrate. An appropriate standoff distance will ensure that the powder particles are fully molten before deposition at the substrate
Powder feed rate	Selection of appropriate powder feed rate will avoid clogging of the powder tubes and most particles fully melted by the plasma jet. The powder feed rate is usually modulated by the carrier gas (N_2) flow rate.

2.5 High temperature oxidation behavior of air plasma sprayed TBCs

The TGO thickness increases with the thermal exposure time and followed a parabolic law (Evans et al. 2001). Thickness of TGO determines the stresses within ceramic top coat, TGO, and the interface of TGO/bond coat. Ogawa et al. (2006) have reported a four kinds of oxides formation such as α-Al_2O_3, Cr_2O_3, NiO and (Ni,Co) (Cr, Al)$_2O_4$ (CSN) in TGO. They are associated with the failure of TBCs in different mechanisms. It was also suggested a uniform and dense α-Al_2O_3 is an important for good oxidation protection to underlying substrate. However, discontinues α-Al_2O_3 scale results in the formation of other oxides which exhibits a weak oxidation resistance. Further, α-Al_2O_3 exhibits a better adhesion to ceramic top coat over aforementioned these oxides. Cr_2O_3, being a protective scale against oxidation and hot corrosion. Above all, these spinels (CSN) are porous, brittle and lacking of potential on anti-oxidation (Chen et al. 2008). Fig. 2.9 shows the formation of spinel after exposure to 100 and 430 cycles at 1050 ˚C.

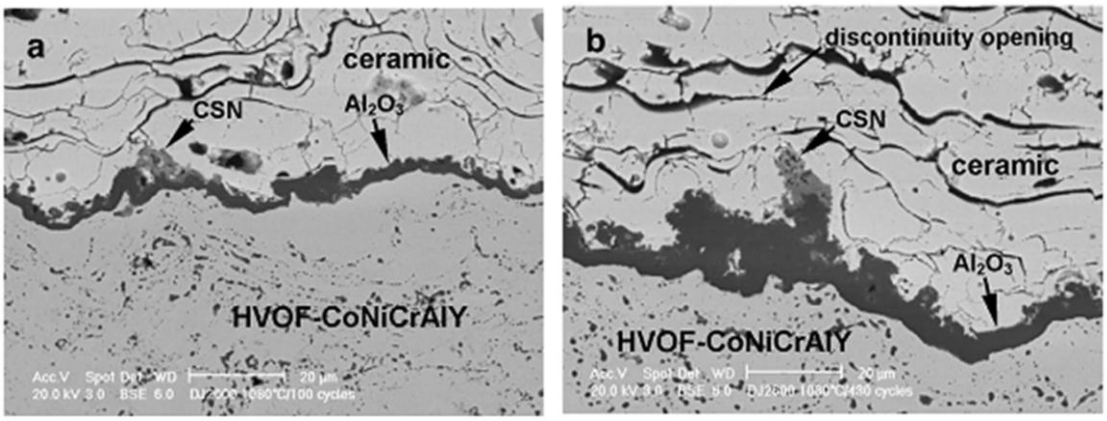

Fig. 2.9: (a) The TGO formed in the TBC with an HVOF-CoNiCrAlY bond coat after 100 cycles, which contained a nearly continuous Al_2O_3 layer with small amount of chromia, spinel and NiO clusters (CSN); and (b) Similar condition of operation after 430 cycles at 1050 ˚C (Chen et al. 2008).

Role of surface coverage area of the mixed oxides on the bond coat surface and thermal cyclic lifetime after TBCs failure is shown in Fig. 2.10. It clearly indicates that increase of surface coverage of spinel and Cr_2O_3 on the TGO interface during the thermal cyclic test, a significant reduction of the coating lifetime. So, integrity of TBC can be controlled by mixed oxide formation (Li et al. 2010).

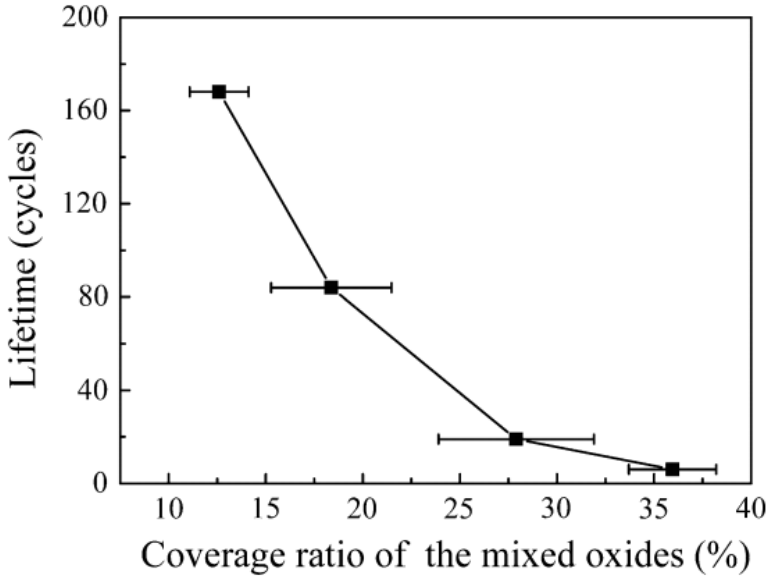

Fig. 2.10: Relationship between the surface coverage area of the mixed oxides on the bond coat surface and thermal cyclic lifetime after TBCs failure (Li et al. 2010).

Nath et al. (2014) have extensively studied the isothermal oxidation behavior of compositionally graded (layers containing a mixture of CoNiCrAlY and YSZ) coatings along with conventional duplex (CoNiCrAlY/YSZ coating) TBCs. They have developed a correlation between TGO growth kinetics with respect to temperature (shown in Fig. 2.11). Fig. 2.11 shows the thickness of TGO of (1) duplex and (2) compositionally graded TBCs at three different temperatures of 900 [Fig. 2.11 (a)], 950 [Fig. 2.11 (b)] and 1000 ˚C [Fig. 2.11 (c)].

It is clearly exhibited that kinetics growth of the TGO for given temperature have parabolic in nature. But, growth rate was much lower in compositionally graded coatings as compared to duplex TBCs due to the presence of protective Al_2O_3 layer throughout the coating in an intermittent manner and control the supply of oxygen at the bond coat and top coat interface.

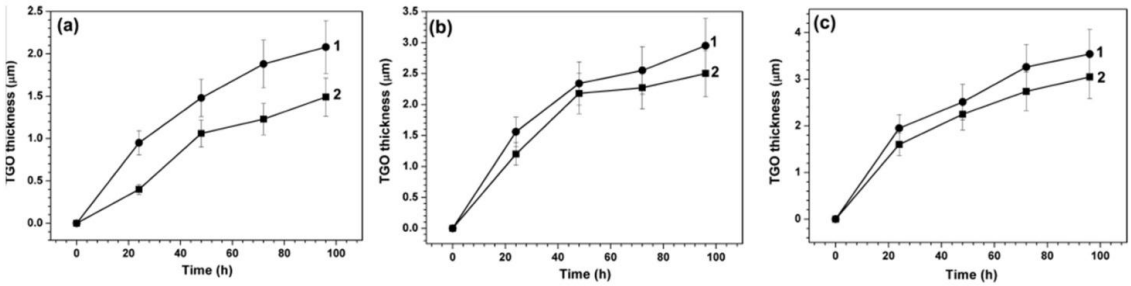

Fig. 2.11: Plot of thickness of TGO with respect to oxidation time (1) duplex; and (2) compositionally graded TBCs after exposure to (a) 900; (b) 950; and (c) 1000 ˚C (Nath et al. 2014).

Darolia (2003) and Weimer et al. (2003) have reported the role of pre-oxidation of bond coat at low oxygen partial pressure before the deposition of the ceramic top coat to minimize the oxidation by protective α-Al_2O_3 scales. Similarly, Matsumoto et al. (2006) have studied the oxidation and thermal cyclic behavior of 8% YSZ TBCs at different oxygen partial pressure to distinguish the TGO growth. They have found that oxidation resistance depends on TGO thickness and its total composition. The microstructure of the samples oxidized at different oxygen partial pressures at 1200 ˚C for 50 h is shown in Fig. 2.12 (A-E).

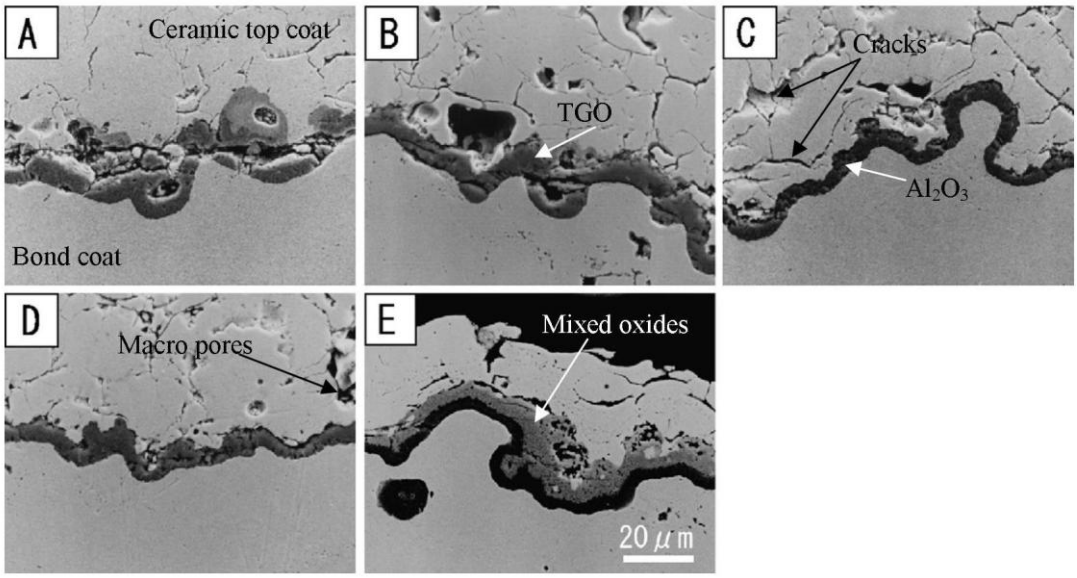

Fig. 2.12: Cross sectional SEM microstructures of pre-oxidized 8%YSZ treated at the pressure of (A) 0.2; (B) 10^{-12} to 10^{-13}; (C) 10^{-14} to 10^{-15}; (D) 10^{-16} to 10^{-17} atm; and (E) without pre-oxidation (Matsumoto et al. 2006).

EDS analysis at the TGO region showed that the dark region at the interface in Fig. 2.12 (C) mainly composed of Al and O with low concentrations of other elements such as Ni and Cr. But other samples (A, B, D and E) showed grey outer layer consists of Ni, Cr, Co, Al and O. They found that the average thermal cyclic life of TBCs for sample C is twice as compared to other specimens A, B and D. Nijdam et al. (2006) have studied the combined effect of pre-annealing and pre-oxidation treatment on the processed of TBCs on NiCoCrAlY bond coatings. They have noted that the thickened TGOs have longest life spans, during thermal cycles test due to formation of large α-Al_2O_3. However, it is still not clear mechanism reports are available that how the TGO thickness and composition affects the oxidation kinetics of plasma sprayed TBCs. The TGO growth and oxidation behavior of various ceramic TBCs is shown in Table 2.5.

Table 2.5: TGO growth and oxidation performance of various ceramic TBCs in different environmental conditions.

Sl. No	Material	Condition/ Environment	Summary	Reference
1	NiCrAlY-Al_2O_3 bond coat (the absence of Top coat)	Isothermal oxidation tests at 1000 °C for 100 h in static air/Changing the composition of NiCrAlY coatings by incorporating Al_2O_3 as second phase	The Al_2O_3 second phase was distributed in the grains as well as on the grain boundaries of the coatings. The Al_2O_3 second phase could improve the oxidation resistance of NiCrAlY coatings during oxidation at 1000 °C and slow down the growth of Cr_2O_3 and $NiCr_2O_4$.	Wu et al. (2003)
2	NiCrAlY bond coat (the absence of Top coat)	Oxidation tests at 1000 °C for up to 1000 h/ Varying O_2 in NiCrAlY	Coatings with the highest oxygen content, porous Cr_2O_3/$NiCr_2O_4$ oxide scale formed. Low oxygen content in the coating is beneficial to the formation of a protective α-Al_2O_3 scale.	Tang et al. (2004)
3	YSZ-NiCrCoAlY with 0.25% Hf	Oxidation test was conducted in static air / Test was carried out at 900, 1000, 1100 and 1200 °C for standard and vertically cracked (VC), APS coatings. At each temperature, the specimens were exposed for 25, 50, 75	The difference between oxidation behavior of the vertically cracked and standard structures are attributed to the effects of microstructure morphology and porosity on oxygen ingression into the zirconia and TGO layers. The isothermal oxidation resistance of the STD and VC microstructures is similar at temperatures up to 1200 °C.	Soboyejo et al. (2011)

		and 100 h.		
4	YSZ/NiCrAlY YSZ/Al_2O_3/ NiCrAlY, YSZ+Al_2O_3/NiCrAlY and Al_2O_3/YSZ/ NiCrAlY	Oxidation test was carried out at 1100 ˚C for 4 h cycling / Composite YSZ with Al_2O_3 coating	The presence of alumina as a top coat or as mixed oxide with YSZ can improve the durability of YSZ coating towards oxidation at 1100 ˚ C presumably by oxygen diffusion slowdown. The thickness of the TGO which is an indication of diffused oxygen through the TBC layer was reduced when Al_2O_3 was used as a top layer on YSZ.	Keyvani et al. (2011)
5	8% YSZ-NiCrAlY	Atmospheric oxidation test was carried out at 1050 C / cyclic test was conducted for 50-min heating followed by a 10-min cooling	The outer layer was a mixed layer consisting of NiO, Cr_2O_3 and $Ni(Al,Cr)_2O_4$spinels, whereas inner layer was composed of Al_2O_3. Failure of the coating occurred near the interface between the mixed oxide layer of the TGO and the top coat.	Ni et al. (2011)
6	8 wt.% YSZ-NiCrAlY	Ar atmosphere with <10 ppm of oxygen / TBCs with different TGO thicknesses ranging from 1.3 μm to 7.7 μm were prepared by controlling isothermal oxidation time	A critical TGO thickness of about 6 μm, over which the thermal cyclic lifetime decreases more significantly with the increase in TGO thickness.	Dong et al. (2014)

TGO growth and oxidation behavior of plasma sprayed TBCs is also controlled by microstructure and phase structure of top coat materials at elevated temperatures (Golosnoy et al. 2009 and Karger et al. 2011). Particularly, the phase transformation of YSZ from tetragonal (t-ZrO_2) to monoclinic phase (m-ZrO_2) during thermal cycles which results 3-5% volume change within the coating and increased sintering rate of the porous TBC layer above 1200 ºC, which tend to cause catastrophic failure of TBCs (Ochrombel et al. 2010). It is still difficult to assess how TGO thickness and composition affects the TBCs after oxidation at higher temperature.

Kim et al. (2009) have investigated the degradation of plasma sprayed YSZ TBCs by nano-indentation technique. The YSZ TBC was isothermally aged at 1100 ˚C for various times up to 400 h. The mechanical properties of top coat, TGO, and bond coat were measured using same depth of indentation during the test. The obtained results of load-depth plot, elastic modulus and hardness plots are shown in Fig. 2.13 (a), (b) and (c) respectively. From Fig. 2.13 (a) it is understood that the load required for TGO and top ceramic coat is around two to three times than bond coat for the same depth of penetration.

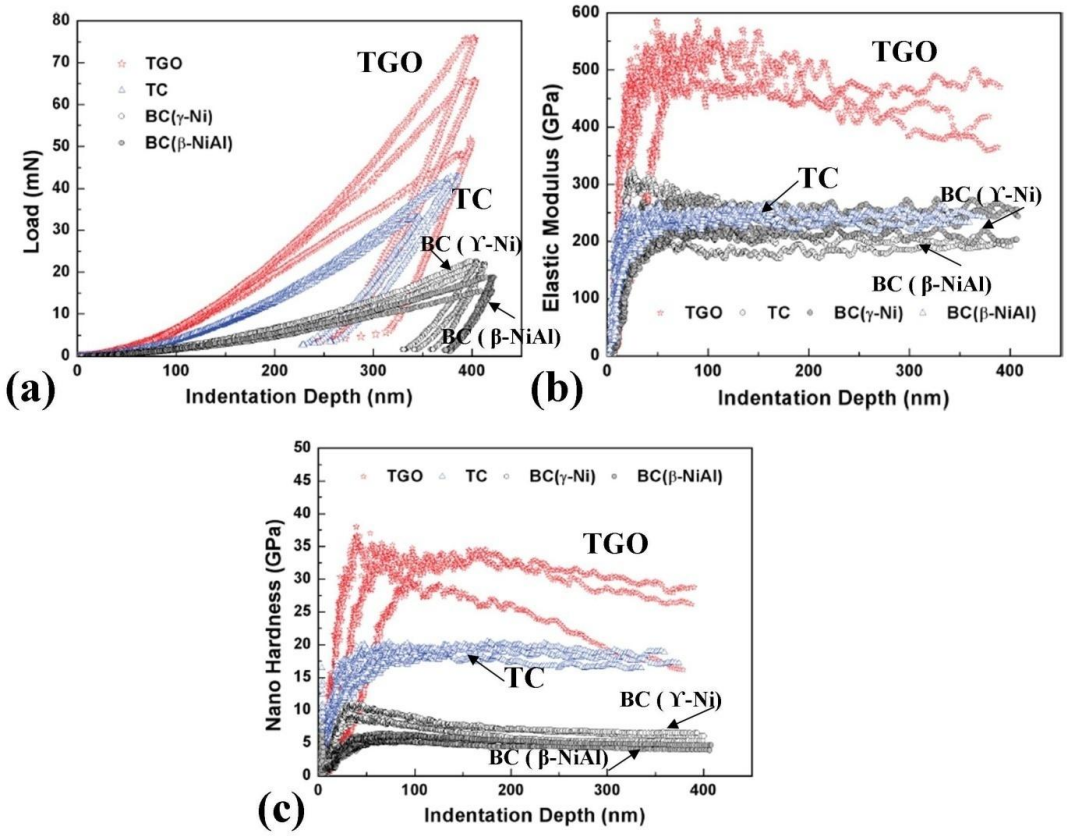

Fig. 2.13: (a) load versus depth curve; (b) elastic modulus with indentation depth; and (c) nano-hardness of the coating layer after oxidation at 1100 ˚C for 100 h. Note: TC-top coat and BC-bond coat (Kim et al. 2009).

The elastic modulus and hardness of TGO is considerably higher than two phases (γ'-Ni and β-NiAl) of bond coat and ceramic top coat [(Fig. 2.13 (b and c)] due to compact and highly enriched α-Al_2O_3 at the interface. The large elastic modulus variation of TGO with adjacent materials such as ceramic top coat and bond coat leads to severe residual thermal stresses which is the main cause for delamination of TBCs at the interface.

The residual stresses of thermally cycled conventional YSZ TBCs and Al_2O_3 film pre-deposited YSZ TBCs were measured by Li et al. (2012) after exposure to 1100 ˚C for 30 min. After thermal cycles the peaks between 550 and 700 cm^{-1} decomposed into 620 and 640 cm^{-1} [Fig. 2.14 (b)]. But the peaks at 260 cm^{-1} showed the negative shift towards right side confirmed the formation of compressive stresses in the coatings.

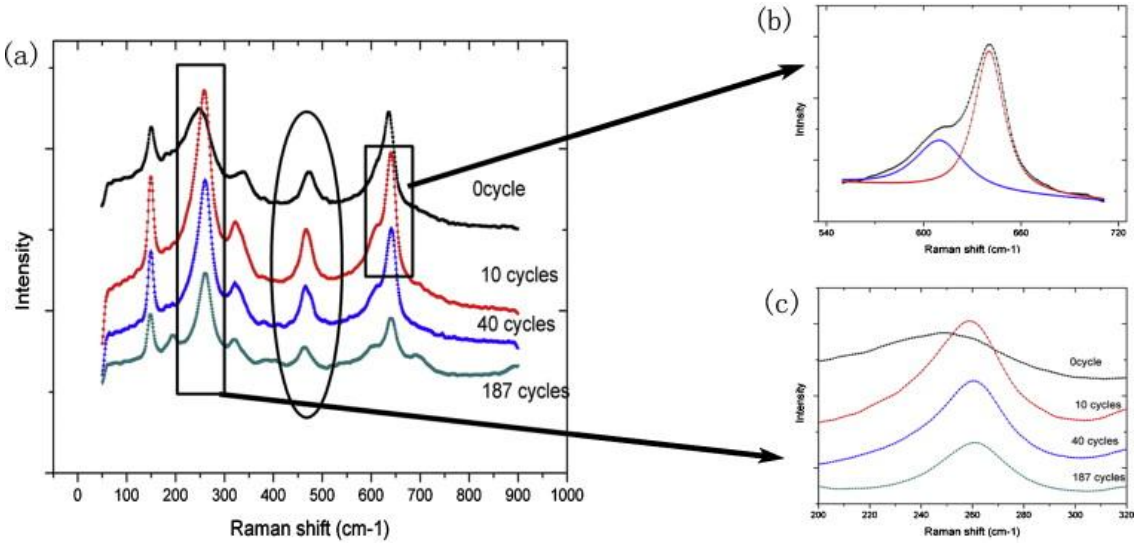

Fig. 2.14: Raman spectra of conventional YSZ TBCs after exposure to different thermal cycles at 1100 ˚C (Li et al. 2012).

The spectral shift of band at 470 cm^{-1} is given in Table 2.6. The formation of tensile stresses could be seen in the case of conventional YSZ TBCs. The increase in compressive stresses was found to be about -5.67 and -4.95 cm^{-1} for conventional and modified TBCs respectively, after exposure to 137 thermal cycles at 1100 ˚C (Fig. 2.15).

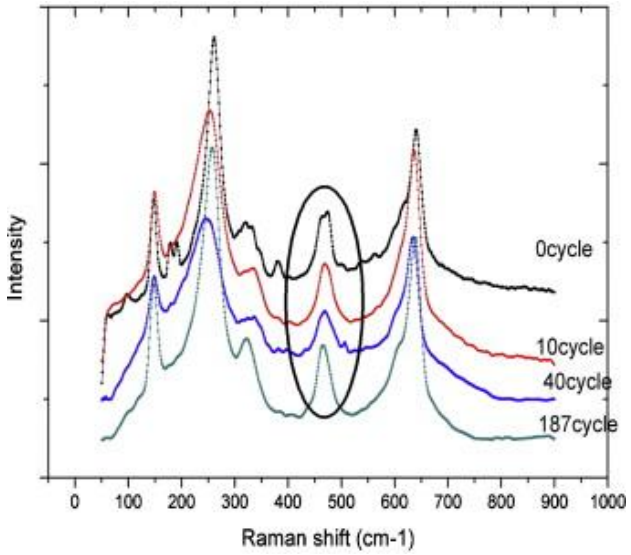

Fig. 2.15: Raman spectra of modified YSZ TBCs after exposure to different thermal cycles at 1100 ˚C (Li et al. 2012).

The reduction in residual compressive stresses approximately 10% was mainly due to the formation of uniform and compact TGO at the bond coat and top coat interface mitigate the residual stresses in the modified TBC system.

Table 2.6: Spectral shift (ΔΩ) at the band 470 cm^{-1} in the YSZ top coat.

Cycles	Conventional TBC	Modified TBC
0	2.83	2.04
10	-2.43	-0.20
40	-2.57	-2.22
137	-5.67	-4.95

2.6 Electrochemical impedance behavior of TBCs

Several techniques have been proposed to examine the total TBC system reliability namely, infrared thermography, acoustic emission and photoluminescence piezospectroscopy (Berndt et al. 1985 and Harada et al. 1995). In addition to these techniques, the electrochemical impedance spectroscopy (EIS) has also been found to be very useful in evaluating the structural changes of TBCs such as thickness reduction, the formation of porosities, TGO growth, defects initiation, and coating delamination as the conductive electrolyte can easily penetrate into former defects [Sohn et al. (2001), Byeon et al. (2005), Huang et al. (2011) and Chen et al. (2016)]. These degradations can be measured non-destructively using an impedance kinetic (resistance and capacitance) change of both the ceramic top coat and TGO layer.

Microstructural evolution of YSZ TBCs after thermal cycling was studied by Song et al. (2011) using EIS. They found the resistivity of alumina-based TGO scale increases with increasing oxidation time, due to increasing TGO growth at the interface. Fig. 2.16 showed the phase angle and frequency (Bode Plot) of YSZ samples exposed thermal cyclic test 1030 ˚C for different cycles. The frequency in the range of 300 Hz indicates response for TGO and this increase from right hand side for the specimens subjected to 100 to 250 cycles. Further, increasing thermal cycles to 400, it did not show any relaxation process mainly due to the compositional change of pure Al_2O_3 to mixed oxides at the interface. The samples thermally cycled for 100 and

250 cycles showed TGO resistance than 400 cycles due to the absence of enriched α-Al_2O_3 at the interface.

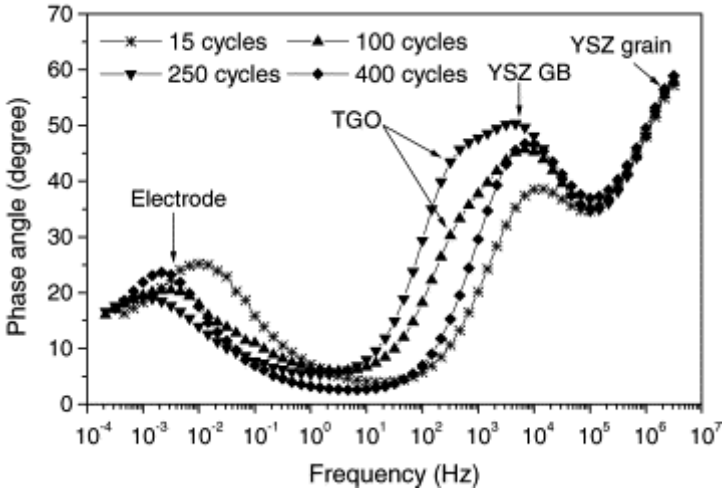

Fig. 2.16: Bode frequency plot of YSZ samples exposed to thermal cyclic test 1030 ˚C (Song et al. 2005).

Jayaraj et al. (2004) have reported EIS study of YSZ TBCs after isothermal and cyclic oxidation at 1100 ºC. They have noticed that large-scale spallation of top coat and TGO layer which could provide more electrolyte contact (0.01M $K_3Fe(CN)_6/K_4Fe(CN)_6.3H_2O$) with metallic bond coat surface, caused to an abrupt increase in the capacitance of top coat and TGO. TGO thickness was quantitatively calculated and correlated with capacitance. Fig. 2.17 (a) revealed that an increasing TGO growth was observed with an increasing oxidation time and this growth is inversely proportional to the capacitance. Fig. 2.17 (b) showed that the TGO growth gradually decreased with an increasing thermal cycles at 1121 ˚C. In addition, the gradual increase in capacitance of TGO corresponded to formation of defects such as large cracks and pores increased the conduction with metallic bond coat.

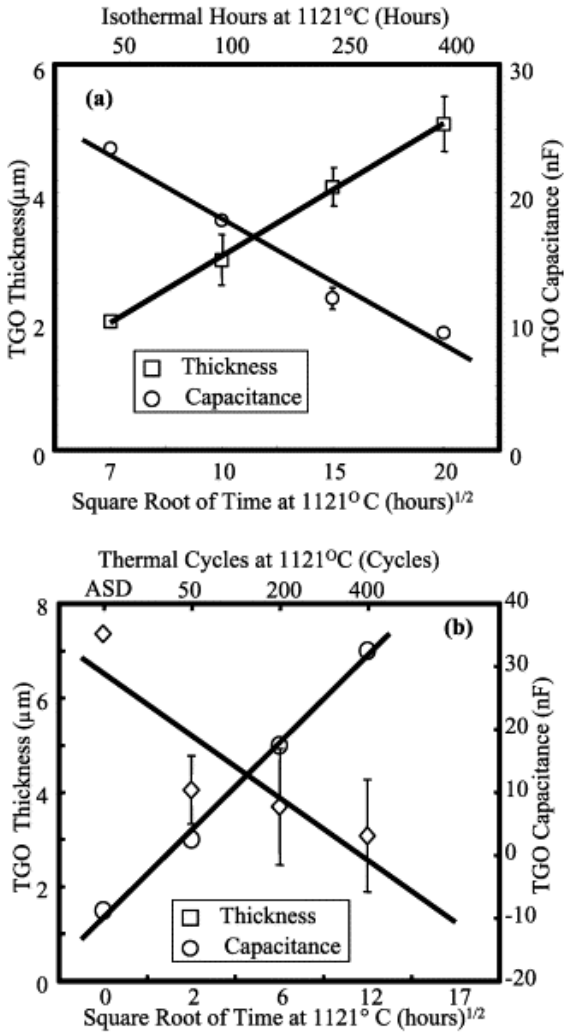

Fig. 2.17: TGO capacitance as a function of time of (a) isothermally oxidized EB-PVD; and (b) thermally cycled EB-PVD TBCs.

Zhang et al. (2005) have made a good correlation between impedance kinetics such as pore resistance, ceramic resistance, and ceramic capacitance with respect to the morphological structures of YSZ TBCs. The electrical resistance of top coat is directly proportional to its thickness, the presence of porosity, pore size, and shape distributions. Impedance analysis of 7YSZ TBCs during high-temperature oxidation test at 950 ºC was studied by Chen et al. (2016). The typical Nyquist and bode plots are presented in Fig. 2.18 (a) and (b) respectively.

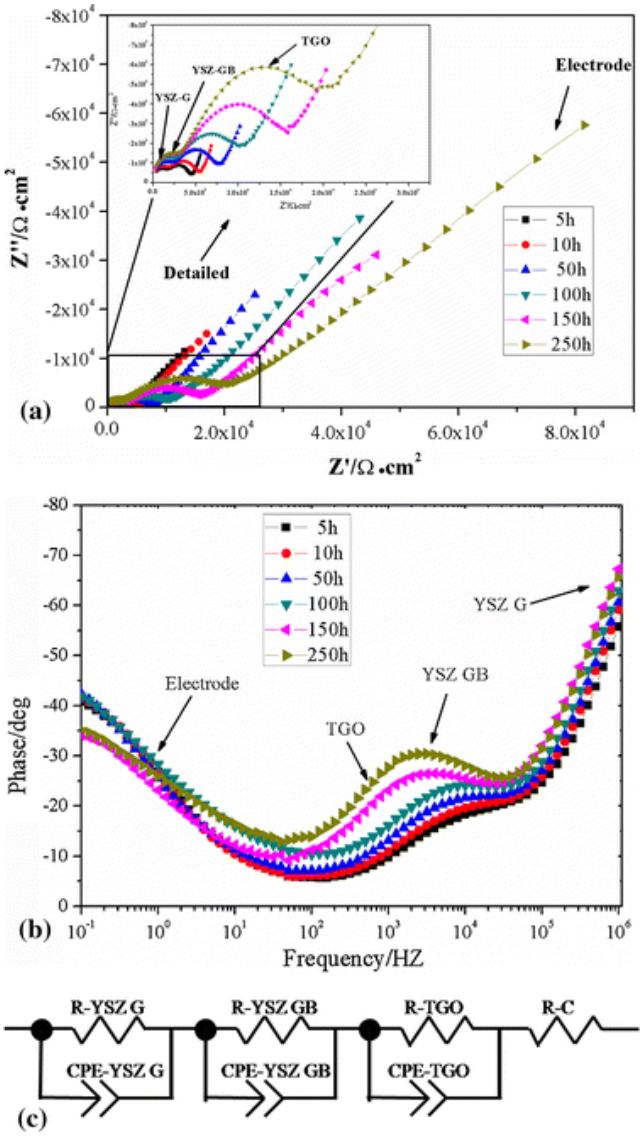

Fig. 2.18: (a) Nyquist; (b) Bode plot; (c) equivalent circuit model for YSZ TBCs after exposure to oxidation at 950 ˚C for different times (Chen et al. 2016).

They have found that at the beginning of oxidation time (<50 h) YSZ grain boundary resistance increased due to increasing cracks. Further, increasing oxidation time (>150 h) showed decreasing grain boundary resistance mainly due to sintering of ceramic top coat. But they did not notice an apparent change in capacitance of both YSZ grain and grain boundary at 950 ˚C. A correlation between Young's modulus of the ceramic top coat and electrochemical impedance was reported by Gomez-Garcia et al. (2009). The YSZ top coat crack resistance (R_{crack}) was increased up to a critical value 19 kilo Ohm after exposure to isothermal oxidation test at 1050 ºC for 75 h.

A reduction in R_{crack} was observed to be about 26% after exposure to 1050 ºC for 336 h. A linear relationship has been found between R_{crack} and Young's modulus as a consequence of sintering.

2.7 Hot corrosion behavior of TBCs

Hot corrosion is one of the high temperature material degradations in thermal barrier coatings (TBCs) through the chemical reactions of molten salts and ceramic top coat, especially with Na, S, and V from fuel impurities and Cl from marine atmosphere (Khajavi et al. 2004). These impurities can form Na_2SO_4 and V_2O_5 at elevated temperatures, which easily deposited on the surface of gas turbine blades. Hot corrosion can be classified into two forms namely high temperature (type I) and low temperature (type II) hot corrosion for operating temperature range 850-950 ˚C and 650-800 ˚C respectively (Eliaz et al. 2002). The chemical reaction of molten salts with metallic bond coat in TBCs also led to form non-protective oxide scales at the bond coat and ceramic top coat at the interface and this significantly affected delamination life of TBCs. The conventionally used YSZ ceramic TBC was found to undergo phase transformation to monoclinic ZrO_2 due to the reactions of molten salts with yttria stabilizer (Y_2O_3).

The Y_2O_3 leached out from YSZ and reacted with $NaVO_3$ (due to the combined reaction of Na_2SO_4+V_2O_5) to form YVO_4. The formation of $NaVO_3$ phase between Na_2SO_4 and V_2O_5 is shown in Fig. 2.19. The detailed reaction mechanisms of YSZ and Scandia stabilized zirconia (SSZ) with V_2O_5 reported by Jones (1997). It was found that the YSZ easily prone to hot corrosion than SSZ in vanadium containing engine environments. Hence, in order to improve the hot corrosion performance of conventional zirconia based TBCs several alternate ceramic materials and functionally graded composite coatings have been developed and tested at elevated temperatures. Xu et al. (2010) have studied hot corrosion behavior of rare earth zirconates ($La_2Zr_2O_7$ and $La_2Ce_2O_7$) and YSZ in the presence of Na_2SO_4 + V_2O_5 at 900 ˚C for 100 h. The basicity of La_2O_3 is relatively higher than CeO_2, so molten salts preferably attacked La_2O_3, while minimum attack was observed for CeO_2. The

CeO_2 containing TBC exhibited the best performance in hot corrosion than YSZ due to its low basicity.

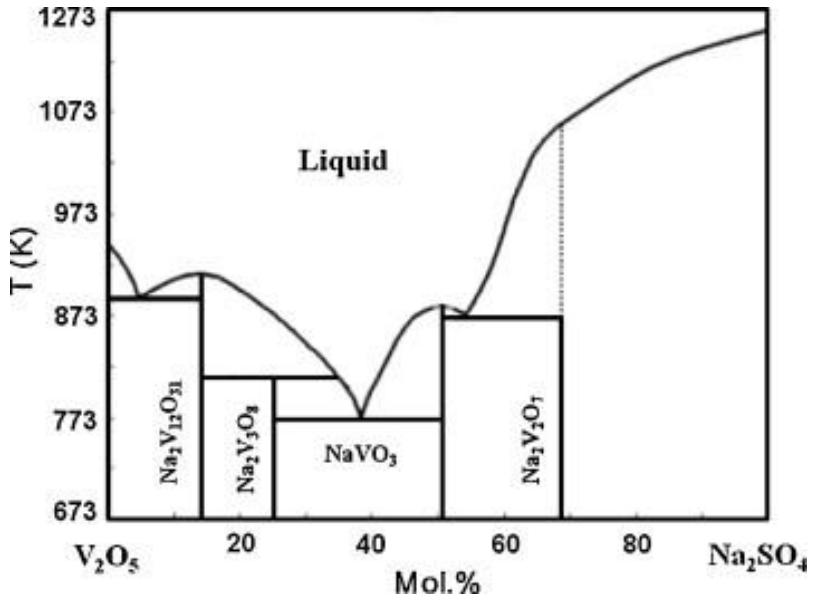

Fig. 2.19: Phase diagram of the Na_2SO_4-V_2O_5 system (Roth et al. 1981).

Hot corrosion of $LaTi_2Al_9O_{19}$ ceramic after exposure to V_2O_5 environment at 700-950 ˚C in air was studied by Zhou et al. (2016). It showed that degradation processes were significantly affected by temperature. At 700 ˚C for 10 h, $AlVO_4$, $LaVO_4$ and TiO_2 phases were identified as major corrosion products. However, at 800 ˚C, it was partially degraded into α-Al_2O_3 and θ-Al_2O_3 due to the instability of $AlVO_4$. Final corrosion products were composed of α-Al_2O_3, $LaVO_4$ and TiO_2 at 950 ˚C.

Vakiliford et al. (2017) have reported the hot corrosion behavior of functionally graded TBCs (mixture of NiCrAlY + YSZ) and duplex TBC (layered NiCrAlY/YSZ) in the presence of sodium and vanadium atmosphere at 800 ˚C for 120 h. They observed an significant improvement of hot corrosion performance of functionally graded TBC as compared to duplex TBCs due to the formation of $CrVO_4$ phase which postponed the phase transformation of t-ZrO_2 to m-ZrO_2.

Hot corrosion behaviors of Al_2O_3-clad YSZ coatings in vanadium-sulfate containing environments also studied by Zhong et al. (2010). The significant enhancement in hot corrosion resistance of Al_2O_3 clad YSZ was found than as

deposited YSZ coatings mainly due to chemical inertness and restrained molten salts by the dense clad layers. Summary of hot corrosion behavior of different ceramic top coat materials are listed in the Table 2.7.

Table 2.7: Hot corrosion performance of various top coat ceramic in different environmental conditions

S. No	Material	Environment/variable	Summary	Reference
1	Laser glazed plasma sprayed YSZ	Na_2SO_4 + V_2O_5 and corrosion testing at 910 ˚C / different wt.% of Y_2O_3 in YSZ phase	There are no significant corrosion cyclic life differences for TBC with various YSZ top coats for both plasma-sprayed and laser-glazed TBC. The lifetime decreased as the amount of deposited V_2O_5 salt increased.	Tsai et al. (2007)
2	YSZ, YSZ+Al_2O_3 and YSZ/Al_2O_3	A mixture of V_2O_5 and Na_2SO_4 and testing was done at 1050 ˚C for 40 h / protective effects of Al_2O_3 in YSZ using different methods	Monoclinic ZrO_2 fraction was lower in (YSZ + Al_2O_3) coating in comparison with usual YSZ. In the YSZ/Al_2O_3 system, the presence of a dense Al_2O_3 top layer on YSZ reduced the infiltration of molten salt and resulted in the further resistance of TBC against hot corrosion.	Afrasiabi et al. (2008)
3	$Yb_2Zr_2O_7$	V_2O_5 molten melt / hot corrosion test was performed at temperatures ranging from 600-800 ˚C in air	After thermal exposure to pure vanadate in a temperature range of 600-800 °C in air, different reaction products such as ZrV_2O_7, $YbVO_4$ and *m*-ZrO_2 are identified, depending upon the hot	Li et al. (2010)

			corrosion conditions.	
4	YSZ/ $LaMgA_{l1}O_{19}$	$Na_2SO_4 + V_2O_5$ mixtures with a hot corrosion test was isothermally conducted at 950 ˚C for 60 h / YSZ with different vol% of $LaMgA_{l1}O_{19}$	La_2O_3 is a stronger base than Y_2O_3 according to the innate Lewis acid-base natures for the solid inorganic oxide, so $LaVO_4$ will be firstly formed due to the degradation of LaMA coating during corrosion.	Chen et al. (2011)
5	YSZ, $Gd_2Zr_2O_7$ and YSZ+ $Gd_2Zr_2O_7$	$Na_2SO_4 + V_2O_5$ salt mixture and test temperature was at 1050 ˚C for 4 h / the hot corrosion performance of yttria stabilized zirconia (YSZ), $Gd_2Zr_2O_7$, and YSZ + $Gd_2Zr_2O_7$ comp osite coatings in the presence of molten mixture	In the case of YSZ, the reaction between $NaVO_3$ and Y_2O_3 produces YVO_4 and leads to the transformation of tetragonal (t') ZrO_2 to monoclinic (m') ZrO_2. For the $Gd_2Zr_2O_7$ + YSZ composite coating, by the formation of $GdVO_4$, the amount of YVO_4 formed on the YSZ + $Gd_2Zr_2O_7$ comp osite coating is significantly reduced. Molten salt also reacts with $Gd_2Zr_2O_7$ to form $GdVO_4$.	Habibi et al. (2012)
6	Ceria stabilized zirconia (C-YSZ)	$Na_2SO_4 + V_2O_5$ corrosive salt and hot corrosion test was conducted at 1000 ˚C for 30 h / hot corrosion response of ZrO_2-25 wt.% CeO_2-2.5wt.%	Molten salts were penetrated through coating micro-cracks and open pores and interacted with zirconia stabilizers (Y_2O_3 and CeO_2) to form	Ahmadi-pidani et al. (2012)

		Y_2O_3	YVO_4 and $CeVO_4$ rod-type crystals and CeO_2 semi-cubic crystals.	
7	YSZ and YSZ-Ta_2O_5	Hot corrosion test was done in the presence of $Na_2SO_4 + V_2O_5$ mixture at 1100 ˚C for 4 h / hot corrosion performance of YSZ and YSZ-Ta_2O_5 coatings	For YSZ, the reaction between $NaVO_3$ and Y_2O_3 produces YVO_4 and leads to the transformation of tetragonal ZrO_2 to monoclinic ZrO_2. For the Ta-YSZ sample, molten $Na_2SO_4 + V_2O_5$ mixture reacts weakly with the sample to form $NaTaO_3$, $TaVO_5$ and Ta_9VO_{25} after 80 h (20 cycles) of hot corrosion testing.	Habibi et al. (2013)
8	Conventional 8 wt.% YSZ and nanostructured 7 wt.% YSZ	Hot corrosion studies were performed in the presence of a molten mixture of $V_2O_5 + Na_2SO_4$ at 1000 °C for 30 h in air / Comparison of hot corrosion behaviors of plasma-sprayed conventional and nanostructured yttria stabilized zirconia (YSZ) thermal barrier coatings	The detrimental phase transformation of zirconia from tetragonal to monoclinic due to depletion of stabilizer from zirconia structure, and finally, creation of stresses resulting from formation of the monoclinic ZrO_2 and YVO_4 were recognized as degradation mechanisms of both coatings.	Jamali et al. (2014)
9	$SrZrO_3$ ceramic co-doped with Y_2O_3 and Yb_2O_3	$Na_2SO_4 + V_2O_5$ salt mixture / The hot corrosion behaviors of $Sr(Y_{0.05}Yb_{0.05}Zr_{0.9})O_{2.95}$ ceramic were investigated in Na_2SO_4, V_2O_5, and	$Sr(Y_{0.05}Yb_{0.05}Zr_{0.9})O_{2.95}$ ceramic reacted with molten V_2O_5 salt at 800 and 900 ˚C to form a porous layer consisting of m-ZrO_2, YVO_4, $YbVO_4$ and $Sr_3V_2O_8$.	Dong et al. (2014)

		$Na_2SO_4 + V_2O_5$ salts mixture at 900, 950 and 1000 °C for 10 h		

To minimize the attack of vanadate and sulfate on TBCs coatings, the addition of several elements such as Ca, Mg, Cr, Si, Al and Ni have been reported as inhibitors at higher temperatures (Kerby et al. 1973 and Rocca et al. 2003). The main principle of hot corrosion inhibition is to trap corrosive elements in the molten salts May et al. (1976) have reported the formation of abundant and hard refractory compounds using Ca based inhibitors. Mg was found to be a well known inhibitor for avoiding vanadium induced hot corrosion which gives MgO in the engine flame and reacted with V_2O_5 to form stable magnesium vanadate $Mg_3V_2O_8$ (Tiwari et al. 1998).

Hot corrosion inhibition of YSZ TBCs in the presence of MgO inhibitor was studied by Bajpai et al. (2015). It was concluded that the hot corrosion effect of V_2O_5 was minimized by MgO through the formation of $Mg_3V_2O_8$. Some researchers have studied the synergetic effect of Cr-Si on sodium induced hot corrosion process (Otsuka et al. 1990). Literature results also revealed that the melting point of Ni based refractory vanadate $Ni_3V_2O_8$ (1300 ˚C) is considerable higher than Mg based inhibitors (1200 ˚C) and reactivity of NiO with V_2O_5 is faster than MgO (Rocca et al. 2003). The hot corrosion inhibitions of TBCs by individual elements have been reported; however, the combined effect of Mg and Ni on sodium and vanadium containing environments are very limited in TBCs.

2.8 High temperature erosion behavior of ceramic TBCs

In TBCs, erosion resistance of top ceramic coat is highly desirable as it has a direct impact on the integrity of TBCs life time at higher temperature. Review of literature says that the erosion behavior of fully dense, un-porous ceramics has been widely studied but there is very few open literatures are available on porous ceramic system, especially top coat ceramic.

The steady state erosion rate follows a power law relationship. According to the literature, the derived relationship is given in Eq. 2.1 (Evans et al. 1978 and Weiderhorn et al. 1983) as:

$$V \propto v^a R^b H_t^c K_{ct}^d \quad (2.1)$$

Where V is the erosion rate, v is the impact particle velocity, R is the particle radius, H_t is the target hardness, K_{ct} is the target fracture toughness and a, b, c and d are constants. The determination of fracture toughness through indentation measurement of porous ceramics is found to be very complicated due to its complex microstructure of plasma sprayed TBCs. Some researchers have proposed new methods to find out the fracture toughness of plasma sprayed coatings other than indentations techniques. The erosion rates of solid bodies are majorly dependent on the ratio of hardness of target (H_t) to impacting particle (H_p). Shipway et al. (1996) have performed solid body erosion test on ceramic targets with different erodent particles and concluded that the erosion rate strongly depends on target hardness than fracture toughness of materials. Janos et al. (1999) have studied effect of thermal aging on the erosion resistance of air plasma sprayed thermal barrier coating (shown in Fig 2.20). They have found that erosion resistance and micro hardness of TBCs increased with the increased thermal aging temperature and decreased due to increment of porosity in the top ceramic coat.

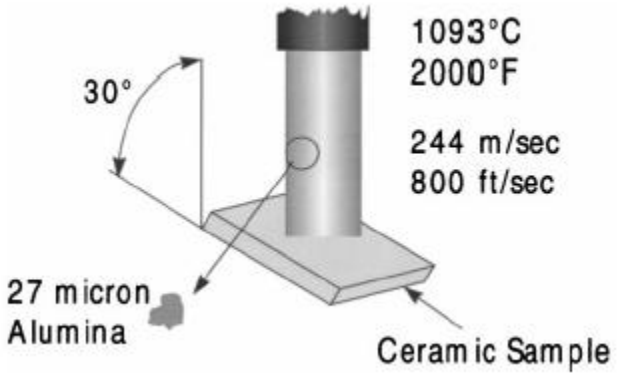

Fig. 2.20: High temperature air jet erosion set up (Janos et al. 1999).

The erosion test was conducted using 27 µm medium size alumina grits as an erodent material. The angle of incident was set to 30˚ (Fig. 2.20), temperature and velocity of impingement was set to 1093 ˚C and 244 m s^{-1} respectively. An increase in erosion rate with an increase in porosity was observed, however, the significant

reduction in erosion rate was also observed after thermal ageing treatment over as sprayed condition (Fig. 2.21).

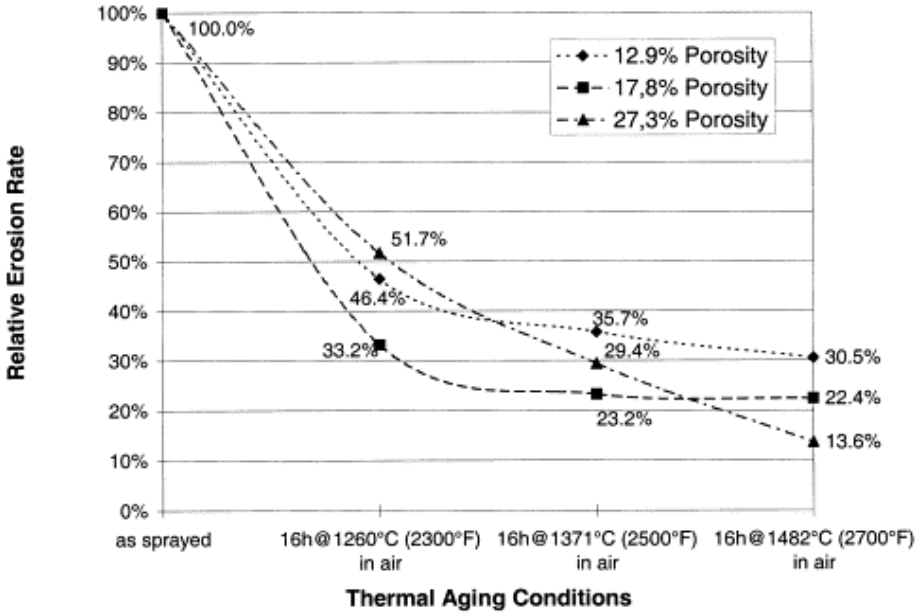

Fig. 2.21: Relative improvement in erosion resistances of thermally aged samples compared to as-deposited TBCs (Janos et al. 1999).

Tsai et al. (2007) have adopted laser glazing process on the plasma-sprayed ceramic TBC layer to improve the erosion resistance. Laser glazing process improved the erosion resistance of plasma sprayed TBCs by about 1.5 to 3 times with the impingement angle ranging between 30 and 60˚ (Fig. 2.22).

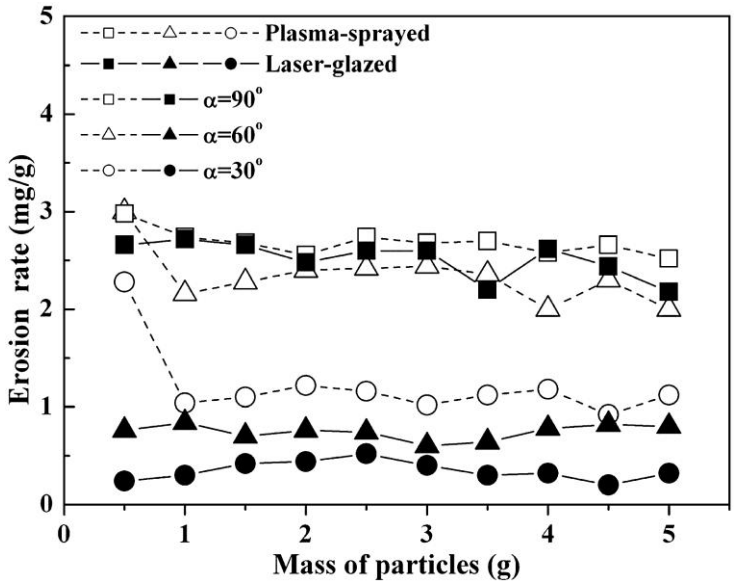

Fig. 2.22: Incremental erosion rates of laser glazed and plasma sprayed TBCs at different impingement angles (Tsai et al. 2007).

2.9 Research gap in the literature survey

Review of the literature survey says that the phase transformation of YSZ from tetragonal (t-ZrO_2) to monoclinic (m-ZrO_2) occurred during cyclic oxidation and after exposure to hot corrosion in vanadates and chlorides salt which resulted 3-5% volume change within the coating and it caused catastrophic failure of TBCs at the temperatures of 900-1200 ˚C. Hence, much effort has been directed in the last few decades to seek for new ceramic material with better thermal-physical properties than YSZ.

2.10 Scientific basis of the proposed work

In contrast to other materials, the Sm based aluminate is characterized by high melting points, low thermal conductivity, high thermal expansion coefficients and high temperature phase stability (Feng et al, 2012, Wan et al, 2010). The thermal conductivity and thermal expansion coefficients of different aluminates are shown in the following Figs. 2.23 and 2.24 respectively.

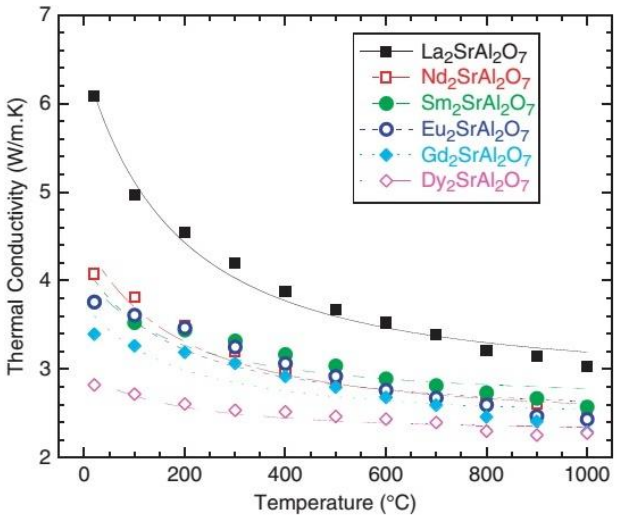

Fig. 2.23: Thermal conductivity of the strontium aluminates as a function of temperature (Wan et al. 2010).

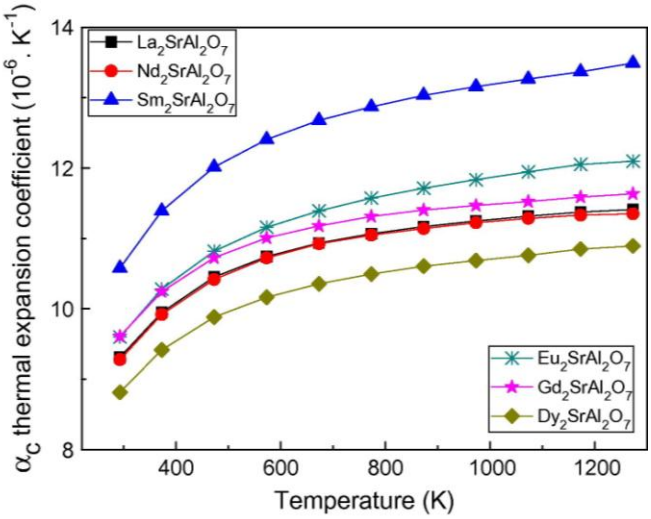

Fig. 2.24: Linear thermal expansion coefficient of $Ln_2SrAl_2O_7$ compounds as a function of temperature. Note: α_c in this plot indicates thermal expansion in c direction of the tetragonal unit cell (Feng et al. 2012).

Rare earth strontium aluminates additionally offer the possibility of extensive substitution of ions at the Ln site, which enables the properties of the materials to be tailored. The large thermal expansion of the Sm based oxide compound makes it particularly attractive, as it is amongst the least anisotropic. The thermal expansion of samarium strontium aluminate is found to be about 13.5-13.8×10^{-6} K^{-1}, which is

higher than plasma sprayed 8%YSZ (10.7×10^{-6} K^{-1}) at 1000 ˚C. Hence, Sm based aluminate can be proposed as an alternate top coat ceramic against YSZ material to minimize the sharp discontinuities in thermal expansion mismatch.

Fig. 2.25 shows the comparison of thermal conductivity and thermal expansion of different TBC material tested at 1000 ˚C. In addition to perovskite family (ABO_3) and pyrochlores ($A_2B_2O_7$) the other interesting materials like rare earth strontium aluminates ($Ln_2SrAl_2O_7$) are also cover the most favorable range of thermal conductivity and thermal expansions for TBCs applications, i.e. low thermal conductivity and high coefficient of thermal expansion.

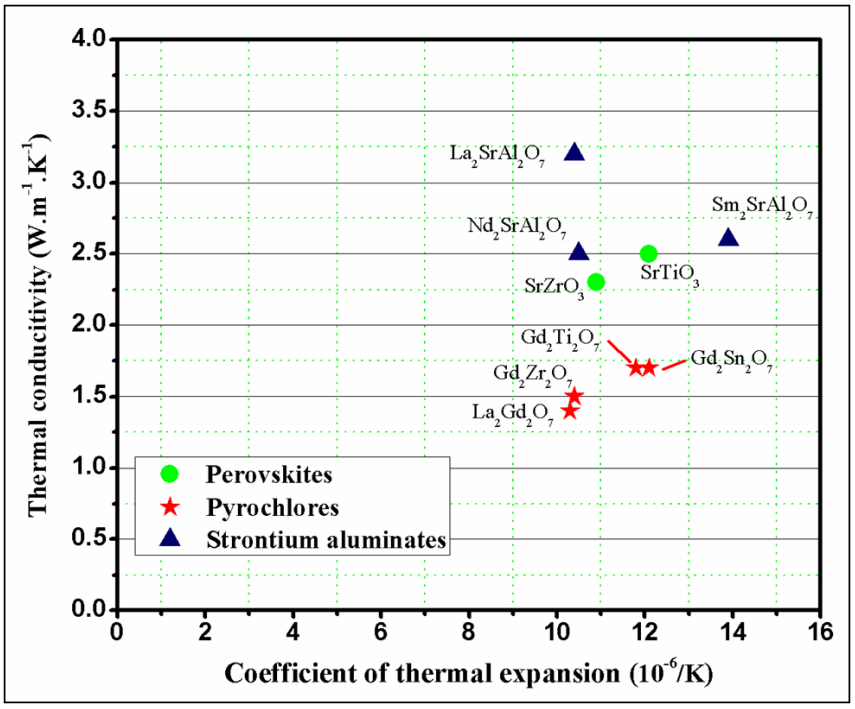

Fig. 2.25: Plot of thermal conductivity versus coefficient of thermal expansion of new thermal barrier coating materials (Vaβen et al. 2010).

Such materials synthesis and the development of strategically design for TBC are sparse. From the literature review it is also clear that plenty of investigations have been extensively studied to analyze the failure of TBCs caused by TGO growth, thermal expansion mismatch, oxidation of bond coat, and so on. However, it is not

clear that how the TGO affects (thickness) affects the oxidation behavior of TBCs at elevated temperature.

Hence, this work will address two important challenges in the field. The first one is to synthesis, develop SSA based TBCs, the role of TGO thickness and purity on the oxidation behavior of the alternate SSA ceramic vis-à-vis conventional YSZ TBCs at high temperature (900-1200 ˚C). The second is to study the hot corrosion and high temperature erosion behavior of new SSA TBCs at elevated temperatures (500-1200 ˚C).

CHAPTER 3

3 EXPERIMENTAL DETAILS

This chapter describes about the equipment used and procedures followed for synthesis, development of thermal barrier coatings, pre-oxidation, oxidation, electrochemical impedance study, hot corrosion and high temperature erosion studies and relevant characterization for analysis of oxidation and hot corrosion products. The schematic representation of the work flow is shown in Fig. 3.1.

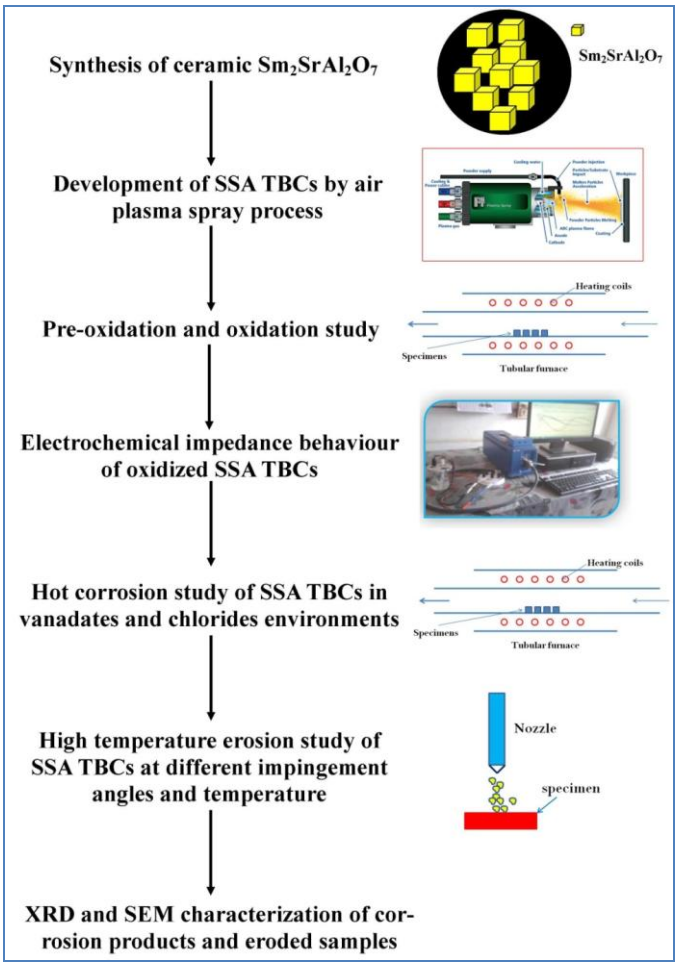

Fig. 3.1: Schematic representation of experimental details.

3.1 Synthesis of ceramic SSA ceramic by molten salt method

Samarium oxide (Sm_2O_3, 99.9%), Strontium carbonate ($SrCO_3$, 99.0%) and Aluminium oxide (Al_2O_3, 99.9%) were used as a starting precursor materials for the synthesis of SSA ceramic. These oxides were mixed with 0.5:0.5 eutectic compositions of potassium chloride (KCl, 99.5%) and sodium chloride (NaCl, 99.5%) for 30 min in an agate mortar. The mixture was placed in the alumina crucible and then heated up to 1100 ºC for 24 h. Final products were continuously washed with hot deionized water to remove the salts. The obtained products were further dried in the hot air oven at 120 ºC for 6 h.

3.2 Deposition of SSA ceramic by air plasma spray process

3.2.1 Substrate materials and feed stocks used for coating preparation

Ni based superalloy (Inconel 718) was as a substrate material and procured from M/s. Narendra steels, Mumbai, India. The chemical composition of the substrate is given in Table 3.1. The size of 20 mm × 20 mm × 5 mm specimens were cut from sheet and was used for plasma spraying process.

Table 3.1: Chemical composition of Inconel 718 (wt. %).

Ni	Fe	Cr	Nb	Mo	Ti	Al	Mn	Co
54.02	17.65	17.60	5.10	2.98	0.80	0.26	0.30	0.48

All the samples were ground using emery papers and subjected to alumina (Grit 45) grit blasting prior to the coating process. The chemical composition of NiCrAlY bond coat is provided in Table 3.2.

Table 3.2: Chemical composition of NiCrAlY (wt. %).

Ni	Cr	Al	Y
68.29	21.41	10.27	0.93

NiCrAlY bond coat (~50 µm thickness) was deposited on grit blasted substrate by air plasma spray technique using a 55 kW F4-MB plasma gun (Metallizing Equipments Company Pvt. Ltd, Jodhpur, India). The plasma is created between anode and cathode and the feed stock is fed into plasma plume from powder feeder. The quality of plasma spray coating depends on the particle size and morphology of spray feed stocks. The reported optimum particle size for plasma spray process is around 30-50 µm in order to melt completely and to achieve a lower time of melting. The surface roughness (R_a) of as deposited bond coat was found about 12 µm using an optical profilometer having accuracy of ±1 µm. The precise spray conditions and plasma spray parameters for both bond coat and top coats are given in Table 3.3.

Table 3.3: Plasma spray parameters for both bond coat and ceramic top coat materials.

Parameter	NiCrAlY	SSA	YSZ
Particle size (µm)	-112/+53	-75/+2	-140/+15
Power (kW)	33	35.5	35.5
Spray distance (mm)	110	100	100
Working gas, Ar (m^3/h)	2.28	2.28	2.28
Working gas, H_2 (m^3/h)	0.48	0.6	0.6
Carrier gas, N_2 (m^3/h)	0.30	0.28	0.28
Feed rate (g/min)	45	30	30
Anode-nozzle internal diameter (mm)	6	6	6
Injector position (deg.)	90	90	90
Injector internal diameter (mm)	1.8	1.8	1.8

The SSA ceramic was synthesized in the laboratory using molten salt method. The ceramic top coat materials such as SSA and YSZ (used as reference) were separately sprayed on the bond coat surface using APS technique. The average particle size of used SSA and YSZ powder is approximately 45 and 60 µm, respectively. The thickness of bond coat and top coat are obtained between 50-100 and 100-200 µm respectively. The thicknesses of bond and top coat were selected

based on the works reported previously and availability of SSA ceramic. The particle size of commercial grades 8%YSZ (PAC 2008P) and NiCrAlY (PAC 9620AM) were provided by M/s. Powder Alloy Corporation, Ohio, USA. The particle size of synthesized SSA powder was calculated by sieve analysis according to ASTM B-214.

3.3 Pre-oxidation and oxidation study

The pre-oxidation treatment of the SSA and YSZ coated TBCs specimens were carried out in the presence of high purity argon (99.999%) atmosphere at 1050 ºC (Li et al. 2009 and Dong et al. 2014). Specimens were pre-oxidized at 1050 ºC for 10, 20, and 30 h to get TBCs with different TGO thicknesses in the Ar atmosphere prior to oxidation test under air.

Isothermal oxidation study was performed at 1100 ºC for 15 h in air using a resistance controlled tubular furnace with ±1 ºC accuracy. The weight gain measurement was made at the interval of 5 h using a semi-microbalance having the accuracy of around ±0.0001 g. Three specimens were tested for each condition to obtain the average weight gain values during oxidation test.

3.4 Electrochemical impedance measurement of SSA TBCs

The conventional three electrode system was employed for EIS measurement, consists of a reference electrode (saturated calomel electrode-SCE), a platinum counter electrode and working electrode. Oxidized TBC specimens were acted as working electrode and the same were prepared in the following manner. One side of the oxidized specimen was mechanically polished to remove the TBC layer and acting as one electrode. The TBC side of the specimen was immersed in an aqueous electrolyte containing 0.01 M $K_3Fe(CN)_6/K_4Fe(CN)_6.3H_2O$. Particularly, this electrolyte was taken because of its highly reversible exchange current density and minimal interference with the system (García et al. 2009). Electrochemical impedance measurement was conducted using potentiostat with an impedance analyzer (Biologic, SP-150, France), which is computer controlled.

Spectral analysis or curve fitting was performed using EC-Lab impedance analysis software attached to the instrument to get the electrical properties (resistance and capacitance) of TBC system. In the EIS measurement, the AC amplitude of 20 mV and frequency in the range of 10^{-3} Hz to 10^{5} Hz was employed.

3.5 Residual stress measurement of the SSA TBCs

The residual stresses of the SSA TBCs were analyzed using micro-Raman spectroscopy (Jobin-Yvon) with an argon ion laser (532 nm) and exciting light source with 4 mW power. The residual stresses were calculated based on peak shifts of Raman bands due to stresses and conversion of these band shifts to stress values by the use of tensor coefficients (Li et al. 2012 and Tomimatsu et al. 2003). The relation between the bi-axial residual stress and peak shift of a given Raman band by

$$\text{Average stress tensor } \sigma = -b\Delta\Omega \qquad (3.1)$$

Where $\Delta\Omega = \Omega - \Omega_o$ and Ω_o are the position of selected Raman line for the stress-free sample. In the present work, the strong Raman line at 320 cm^{-1} was used to determine the residual stress and variation of $\Delta\Omega$ at 320 cm^{-1} was used to indicate the variation of stress in the TBCs.

3.6 Hot corrosion test and resistance assessment

The TBCs samples were pre-heated at 200 ˚C for 30 min to get a good adhesion of salts on the coating surface. A two types of salt mixture such as 50 wt.% Na_2SO_4 + 50 wt.% V_2O_5 and 90 wt.% Na_2SO_4 + 5 wt.% V_2O_5 + 5 wt.% NaCl powder were prepared and dissolved in distilled water to get a salt slurry which was applied over the coating surface. Further samples were dried at 120 ˚C for 2 h to remove the moisture and weighed to find out the amount of salts on the sample surface. The salt coverage was found to be in the range of 17-20 mg/cm^2.

The salt coated specimens were placed in the even temperature zone of tubular furnace with the accuracy of ±1 ˚C and heated at 700 and 900 ˚C. The specimen

surface was examined in every 10 h of hot corrosion by cooling the furnace to room temperature. If any coating spllation (>20%) observed on the sample surface, that particular specimen was removed and then the test was continued for remaining samples. The interval time was reduced to 2 h for remaining samples in order to predict the exact coating spallation time. After test the specimens were removed and washed with water and dried.

3.7 Characterization of ceramic powders and coating

A detailed phase of the synthesized ceramic powder and oxidized TBC samples were analyzed using X-ray diffractometer (JEOL DX GE-2P, Japan) with Cu K_α (λ=1.514 Å) radiation at an accelerating voltage of 30 kV and 20 mA. All the samples were scanned at a speed of 2 deg. min^{-1}.

X-ray Photoelectron Spectroscopy (XPS) being used to examine stoichiometry of synthesized SSA (ESCALAB MkII, VG Scientific). Al Kα radiation (12 kV, 6 mA) was used to excite Sm 4d, Sr 3d, Al 2p, and O 1s electron from as-synthesized SSA. The obtained spectrum was calibrated with C 1s line at 285 eV.

High-resolution SEM (EVO 18, Carl Zeiss, Germany) was used for morphological and cross-sectional studies of synthesized powder and oxidized specimens. For cross sectional study, the specimens were cold mounted with epoxy resins and subjected to slow speed diamond cutting using diamond saw. The specimens were further polished with 300 to 1200 grade SiC emery papers, 0.5 µm diamond paste, cleaned with distilled water and dried. Energy Dispersive X-ray Spectroscope (EDS) was used for the compositional analysis of ceramic powder and coatings.

3.8 High temperature erosion test

High temperature erosion test was conducted in air jet erosion test rig (Fig. 3.2) at three different temperatures such as 200, 500 and 800 ˚C according to ASTM G 76-13 at the Ducom Instruments, Bengaluru, India. The erosion test was performed

on as deposited and pre-oxidized SSA TBCs. The conventional YSZ ceramic was also studied for comparison purpose. The testing conditions followed in the present study are reported in Table 3.4.

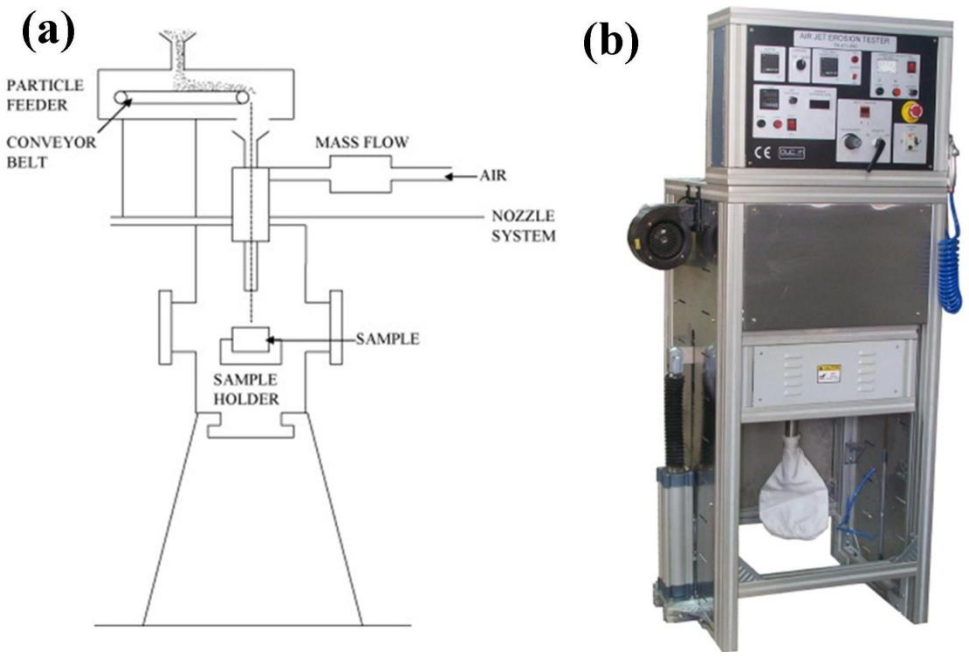

Fig. 3.2: (a) Line sketch and (b) Photographic image of high temperature erosion tester (Ramesh et al. 2010).

Table 3.4: Erosion test parameters used for SSA and YSZ TBCs

Test parameter		Specifications
Air	Discharge	2 gm/min
	Velocity	30 m/s
Specimen	Size	20 × 20 ×5 mm
	Erodent material	Alumina
	Erodent size	50 µm
	Temperature	200, 500, and 800 ˚C
	Angle of impingement	30 and 90˚
Nozzle	Size	ID: 1.5 mm, OD: 15 mm and 50 mm long
	Material	99.9 % pure alumina

Initially the as deposited and pre-oxidized SSA and YSZ specimens were cleaned with de-ionized water in ultrasonic cleaner, dried and weighed. Then the sample was loaded in to the sample holder of erosion tester and eroded with alumina particles at the pre-determined velocity, feed rate, impingement angle and temperature. The final mass of specimens was measured to calculate the weight loss. The mass loss of the specimens were normalized by testing time and feed rate of erodent causing weight loss (testing time × erodent feed rate). Then the erosion rate of SSA and YSZ TBCs were calculated for g/g of alumina impingement (Ramesh et al. 2010).

3.9 Measurement of mechanical properties

The mechanical properties such as Young's modulus, hardness and stiffness were measured by Nano-indentation technique. All the experiments were conducted in the load controlled mode using a Hysitron Tribo-indenter fitted with a Berkovich indenter at room temperature on pre-oxidized SSA TBCs.

RESULTS AND DISCUSSION

CHAPTER 4

4 OXIDATION STUDIES

Much research works have been done to improve the bond coat oxidation resistance by changing the bond coat alloy and modifications in the coating processes. In addition to this modifying the conventional top coat ceramic material has also been effective in improving the oxidation resistance of TBCs. In the present study, SSA ceramic based TBC was developed and its oxidation behavior examined vis-à-vis conventional YSZ.

4.1 Characterization of SSA ceramic powder

The XRD pattern of SSA ceramic powder is shown in Figs. 4.1 (a), (b) and (c) for as synthesized [4.1 (a)], annealing of same powder for 15 h [4.1 (b)] and 168 h [4.1 (c] at 1300 ºC, respectively. Lattice parameters and intensity ratio obtained from the XRD plots [Figs. 4.1 (a)-(c)] are shown in Table 4.1.

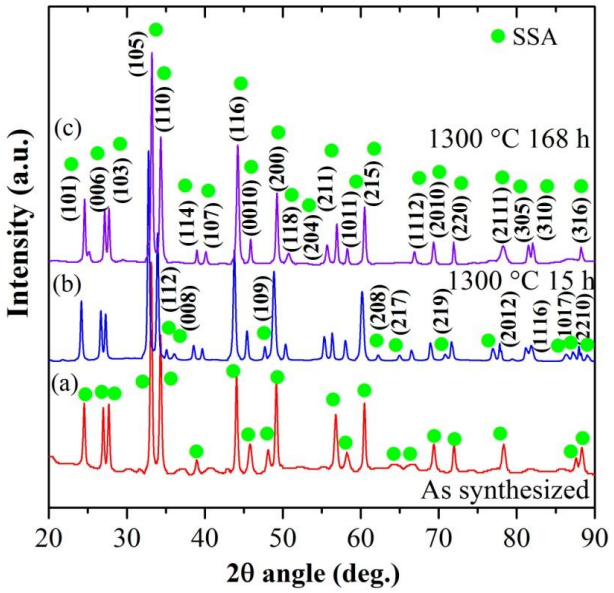

Fig. 4.1: XRD patterns of (a) as synthesized; (b) powders annealed at 1300 ºC for 15 h; and (c) 168 h.

Fig. 4.1 (a) shows that the presence of a single phase BCT (body centered tetragonal) system with double perovskite structure (Zverera et al. 2003). A weak peaks with low intensities (<10%) at 2θ values and corresponding planes such as (112), (008), (208), (217), (219), (1116) and (1017) were not seen in as synthesized SSA as compared to annealed powders at 15 and 168 h for 1300 ºC. This is because of low-temperature processing (1030 ºC) and used time (48 h) for the synthesis of SSA powder, which are not sufficient to form complete SSA crystal. Lin et al. have done the low-temperature synthesis of $LiNbO_3$ ferroelectric materials at different temperatures ranging from 650 to 800 ºC for 3 h. They were found that with the increase in temperature, the diffraction peaks intensity increases gradually. It indicates an increase of temperature leads to increase the particle size (Lin et al. 2008).

Table 4.1: Intensity ratios of XRD peaks of SSA powder with different heat treatments.

		Intensity ratio, I_{105} = 100						
Sample	c/a ratio	I_{101}	I_{103}	I_{110}	I_{116}	I_{200}	I_{1011}	I_{215}
(JCPDS # 760095)	5.37	33	38	65	32	33	14	27
As synthesized	5.24	25	29	63	54	47	24	36
Powder,1300 ºC, 15 h	5.34	26	16	41	44	31	12	28
Powder,1300 ºC, 168 h	5.36	36	24	65	47	29	14	34

Similarly, SSA powder was subjected to use annealing process at 1300 ºC for 15 h which is shown XRD plot [Fig. 4.1 (b)]. It was observed that a formation of new SSA peaks corresponds to planes (112), (008), (109), (208), (217), (219), (2012), (1116), (1017), and (2210). As the time increased to 168 h, a major phase changes or destabilization and decomposition of SSA powders were also not observed. It clearly showed that a high-temperature thermal stability of developed ceramic powder. With the increase in dwelling time from 15 h to 168 h, the diffraction peaks intensity of few major planes such as (101) and (110) gradually increased about 35 % due to the particle growth (Table 4.1) (Lin et al. 2008). Further, the calculated c/a ratio from

XRD data found to be increased a trivial with an increase in annealing time (shown in Table 4.1). The SSA powder after 1300 ºC for 168 h treatment has a **c/a** ratio of 5.360 Å, which is 0.18% lower than that of pure SSA phase, indicating that no loss of composition or vacancy formation even at higher temperature treatment (Zverera et al. 2003). The EDS analysis of synthesized SSA powder is shown in Table 4.2. It is observed that the atomic ratio among Sm, Sr, Al, and O followed in the range of 2:1:2:7, which also confirms the formation of SSA phase.

Table 4.2: EDS analysis of the SSA powder (at. %).

	Sm	Sr	Al	O	Chemical formula
Synthesized powder	15.60	5.72	19.36	59.33	$Sm_2SrAl_2O_7$
Error (%)	0.25	0.14	0.05	0.05	

A wide and high-resolution XPS spectrum of Sm, Sr, Al, and O are shown in Figs. 4.2 and 4.3 respectively. The major elements such as Sm, Sr, Al, and O were observed without any other impurities (Fig. 4.2). The binding energy (BE) at 284.6 eV corresponded to C 1s which is generally used as internal reference spectra (Fig. 4.2). The BE values at 976 eV and 1224 eV are more evident Auger peaks of O and C respectively (Hecht et al. 2007). Fig. 4.3 (a-d) shows the high resolution XPS scan of Sm 3d, Sr 3d, Al 2p and O 1s. The Sm 3d peaks such as Sm $3d_{5/2}$ and Sm $3d_{3/2}$ were found at two distinct BE of 1084.3 eV and 1111.5 eV. The BE difference between these two peaks (27.2 eV) clearly indicated the +3 oxidation state of Sm ion (Table 4.3).

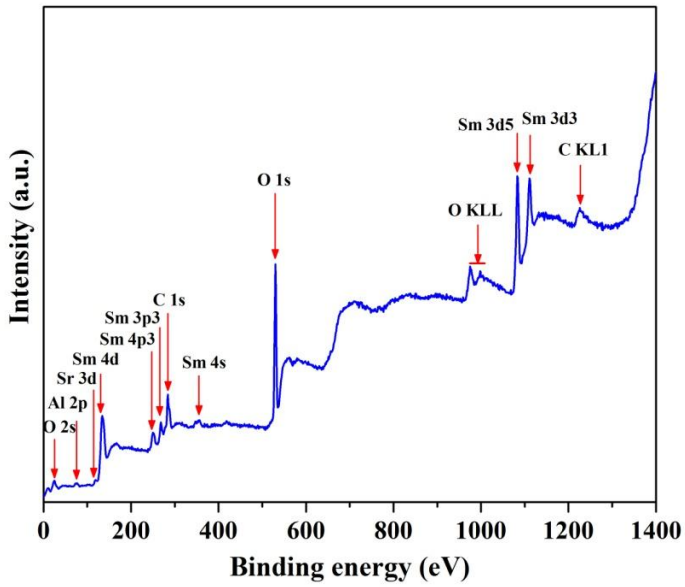

Fig. 4.2: XPS survey spectra of as-synthesized SSA ceramic powder.

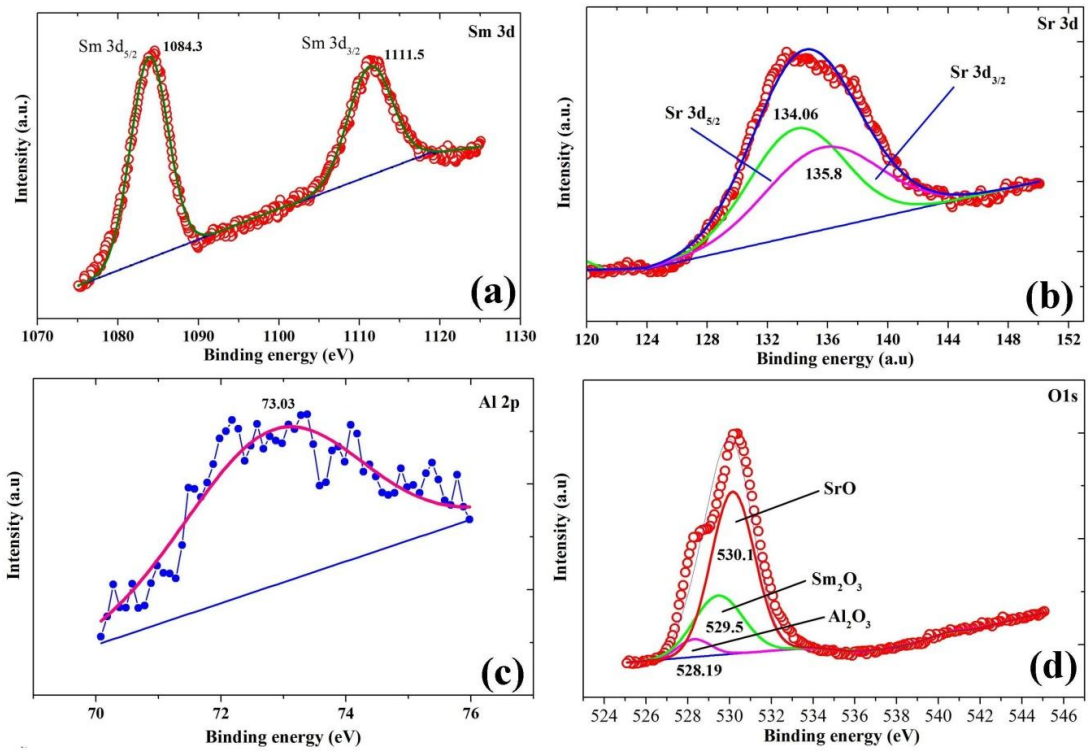

Fig. 4.3: Deconvoluted high resolution spectra of SSA ceramic powder: (a) Sm 3d; (b) Sr 3d; (c) Al 2p; and (d) O 1s.

Table 4.3: Binding energies of Sm 3d, Sr 3d, Al 2p and O 1s of synthesized SSA powder.

	Binding energy (eV)		Compound formation	
Electron level	Experimental value	Reference value	Experimentally observed	References
Sm $3d_{3/2}$	1111.5	1110.9	Sm_2O_3	(Petrov et al. 2010)
Sm $3d_{5/2}$	1084.3	1083.4		
Sr $3d_{3/2}$	135.8	135.5	SrO	(Vasquez et al. 1991)
Sr $3d_{5/2}$	134.06	133.5		
Al 2p	73.03	74.50	Al_2O_3	(Gillet et al. 1992)
O 1s	528.19	528.73	Al_2O_3	(Reddy et al. 2014)
O 1s	529.50	530.40	Sm_2O_3	(Wagner et al. 1979)
O1s	530.10	530.20	SrO	(Wang et al. 2008)

The symmetry of Sm peak indicates that the presence of samarium ions in +3 valence state (Sm^{3+}). Two Gaussian peaks of Sr 3d peak were found at 134.06 eV and 135.8 eV corresponded to Sr $3d_{5/2}$ and Sr $3d_{3/2}$ lines, respectively in the SrO. The high resolution scan of Al (Al 2p) is shown in Fig. 4.3 (c) and this characteristic peak found to be at a BE of 73.03 eV. The BE values of O 1s peaks at 528.19, 529.50 and 530.10 eV revealed the presence of Al-O, Sm and /Sr-O bonds respectively. All noticed BE values of Sm_2O_3, SrO, and Al_2O_3 compounds have shown good agreements with literature data's which are given in Table 4.3.

4.2 Surface morphology before and after coatings

4.2.1 Bond coat (NiCrAlY), SSA and YSZ powders

Microstructures of commercial metallic NiCrAlY alloy and ceramic powders of YSZ and SSA which are used as top coats are shown in Figs. 4.4 (a), (b) and (c), respectively. Figs. 4.4 (a) and 4.4 (b) were shown spherical shape of NiCrAlY and YSZ respectively. Synthesized SSA ceramic powder was found to be cuboidal shapes [Fig. 4.4 (c)].

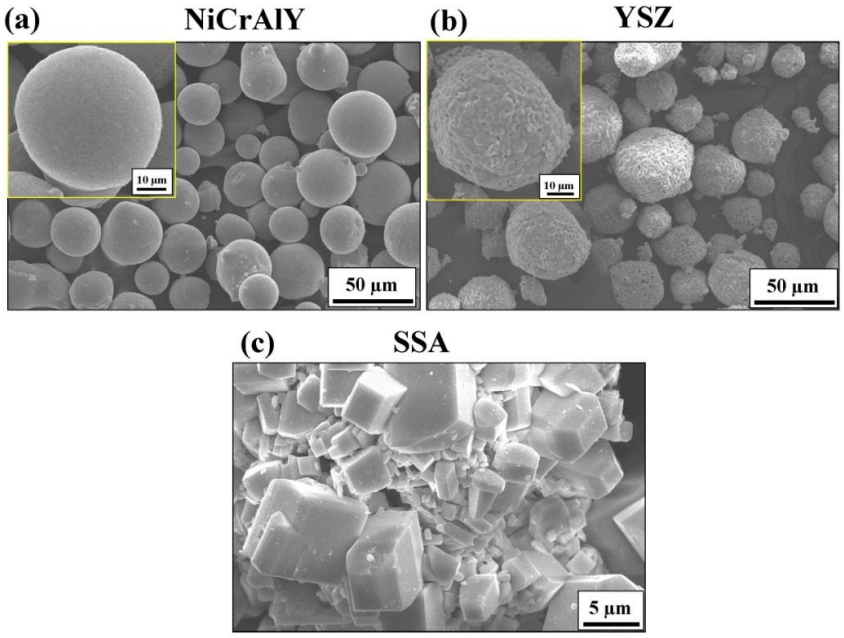

Fig. 4.4: SEM morphology of the powder: (a) NiCrAlY alloy; (b) YSZ; and (c) SSA.

Powder characteristics such as morphology and size distributions directly affect the mechanical and thermal behavior of coatings at higher temperature (Tan et al. 2012 and Dwivedi et al. 2014). However, present research work is primarily focused on the oxidation behavior of newly developed SSA ceramic vis-à-vis conventionally used YSZ. So, the effect of morphology and the sizes of SSA powder on mechanical and other behaviors were assumed to be similar as like conventionally used YSZ material.

4.2.2 Microstructure and XRD analysis of coated YSZ and SSA:

The surface morphologies of as deposited YSZ and SSA top coats are shown in Figs. 4.5 (a) and 4.5 (b) respectively, at lower magnification. These figures have clearly revealed the presence of uneven surfaces due to the formation of several splats (pancake shape of deformed molten particle), pores and micro-cracks. SEM image of SSA top coat at higher magnification is shown in Fig. 4.5 (c). These microstructures consist of semi-melted particles, porosities, and micro-cracks due to improper melting and solidification of ceramic particles. The presence of these features is found to be

beneficial for thermal barrier coating due to enhancement of strain tolerance ability of coatings at high temperature (Guo et al. 2006 and Wang et al. 2003).

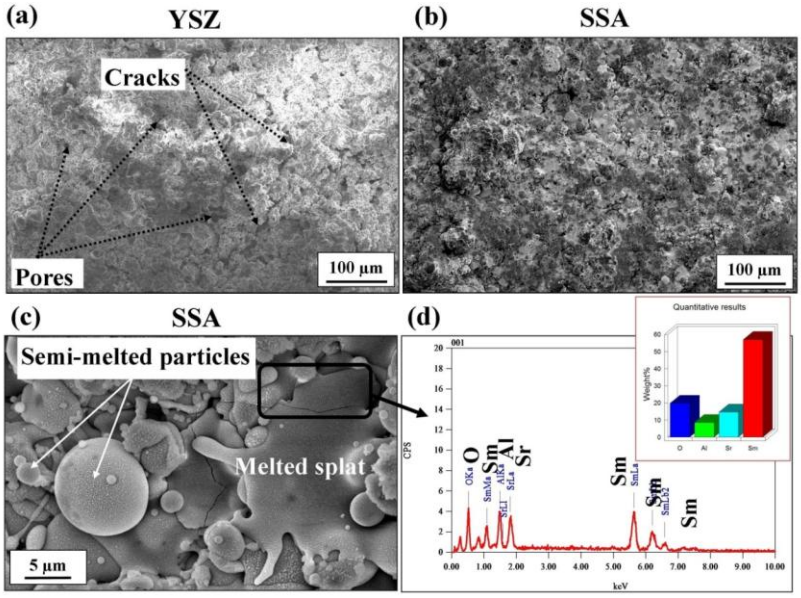

Fig. 4.5: Scanning electron micrographs of the as-deposited top surface of TBC: (a) YSZ; (b and c) Low and high magnification view of SSA; and (d) EDS spectrum of SSA.

The EDS analysis was carried out to distinguish the chemical composition of SSA after deposition by APS technique [Fig. 4.5 (d)]. The elemental compositions (at.%) of Sm, Sr, Al, and O were found to be about 18.54, 8.08, 16.79 and 53.74 respectively. These obtained values are very much similar to the calculated stoichiometry ratio of SSA and also confirmed that the absence of any other compounds (impurities) formation during the processing of SSA ceramic top coat (Table 4.2).

The XRD pattern of as deposited SSA TBCs is shown in Fig. 4.6. It was found that the presence of samarium strontium aluminate single phase (BCT) on the top surface of the coating. Additionally, intensity changes of some major peaks were observed at 24.5, 26.9, 44.02, 49.17 and 60.4^{o} due to rapid crystallization of SSA melt when it is deposited on the substrate (Cao et al. 2001). A typical cross sectional SEM micrographs of as deposited YSZ TBC and as deposited SSA TBC are shown in Fig.

4.7 (a) and Fig 4.7 (b) respectively. EDS spectrum obtained from both the figures are shown as YSZ top coat (Fig 4.7 c), NiCrAlY in YSZ TBCs Fig. 4.7 d), SSA (Fig. 4.7 e), and NiCrAlY in SSA TBCs (Fig 4.7 f). The presence of flattened particles (splats) that are parallel to the substrate base, globular pores/voids, and interparticle cracks were clearly seen in Fig. 4.7 (a). The heterogeneous distribution was obtained for SSA TBCs such as micro-pores (region 1), inter-lamellar pores (region 2), intra-lamellar cracks (region 3) and inter-lamellar cracks (region 4), are shown in Fig. 4.7 (b).

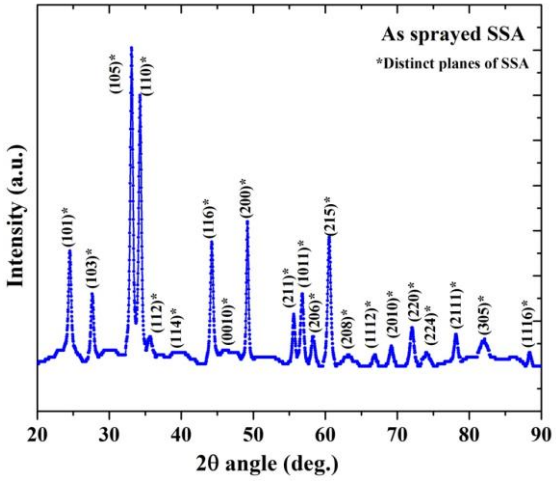

Fig. 4.6: XRD pattern of as-deposited SSA ceramic.

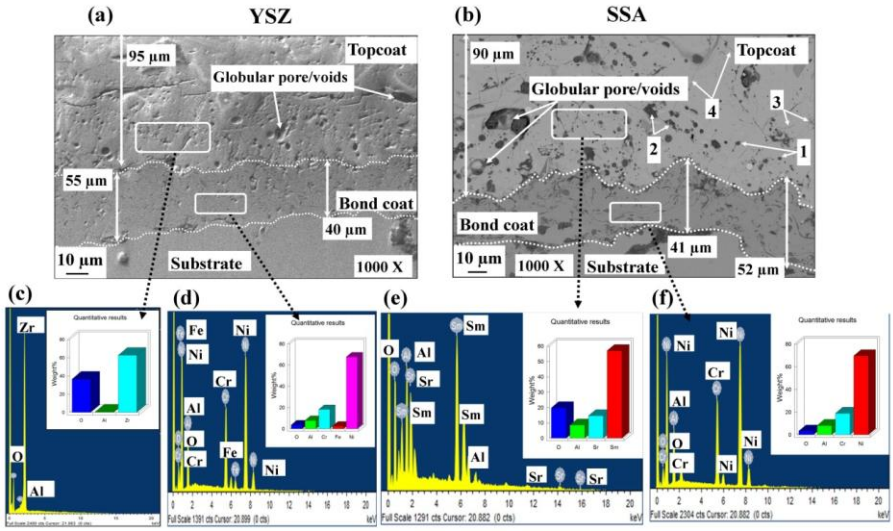

Fig. 4.7: Cross-sectional SEM images of the (a) as-deposited YSZ TBC; (b) as deposited SSA TBC; (c) EDS spectra of YSZ; (d) NiCrAlY bond coat in YSZ TBCs; (e) EDS spectra of SSA; and (d) NiCrAlY bond coat in SSA TBCs.

To compare YSZ and the SSA top coats, the second one has exhibited much-limited cracks, pores and also showed a good mechanical interlocking at the bond coat/top coat interface.

EDS analysis was carried out at the selected areas of both YSZ and SSA TBCs for analyzing the compositional variations at top and bond coat regions after deposition. The selected regions from Fig. 4.7 (a) predominantly contain Zr and O [Fig. 4.7 (c)]. The selected regions from bond coat majorly consist of Ni, Cr, Al and O [Fig. 4.7 (d and f)]. Similarly, the SSA TBC has shown the presence of Sm, Sr, Al, and O [Fig. 4.7 (e)]. The oxygen content in the NiCrAlY bond coat of YSZ and SSA TBCs was found to be about 11.07 and 9.75 at.%, respectively. Based on these results, it is confirmed that no major difference in compositional variations of NiCrAlY bond coat between YSZ and SSA TBCs due to the growth of protective TGO scale at the bond coat/top coat interface is negligible in the as-deposited coating.

4.3 Cross sectional analysis of TGOs formed by pre-oxidation treatment

Cross-sectional SEM images of the SSA TGOs after pre-oxidation treatment are represented in Fig. 4.8 (a-c). The continuous TGO layer was seen at the interface between bond coat/top coat for 10, 20 and 30 h pre-oxidized samples in Fig. 4.8 (a), (b) and (c), respectively. It showed that the microstructures divided into three segments, namely, TBC layer from the top coat, TGOs formed due to pre-oxidation treatments and followed by the bond coat of substrate. These microstructures clearly revealed that the presence of defects such as cracks and porosities in the TBC layer due to the formation of TGO and thermal stresses after pre-oxidation treatment at 1050 ^{o}C (Kulkarni et al. 2003).

The role of TGO is most important factor for the understanding of oxidation characteristics (Zhao et al. 2014 and Dong et al. 2014). TGO has been formed as an intermediate layer between the top coat and bond coat, however; it seems TGO itself divided into two interfaces (top coat/TGO and TGO/bond coat) which depend on the topcoat and bond coat materials [Figs. 4.8 (a-c)].

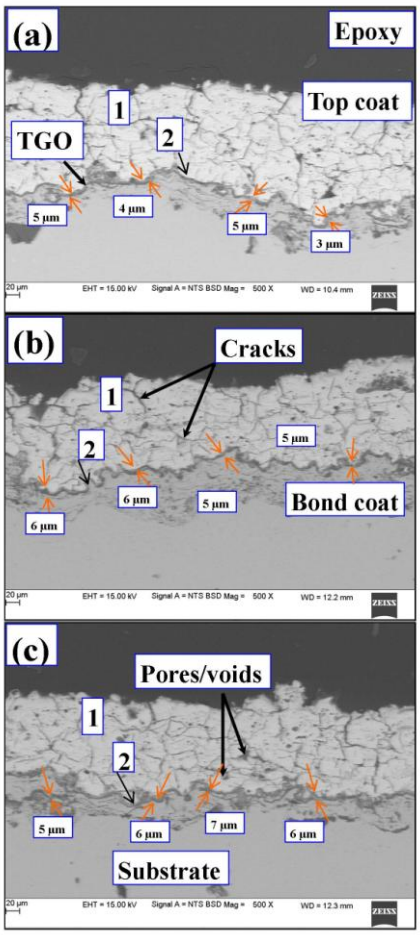

Fig. 4.8: Cross-sectional SEM microstructures of SSA TBCs with the TGOs after pre-oxidation treatment at 1050 ºC for (a) 10 h; (b) 20 h; and (c) 30 h in argon atmosphere.

The EDS analysis of top coat and TGO was taken from SEM images [shown in Figs. 4.8 (a-c)] after pre-oxidation at 1050 ºC for 10, 20 and 30 h. The presence of Sm, Sr, Al, and O were found at region 1 (in the ceramic top coat) and the presence of predominantly Al and O at region 2 (in the TGO layer).

The chemical composition of TGO is varied by varying pre-oxidation time shown in Table 4.4. The atomic percentage of Ni is significantly varied in the TGO region as 7.05, 1.17 and 1.30 for the treatment of 10, 20 and 30 h, respectively. It is indicating that an increasing pre-oxidation duration reduces the diffusion of Ni from bond coat to TGO region by approximately 80% due to increasing TGO growth at 1050 ºC. Similarly, the diffusion of Cr is also reduced by 76% (2.27% to 0.53%) from

10 to 30 h of pre-oxidation treatment. These observations have revealed that the amount of Ni and Cr, in the TGO region is relatively lesser for 20 and 30 h pre-treated samples. It is representing that the purity of the TGO of samples which is treated at 20 and 30 h is better than that of 10 h. It has revealed that the purity of obtained Al_2O_3 in TGO is found to be highest at 20 h of pre-oxidation with the lowest amount of NiO and the absence of Cr_2O_3.

Table 4.4: Cross-sectional EDS analysis of SSA TBCs after pre-oxidation at 1050 ºC (at.%).

Fig. 4.8	Regions	Type of layer	Sm	Sr	Al	O	Ni	Cr
(a)	1	Ceramic top coat	13.37	4.69	12.47	69.47	0.00	0.00
	2	TGO	-	-	31.75	58.93	7.05	2.27
(b)	1	Ceramic top coat	10.83	5.88	13.03	70.26	0.00	0.00
	2	TGO	1.89	0.67	31.39	64.90	1.17	0.00
(c)	1	Ceramic top coat	10.82	5.91	12.88	70.40	0.00	0.00
	2	TGO	1.90	1.45	31.97	62.85	1.30	0.53

Similar results were obtained by Chen et al. (2008), that a small amount of Ni, and Cr seen at the interface of TGO and top coat after pre-oxidation treatment at 1080 ºC in low-pressure oxidation atmosphere (Moskal et al. 2012). The present study shows the development of alumina-rich SSA TGO layer with negligible non-protective oxides of Ni and Cr, in order to study the role of pure α-Al_2O_3 TGO on the oxidation characteristics. The calculated TGO thicknesses of SSA were found to be about 4±1, 5±1 and 6±2 µm for 10, 20 and 30 h of pre-oxidation treatment respectively. The increasing growth of TGO layers observed with an increasing pre-oxidation time which is more consistent with the previous investigations (Dong et al. 2014 and Yuan et al. 2008). The microstructural and TGO thicknesses of YSZ analysis was carried out by Dong et al. 2014 and found that approximately 1.3±0.3 µm, 2.7±0.2 µm, and 3.9±0.3 µm at 1080 ºC for 4 h, 20 h and 50 h of pre-oxidation treatment, respectively which is quite lower than newly developed SSA TGOs. It was well proved that a formation of thicker alumina rich TGO during pre-oxidation

treatment which can act as a diffusion barrier at extended thermal exposure in the presence of air (Li et al. 2010).

4.4 Nano-hardness and Young's modulus of SSA TGOs after pre-oxidation

Fig. 4.9 (a) and (b) shows typical depth-time and load-depth curves, respectively obtained by nano-indentation technique on the surface of SSA TBCs after pre-oxidation treatment at 1050 ºC. The mechanical and other properties (percentage porosity and elastic recovery) of coating were reported in Table 4.5. The porosity of coatings before and after pre-oxidation was calculated based on the theoretical relation between Young's modulus of porous and solid SSA ceramic (Kovacik et al. 1999 and Guo et al. 2004). The load and depth variation of 10, 20, and 30 h pre-oxidized SSA TBCs were continuously measured on the surface during loading and unloading condition. The depth of the curve increases with an increasing pre-oxidation time for SSA TBCs [Fig. 4.9 (b)].

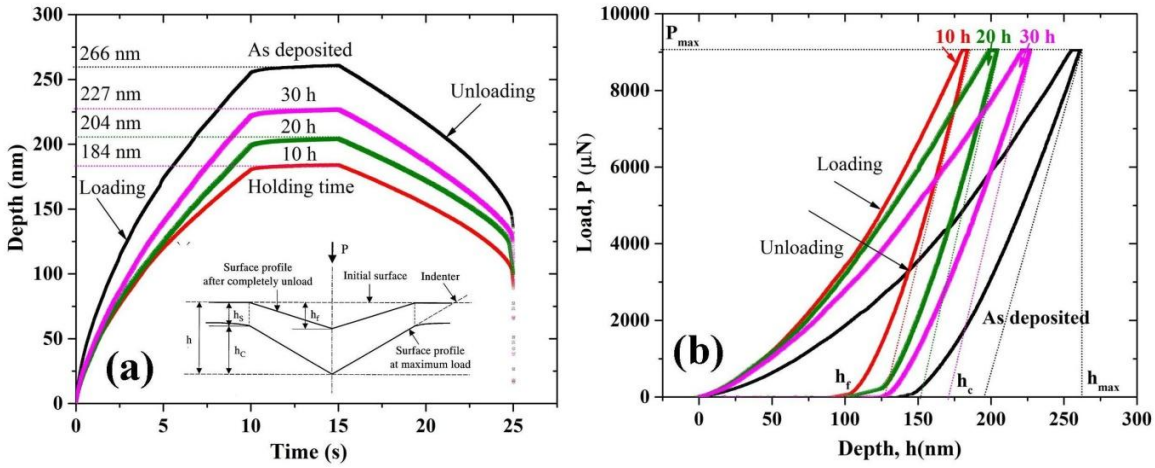

Fig. 4.9: Typical (a) depth-time; and (b) load-depth curves of SSA TBCs before and after exposure to pre-oxidation treatment at 1050 ºC with different time.

The maximum penetration depth was observed for 30 h (227 nm) and followed by 20 h (204 nm) and 10 h (184 nm). The Young's modulus, hardness, and stiffness of SSA TBCs tend to decrease with an increasing pre-oxidation time from 10 to 30 h at 1050 ºC. The calculated porosity values were found to be about 12, 33, and 57% for 10, 20 and 30 h, respectively. The decrease in young's modulus and hardness with an increasing pre-oxidation time can be explained by the fact that an increasing number

of defects (porosity and cracks) make SSA ceramic layer more porous which increases accessibility of oxygen and TGO growth during pre-oxidation treatment at 1050 ºC. These findings of the present work also showed that 30 h pre-oxidized SSA specimen exhibits 50% elastic recovery than 10 (45%) and 20 h (48%). The slightly higher elastic recovery at 30 h is due to the presence of defects in the form of pores and cracks, which can distribute the strain energy during loading and unloading condition. The mechanical properties and percentage elastic recovery of as deposited SSA TBCs (without pre-oxidation) showed considerably lower than pre-oxidized samples could be due to the presence of higher porosity (65%).

According to the literature, the mechanical properties of air plasma sprayed TBCs may change with an increasing thermal cycle due to the effect of sintering and porous microstructure of top coat (Guo et al. 2004). It is also widely accepted that the presence of microstructural defects such as porosity and interconnected cracks makes the thermal barrier coating more strain tolerable at higher temperature (Guo et al. 2006). So, it is quite interesting to examine the oxidation kinetics of SSA TBCs depends on the microstructure of top ceramic layer and growth of TGO thickness at the different pre-oxidation time.

Table 4.5: Mechanical properties of SSA TBCs after pre-oxidation at 1050 ºC.

Condition	Time (h)	h_c (nm)	h_f (nm)	h_{max} (nm)	Young's modulus, E (GPa)	Hardness, H (GPa)	Stiffness, S (μN/nm)	Percentage elastic recovery	Percentage porosity in top coat
With pre-oxidation	10	129	100	184	220	12	219	45	12
	20	137	105	204	170	10	180	48	33
	30	157	113	227	107	8	128	50	57
Without pre-oxidation	0	204	140	267	73	5	109	47	65

4.5 Oxidation kinetics of SSA and YSZ TBCs in air

Oxidation studies were conducted at 1100 ºC for 15 h on SSA and YSZ TBCs to evaluate the role of TGOs which is developed at 1050 ºC for 10, 20 and 30 h pre-oxidation treatment. Figs. 4.10 (a and b) shows the weight gain plots of SSA and YSZ TBCs as a function of time (5, 10 and 15 h) at 1100 ºC in the presence of air. The Figs. 4.10 (a) and (c) clearly show that the oxidation kinetics of both SSA and YSZ TBCs behaves as a parabolic law. It was noticed that the highest weight gain attained at 10 h as compared to 20 and 30 h of pre-oxidation treatment at 1050 ºC for SSA TBCs due to the low growth of TGO (4±1 µm) thickness. The lowest weight gain was found at 20 h of pre-oxidation treatment because of high enriched alumina (98.18 %) with the presence of a lowest amount of Ni (oxides; <2%), highest TGO growth (5±1 µm) and moderate defects (porosity and micro-cracks) as compared to 10 and 30 h (shown in Fig. 4.10).

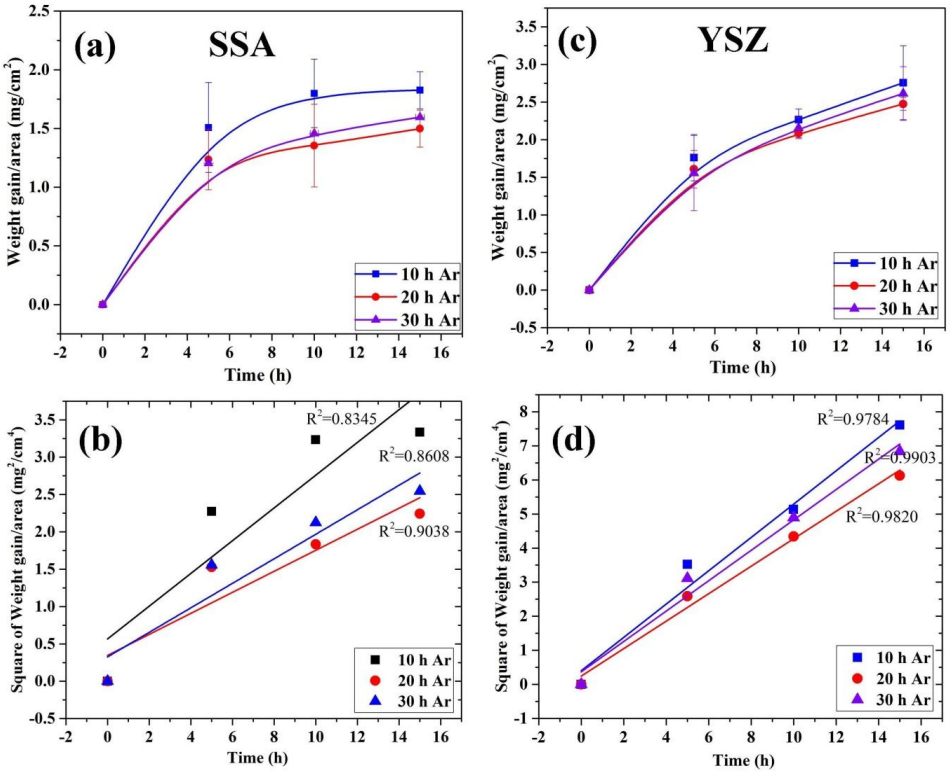

Fig. 4.10: Weight-gain plots and $(\text{Weight gain/area})^2$ vs. time plots of (a and b) SSA; and (c and d) YSZ after oxidation at 1100 ºC for 15 h in air.

So based on these results, it can be concluded that TGO growth and compositional purity play an important role than top coat microstructure during the oxidation process at 1100 ºC. A similar weight gain trend was observed in the case of YSZ TBCs in Fig. 4.10 (b) and the variations in weight gain from 10 to 20 and 20 to 30 h of pre-oxidation treatment are about 10% and 5%, respectively. So, it is clear that the observed weight gain of YSZ TBCs is higher than the SSA TBCs (65%) after oxidation at 1100 ºC [Figs. 4.10 (a) and (c)].

To examine parabolic rate constant at different pre-oxidation treatment conditions using a plot of the square root of weight gain per unit surface area with time for SSA and YSZ are shown in Figs. 4.10 (b and d). The governed relationship between weight gains per unit surface area with time is shown in Eq. (4.1) from the best fitting of plots for SSA [Fig. 4.10 (b)] and YSZ [Fig. 4.10 (d)] at an exposure time of 5, 10 and 15 h.

$$\frac{\Delta W}{A} = (k_p.t)^{1/2} + C_o \qquad (4.1)$$

Where, **(ΔW/A)** - Weight gain per unit surface area (mg/cm^2) at given time **t** (s), $\mathbf{k_p}$ is parabolic rate constant and $\mathbf{C_o}$ is a constant. The parabolic rate constants of both SSA and YSZ TBCs are summarized in Table 4.6.

Table 4.6: Parabolic rate constants of pre-oxidized SSA and YSZ specimens after oxidation study at 1100 ºC for 15 h in air.

Time (h)	Type of ceramic top coat	Parabolic rate constant k_p (mg^2.cm^{-4}.s^{-1}) ×10^{-5}
10	SSA	6.08
20		3.90
30		4.55
10	YSZ	13.57
20		11.19
30		12.38

The rate constant $\mathbf{k_p}$ is very sensitive to diffusion of metal cations such as Ni^{2+}, Cr^{3+} and Al^{3+} (Perez 2004).

From Table 4.6, it is noticed that the rate constant k_p decreased from 10 to 20 h followed by an increment at 30 h of pre-oxidation treatment for SSA TBCs. A slightly higher rate constant was observed at 30 h of pre-oxidation treatment as compared to 20 h is due to the presence of high porous structure (57%), indicating a possibility of either the presence of defects which led the high diffusivity of oxygen in the ceramic top coat and TGO layer at 1100 ºC. From Fig. 4.10 and Table 4.6, it is also evident that the rate of oxidation of air plasma sprayed SSA TBCs system is approximately 65% lower than that of YSZ TBCs. Hence, the newly developed SSA based ceramic coating can slow down the oxidation behavior of the metallic bond coat and impart the oxidation resistance of TBCs systems at 1100 ºC in air.

4.6 Post oxidation analysis

To understand the chemical stability of TGO at the bond coat/top coat interface and the mechanisms of the oxidation process, a detailed analysis of cross-sectional and the top surface of SSA and YSZ TBCs were undertaken using scanning electron microscopy, energy dispersive X-ray spectroscopy, and X-ray diffractometry techniques.

4.6.1 Phase analysis of SSA and YSZ TBCs after oxidation:

To understand the presence of phases on the surface of the top coat of SSA and YSZ TBCs, XRD was conducted for the highest time of 30 h of pre-oxidized samples which is oxidized for 15 h at 1100 ºC. XRD patterns of SSA and YSZ TBCs after exposure to 1100 ºC for 15 h have shown in Figs. 4.11 (a) and 4.11 (b), respectively. The XRD pattern of oxidized SSA top coat [from Fig. 4.11 (a)] clearly revealed that the absence of new products formation or decomposition of phases after the oxidation test at 15 h, however; it has also shown the changes of intensity of the major representative peaks at 32.61, 33.74, 43.64, 48.70 and 59.98º values due to possibility of preferred crystal growth in SSA ceramic (Cao et al. 2001). The

diffraction profile of YSZ TBCs after oxidation at 1100 ºC for 15 h is shown in Fig. 4.11 (b). All the peaks were indexed and referred to be t-ZrO_2 crystal structure (JCPDS # 79-1769). A small intensity peak was noticed at 27.6º, representing as an m-ZrO_2 (JCPDS # 89-9066) phase after enlarging the peaks between 27 to 28º (inset image of Fig. 4.11). The quantities of transformed zirconia from tetragonal to monoclinic phase were calculated using XRD peak integral intensity ratios of t-ZrO_2 and m-ZrO_2 and obtained about 9%.

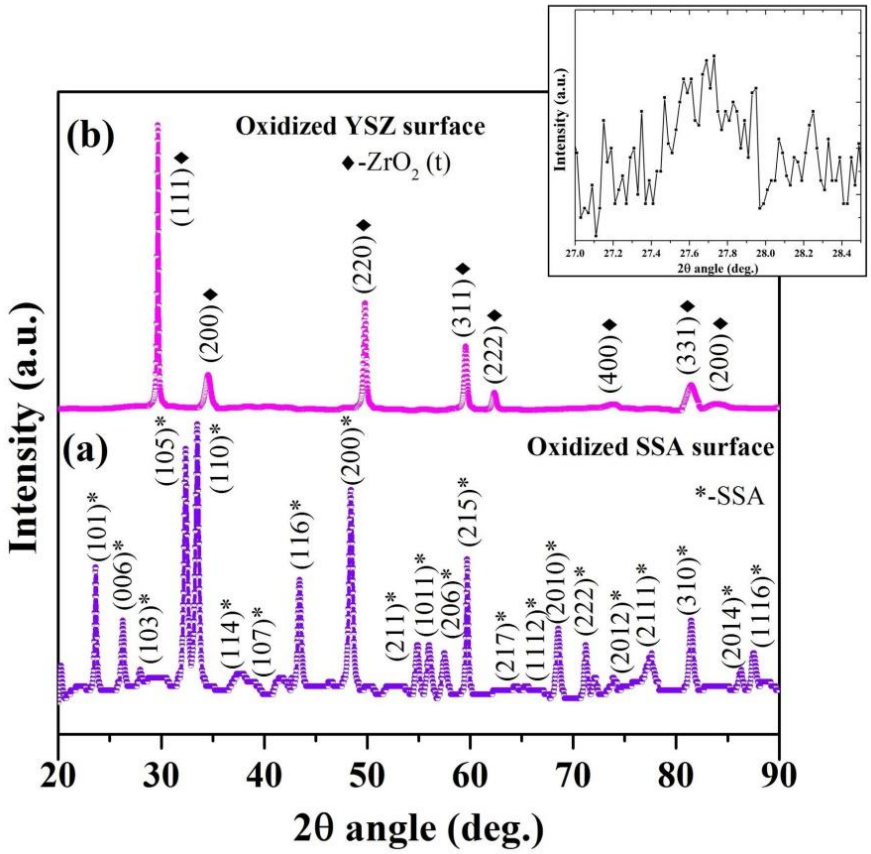

Fig. 4.11: X-ray diffraction patterns of the top surface of oxidized (a) SSA TBCs (30 h pre-oxidized); and (b) YSZ TBCs (30 h pre-oxidized) after exposure to 1100 ºC for 15 h in air.

Many researchers have reported that the presence of m'-ZrO_2 is quite detrimental for the stability of thermal barrier coating due to the volume expansion which caused spallation and failure of coating (Evans et al. 2001 and Song et al.

2011). But in the case of SSA coating, the solid solution of Sm_2O_3 and SrO in Al_2O_3 with a body-centered tetragonal structure was still maintained, as indicated in XRD pattern [Fig. 4.11 (a)] even after exposure to 1100 ºC for 15 h of oxidation treatment in air. These features have made SSA more suitable and prominent over conventional YSZ ceramic for high-temperature thermal barrier coating applications.

4.6.2 Microstructural investigations of SSA and YSZ TBCs:

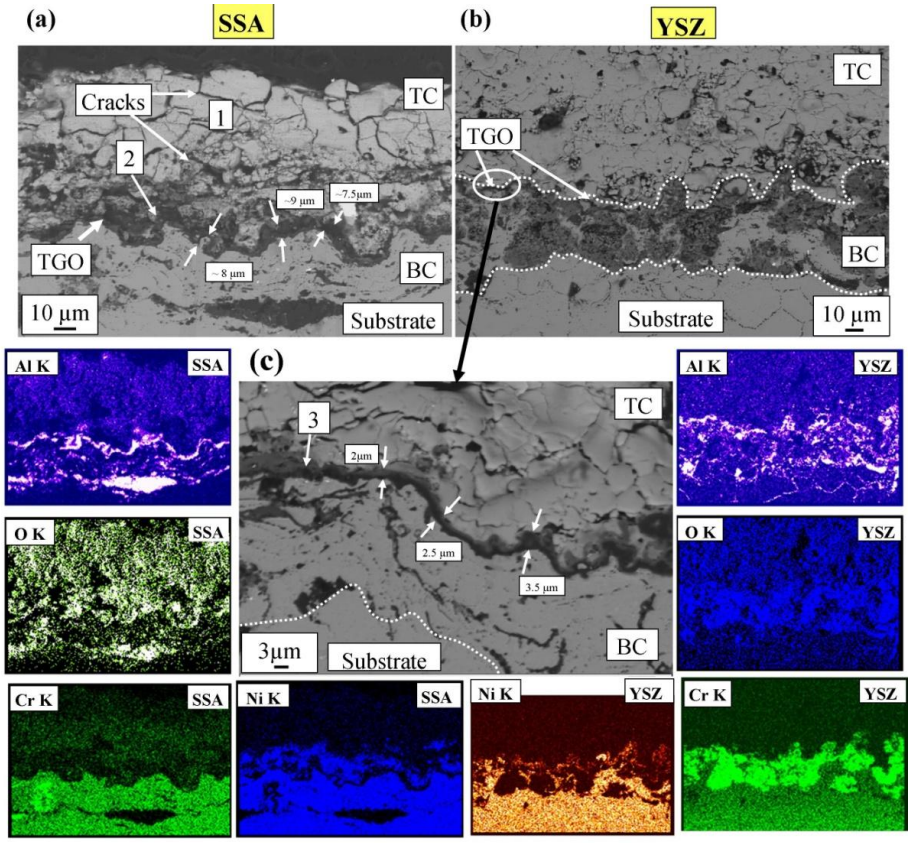

Fig. 4.12: Cross-sectional SEM micrographs of the SSA and TBCs after oxidation at 1100 ºC for 15 h: (a) SSA 10 h pre-oxidized; and (b and c) lower and higher magnification images of YSZ 10 h pre-oxidized. Note: EDS elemental mapping of Al, O, Ni and Cr for both SSA and YSZ TBCs are also shown here.

The cross-sectional SEM images of SSA and YSZ TBCs were taken to analyze the chemical stability of TGO at the interface of ceramic top coat/TGO after oxidation in air at 1100 ºC (10 h pre-oxidized condition) for 15 h is shown in Figs. 4.12 (a-c). Fig. 4.12 (a) shows the horizontal and longitudinal cracks along with

globular pores near the top coat and at the mixed interface of TGO/top coat. EDS analysis was done at two regions, namely, 1 (top coat side) and 2 (TGO mixed side) to know the presence of elements and their oxides. The observed elemental values are tabulated in Table 4.7. The major metallic elements Sm, Sr, Al, and O were seen at region 1 [Fig. 4.12 (a)]. However; at region 2, which is close to the TGO interface consists of extra available Cr and Ni elements as compared to region 1 (Sm, Sr, Al and its oxides) due to high diffusivity of Cr and Ni metals to form their oxides [Fig. 4.12 (a)].

Similarly, the cross-sectional microstructure of YSZ TBCs (10 h pre-oxidized) after exposure to 1100 ºC for 15 h is shown in Fig. 4.12 (b). A very thin and discontinuous TGO layer was observed as compared to SSA TBCs. The higher magnification image of TGO layer in Fig. 4.12 (b) is shown in Fig. 4.12 (c). The average TGO thickness of YSZ TBCs is about 2.5±1 µm. EDS analysis was conducted at the region 3 in Fig. 4.12 (c) is mainly composed of Al and O. The EDS elemental map scanning analysis of both SSA and YSZ TBCs are also shown in Fig. 4.12. The map clearly indicates that larger chromium and oxygen concentrations in the bond coat region of YSZ TBCs than they are present in the case of SSA TBCs. Hence, it can be inferred that the formation of spinel oxides inside the bond coat is responsible for higher weight gain in the YSZ TBCs. The measured TGO thicknesses of both 10 h pre-oxidized SSA and YSZ after oxidation treatment at 1100 ºC are 9±2 µm and 2.5±1 µm, respectively. The presence of a thin and discontinuous TGO layer in the YSZ TBCs caused to diffuse more atmospheric oxygen into metallic bond coat layer and it resulted in higher oxidation at 1100 ºC (Matsumoto et al. 2006).

The cross-sectional micrographs of the oxidized SSA and YSZ TBCs (20 and 30 h pre-oxidized samples) were examined and the results are shown in Fig. 4.13. From Fig. 4.13 (a), it can be seen that the severe coating degradations, which is observed at the top coat/TGO interface. A detailed EDS analysis were carried out to find out the chemical composition of both top coat and TGO region, data are tabulated in Table 4.7. The region 1 (Fig 4.13 a-b and c-d) in both 20 and 30 h pre-oxidized

SSA and YSZ contains Sm, Sr, Al, and O and Zr and O, respectively (Table 4.7). Similarly, at region 2 (Fig 4.13 a-b and c-d), the 20 and 30 h pre-oxidized SSA sample contains Al and O and YSZ consists of Ni, Cr, Al, and O. The TGO thicknesses of 20 h pre-oxidized SSA [Fig. 4.13 (a)] and YSZ TBCs [Fig. 4.13 (b)] showed 6±2 µm and 2±0.5 µm, respectively.

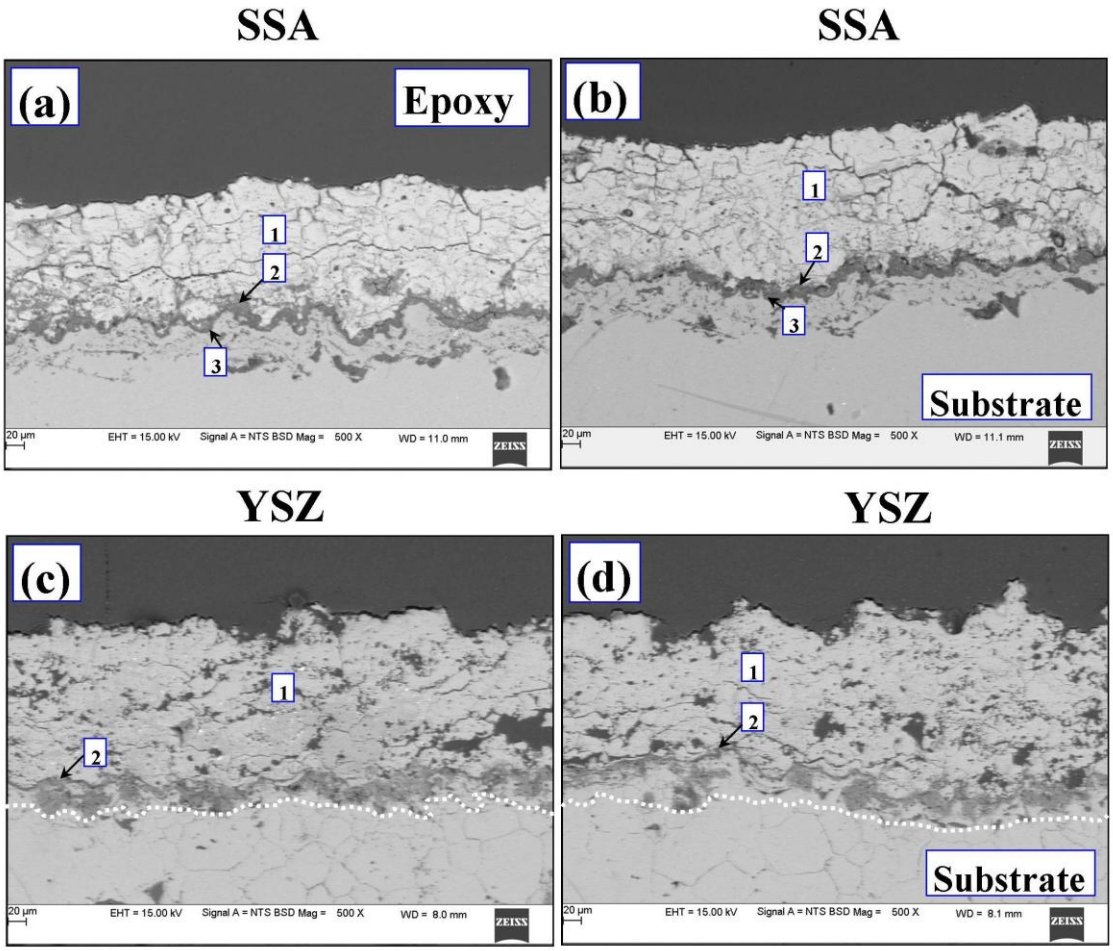

Fig. 4.13: Cross-sectional SEM micrographs of the SSA coatings after oxidation at 1100 ºC for 15 h: (a) 20 h pre-oxidized; and (b) 30 h pre-oxidized and the YSZ coatings after oxidation at 1100 ºC for 15 h: (c) 20 h; and (d) 30 h pre-oxidized samples.

Table 4.7: Chemical compositions of pre-oxidized SSA (10 and 20) samples after oxidation at 1100 ºC for 15 h (at.%).

Fig.#	Condition	Region	Sm	Sr	Al	O	Ni	Cr
Fig.4.12 (a)	SSA 10 h	1 (top coat)	16.55	7.48	14.53	61.44	0.00	0.00
		2 (TGO)	0.00	0.00	34.20	58.32	4.57	5.91
Fig.4.13 (a)	SSA 20 h	1 (top coat)	18.09	7.95	15.01	58.95	0.00	0.00
		2 (TGO)	0.00	0.00	36.73	54.36	6.34	2.58
Fig.4.13 (b)	SSA 30 h	1 (top coat)	18.61	7.46	16.21	57.72	0.00	0.00
		2 (TGO)	0.00	0.00	28.04	57.59	9.92	4.01

After oxidation at 1100 ºC, in the case of SSA TBCs, the highest TGO growth was found at 10 h as compared to 20 h pre-oxidized SSA samples due to the presence of less pure Al_2O_3 TGO (86.32%). In other words, lowest TGO growth was found at 20 h of pre-oxidized samples than 10 due to the TGO of pure Al_2O_3 (98.18%) which contributed to lower the oxidation of metallic NiCrAlY bond coat. The presence of low thick and discontinuous YSZ TGOs caused more bond coat oxidation than SSA TGO s at 1100 ºC which is well matched with the results of oxidation kinetics.

4.6.3 Mechanisms of destabilization of SSA TBCs at the topcoat/TGO interface:

In order to identify the phase composition at the top coat/TGO interface, the XRD analysis was done on the TGO surface of 10 and 20 h pre-oxidized samples after delamination of top coat which is shown in Figs. 4.14 (a and b), respectively. Peaks of $SmAlO_3$ (JCPDS # 29-0083) and mixed oxides such as NiO, Cr_2O_3, and $NiCr_2O_4$ are also found in the spectrum (10 h pre-oxidation) [Fig. 4.14 (a)].

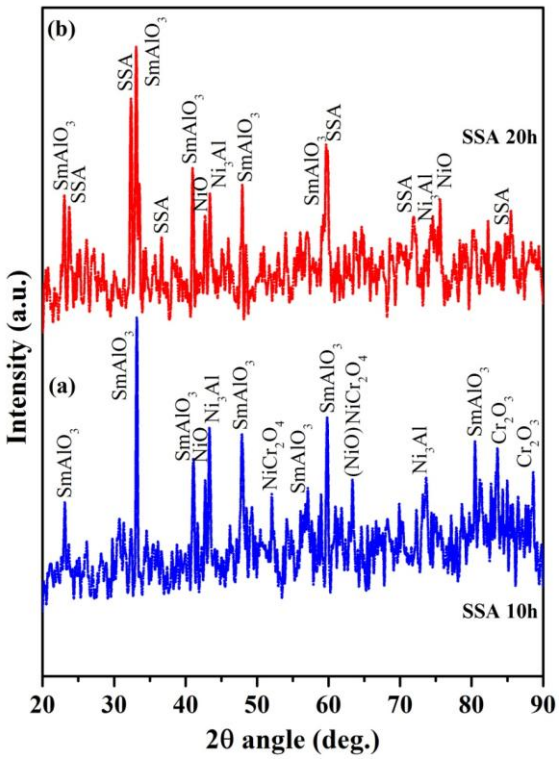

Fig. 4.14: X-ray diffraction analysis of the TGO surface of SSA TBCs after exposure to 1100 ºC for 15 h: (a) 10 h; and (b) 20 h pre-oxidized samples.

In the case of 20 h pre-oxidation treatment, the phases such as $SmAlO_3$, mixed oxides, and SSA top coat materials were observed [Fig. 4.14 (b)]. The percentage of NiO at the interface of samples treated at 10 and 20 h of pre-oxidation treatment were found to be about 42% and 30%, respectively. The formation of mixed oxides at the interface plays an important role in determining the lifetime of TBCs. In this study, the amount of mixed oxides (NiO, Cr_2O_3 and $NiCr_2O_4$) formation at the interface for 20 h of pre-oxidized sample is the lowest than 10 h, which means that quality of TGO at 20 h of pre-oxidized sample even after oxidation at 1100 ºC for 15 h is significantly superior to 10 h treated samples.

Several researchers have also found that rare earth oxides such as Sm_2O_3 and Gd_2O_3 react with Al_2O_3 when coatings exposed to high temperatures (Leckie et al. 2005). So, at the top coat/TGO interface, SSA phase would be first dissociated into Sm_2O_3 and $SrAl_2O_4$ and then reacted with the Al_2O_3 containing TGO to form samarium aluminate ($SmAlO_3$). According to the previous research on phase

compositions of SSA at 1100 ºC and the XRD results of present work, the phase degradations of SSA top coat/TGO could be expressed in the following manner (Zvereva et al. 2003):

$$Sm_2SrAl_2O_7 \rightarrow Sm_2O_3 + SrAl_2O_4 \quad (4.2)$$

$$Sm_2O_3 + Al_2O_3 \rightarrow 2SmAlO_3 \quad (4.3)$$

Comparatively, the newly developed SSA TBCs exhibits better oxidation resistance at 1100 ºC than conventional YSZ TBCs and this may be explained by the growth of TGO at the interface of bond coat/top coat. Though the 10 h pre-oxidized samples showed good mechanical properties and lower porosity than 20 and 30 h, but lower TGO growth and less pure TGO which are contributed to reducing oxidation resistance at 1100 ºC in air. Hence, the oxidation resistance of SSA TBCs is more sensitive to compositional changes at the interface than top coat microstructure under Ar and air atmosphere at 1050 and 1100 ºC, respectively. The TGO with lower thickness is easier to permeate oxygen ions, which results in higher weight gain of the metallic bond coat in the YSZ TBCs. The existence of higher TGO thickness can effectively reduce oxygen permeation; as a result, the oxidation resistance of SSA TBCs is better.

Summary of oxidation study

- The newly developed SSA TBCs exhibits 65% higher oxidation resistance than YSZ TBCs mainly due to the formation of enriched alumina TGO at the interface.
- The presence of discontinuous TGO and mixed oxides (NiO and $NiCr_2O_4$) at the interface makes YSZ TBCs less oxidation resistance than SSA TBCs at higher temperature.

CHAPTER 5

5 ELECTROCHEMICAL IMPEDANCE BEHAVIOR OF OXIDIZED SSA TBCs

It is very difficult to examine the TBCs degradations non-destructively which is most important for predicting the failures and life time assessment of turbine components. Among several non-destructive techniques developed for life assessment of TBCs impedance spectroscopy has been widely used to evaluate the TGO compositional changes and the effect of porosity on the ceramic top layer at higher temperature. In the present work, this technique was used to study the role of top coat and TGO microstructure of SSA TBCs after exposure oxidation at 1100 ˚C.

5.1 Microstructure and electrical property relation of pre-oxidized SSA TBCs

5.1.1 Electrochemical impedance spectra of pre-oxidized SSA TBCs

EIS study is usually represented in Nyquist and Bode plots, in which Nyquist plot consists of a real part and imaginary part of impedances. Bode plot, represents modulus of impedance and phase angle with respect to frequency. In order to find out the electrical property changes of a different layer, it is necessary to design a suitable equivalent circuit model to fit the generated experimental spectra. Since, the electrode surface is not uniform; an ideal capacitor cannot be used to describe the capacitive behavior of SSA TBCs. In such case, constant phase element (CPE) can be used to describe the non-ideal capacitance behavior (MacDonald 1987, Fletcher et al. 1995 and Amaral et al. 1999).

For non-ideal capacitors, the capacitance (C) can be calculated by (Feig et al. 2002 and Wang et al. 2001)

$$C = R^{(1-n)/n} A^{1/n} \qquad (5.1)$$

Where **R** is the resistance and **A** is the parameter of CPE. The CPE behaves like a pure resistor and capacitor, when **n** lies between 0 and 1, respectively.

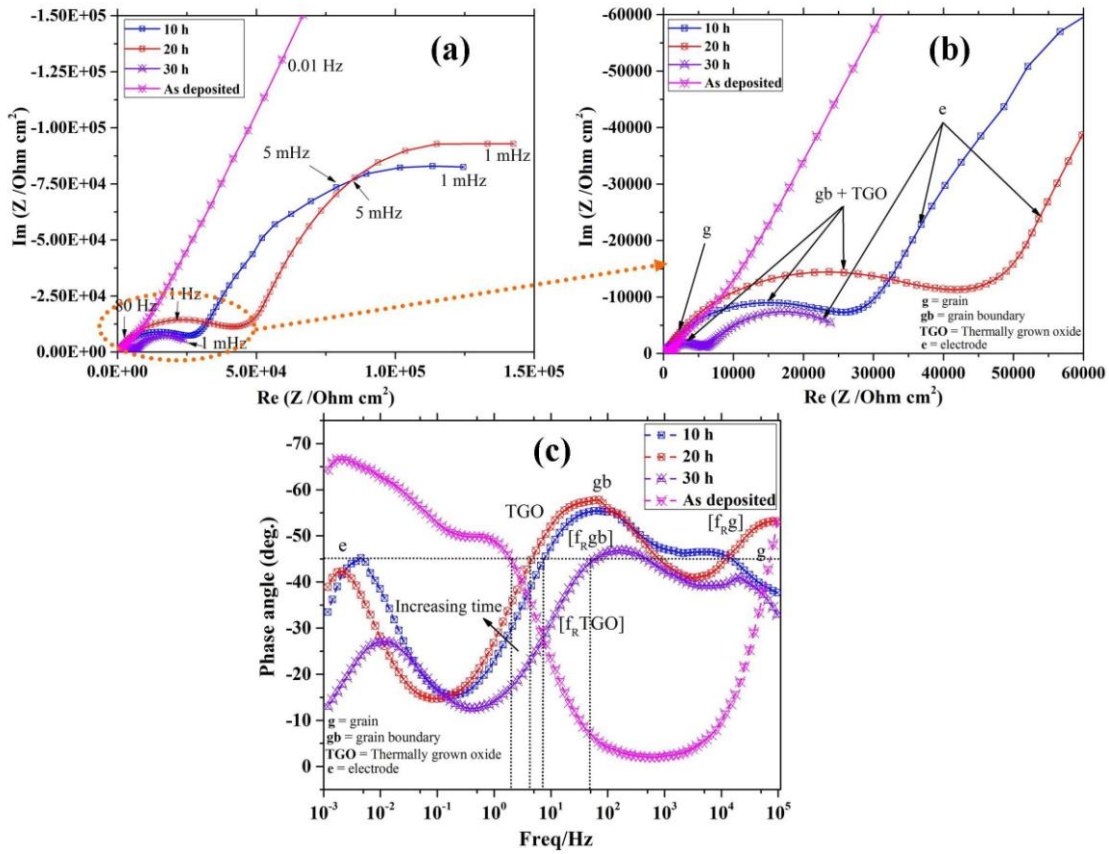

Fig. 5.1: (a) Nyquist impedance, (b) Magnified high frequency Nyquist impedance plot and (c) Bode phase angle plot as a function of frequency of pre-oxidized SSA specimens after exposure to 1050 ºC for different exposure times.

Nyquist and Bode plots of SSA specimens subjected to different pre-oxidation treatment are represented in Fig. 5.1 (a and b) and (c and d), respectively. In Fig. 5.1 (a and b), each plot consists of two semicircles with different diameters, the first semicircle corresponds to grain, grain boundary of SSA top coat, TGO and second semicircle correspond to electrode effect due to TGO-bond coat interface charge transfer resistance. Figs. 5.1 (c and d) represents Bode plot which is classified as three different zones such as high frequency of 10^5-10^2 Hz, medium frequency of 10^0-10^2 Hz and low frequency of 10^{-1}-10^{-3} Hz corresponds to grain and the grain boundary of SSA TBCs, TGO layer and charge transfer response at the TGO-bond coat interface respectively. These phenomenons have been observed in many literatures on an

impedance spectroscopy study of the high-temperature oxidation of thermal barrier coatings (Song et al. 2005 and Jayaraj et al. 2004).

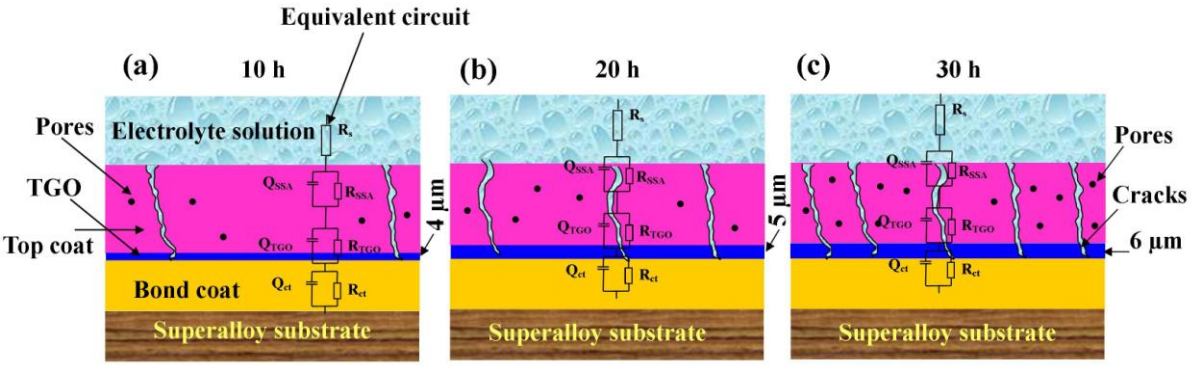

Fig. 5.2**:** Schematic illustrations of SSA TBCs components with AC equivalent circuit model. (a) 10; (b) 20; and (c) 30 h pre-oxidized at 1050 ºC in argon atmosphere.

A clearly two relaxation process is observed for as deposited SSA top coat due to the absence of TGO layer at the junction of top coat and bond coat. The as deposited SSA TBCs found to be higher impedance over pre-oxidized specimens due to the absence of interconnected cracks and pores [Fig. 5.1 (a)]. The magnified view of high frequency plot of Fig. 5.1 (a) is shown in Fig. 5.1 (b). The SSA TBCs pre-oxidized for 20 h at 1050 ºC showed the largest impedance than 10 and 30 h treated specimens. According to both Figs. 5.1 (c and d), the pre-oxidation treatment led appreciable changes in the frequency response of the SSA TBCs. In contrast to as-sprayed SSA TBCs, the pre-oxidized SSA TBCs showed good frequency distribution in the region from 10^5-10^1, 10^1 - 10^0 and 10^0 - 10^{-3} Hz.

The impedance plot was fitted based on a chosen model of 3 R/CPE in the series connection, which corresponds to the SSA top coat, TGO and electric charge transfer resistance as shown in Fig. 5.2. From Fig. 5.3 (a and b), it is evident that both fitted and measured impedance (Nyquist plot) results of as deposited and pre-oxidized SSA TBCs (1050 ºC for 30 h) are very well consistent. The obtained fitting error of impedance simulation was less than 10 %. However, two R/CPE model was used for fitting for as deposited SSA TBCs due to the absence of TGO layer [Fig. 5.3 (a)] (Huang et al. 2011).

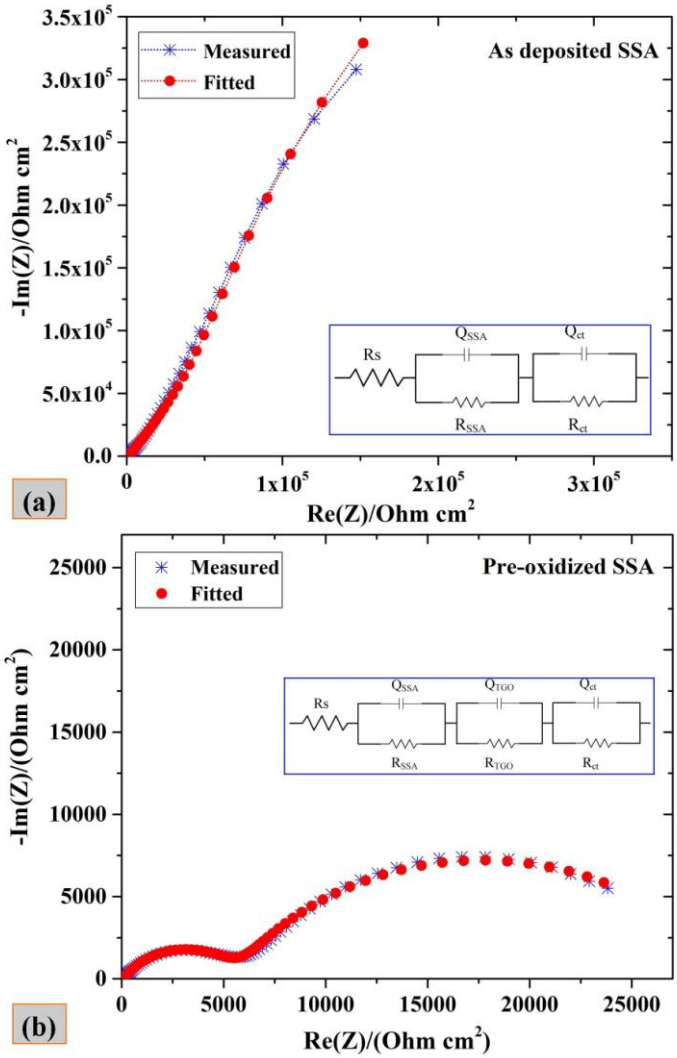

Fig. 5.3: Measured Nyquist plot, fitted results and the equivalent circuit model for SSA TBCs (a) before (as deposited); and (b) after exposure to pre-oxidation at 1050 ºC for 30 h. Note: Q_{SSA}-constant phase element (CPE) of SSA top coat; Q_{TGO}-CPE of TGO layer; Q_{ct}-CPE electric charge transfer between TGO layer and bond coat; R_s-solution resistance; R_{SSA}-resistance to current flow through the SSA top coat; R_{TGO}-resistance to current flow through the TGO layer; R_{ct}-charge transfer resistance at the interface between the TGO and bond coat.

5.1.2 Role of micro-structural defects in SSA top coat on EIS

The cross-sectional SEM microstructure of SSA top coat after exposure to 1050 ºC for different pre-oxidation duration is presented in Fig. 5 (a-c). It is clearly

revealed that microstructure consists of a ceramic top coat, TGO layer (black dark region) followed by the bond coat and substrate.

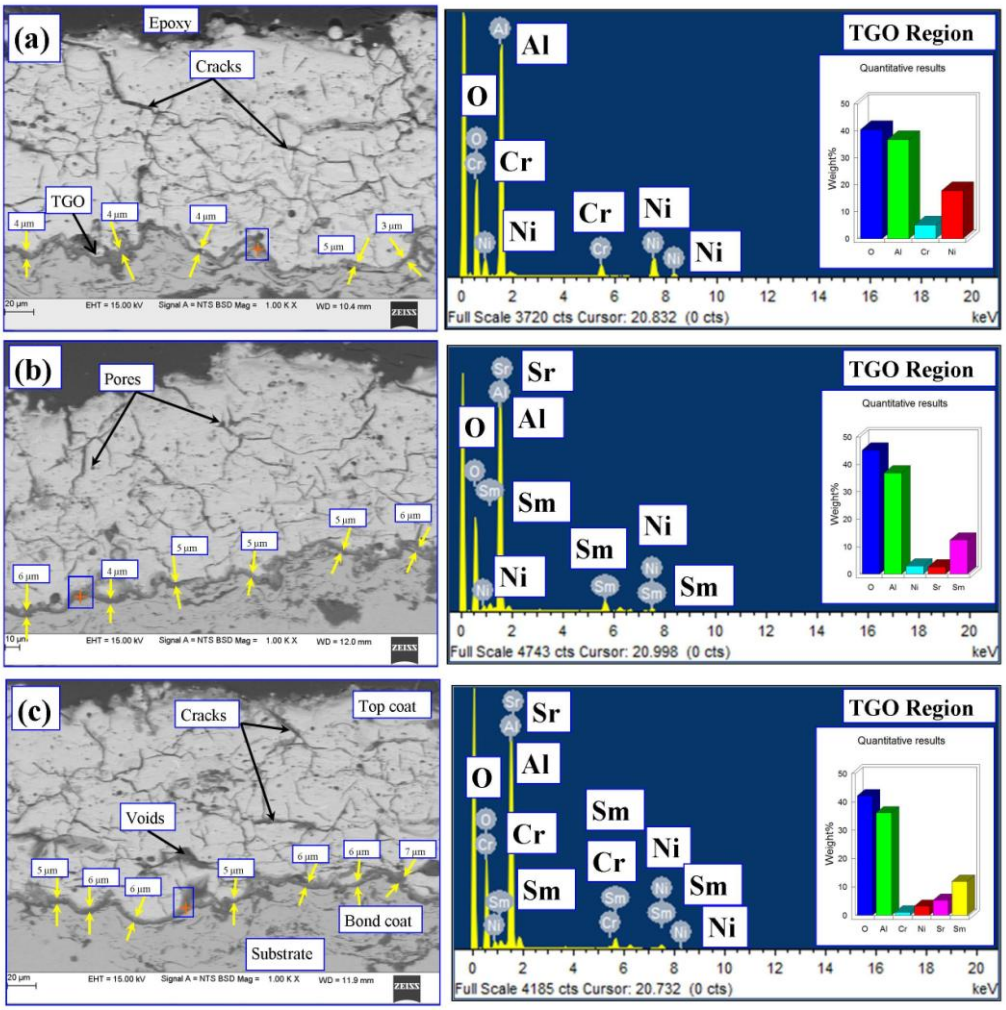

Fig. 5.4: Cross sectional SEM microstructure of pre-oxidized SSA TBCs and respective EDS analysis after exposure to (a) 10; (b) 20; and (c) 30 h at 1050 ºC in argon atmosphere.

Some cracks and porosities can be visibly seen in the microstructure of SSA top coat owing to the formation thermal stresses due to TGO growth during pre-oxidation treatment at high temperature (Yuan et al. 2008). TGO layer has formed due to the oxidation of metallic NiCrAlY bond coat and other top coat property changes at 1050 ºC. Cracks were exhibited at 10 h is found to be lower [Fig. 5.4 (a)] over the higher exposure time of 30 h [Fig. 5.4 (c)].

The cross sectional SEM images (processed by Image J software) of pre-oxidized SSA TBCs are shown in Fig. 5.5 (a-c). The porosity measurement shows the typical pore size distributions in the range of 0.1 - 4 µm [Fig. 5.5 (d-f)]. The fine pores less than 1 µm correspond to incomplete contact between splats and the micro-cracks. The large pores (size < 1 µm) arises by imperfect layer built-up by the molten droplet during the deposition process (Du et al. 2005). More fine pores and cracks could be seen in 30 h as compared to 10 and 20 h, it may be due to higher pre-oxidation duration. It was also observed that the number of cracks and pores increased and some small cracks and pore merge together to form larger cracks in the top coat after 30 h of exposure. The calculated defects in the form of pores and cracks have found to be 13, 29, and 45% respectively for 10, 20, and 30 h of pre-oxidation at 1050 ^{o}C.

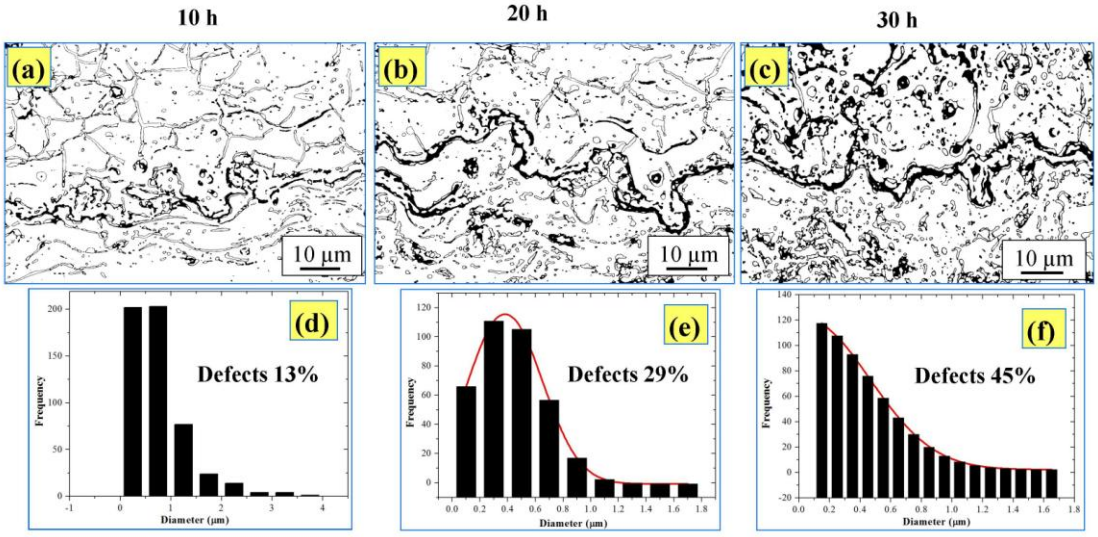

Fig. 5.5: Image J software processed higher magnification cross sectional SEM images of SSA coatings after exposure to pre-oxidation at 1050 ^{o}C for (a) 10; (b) 20; (c) 30 h and (d-f) porosity distributions of (a-c); respectively.

From Nyquist impedance plot [Fig. 5.1 (a and b)], it is found that the diameter of the first semicircle is gradually increased from 10 to 20 h and then decreased due to increasing percentage of defects in the top coat. The Bode plot [(Fig. 5.1 (c)] shows a shift of phase angle (towards low frequency) in the range 10^{1}-10^{0} Hz; it indicates that impedance increases with increasing pre-oxidation time from 10 to 20 h and a significant reduction at higher exposure time of 30 h.

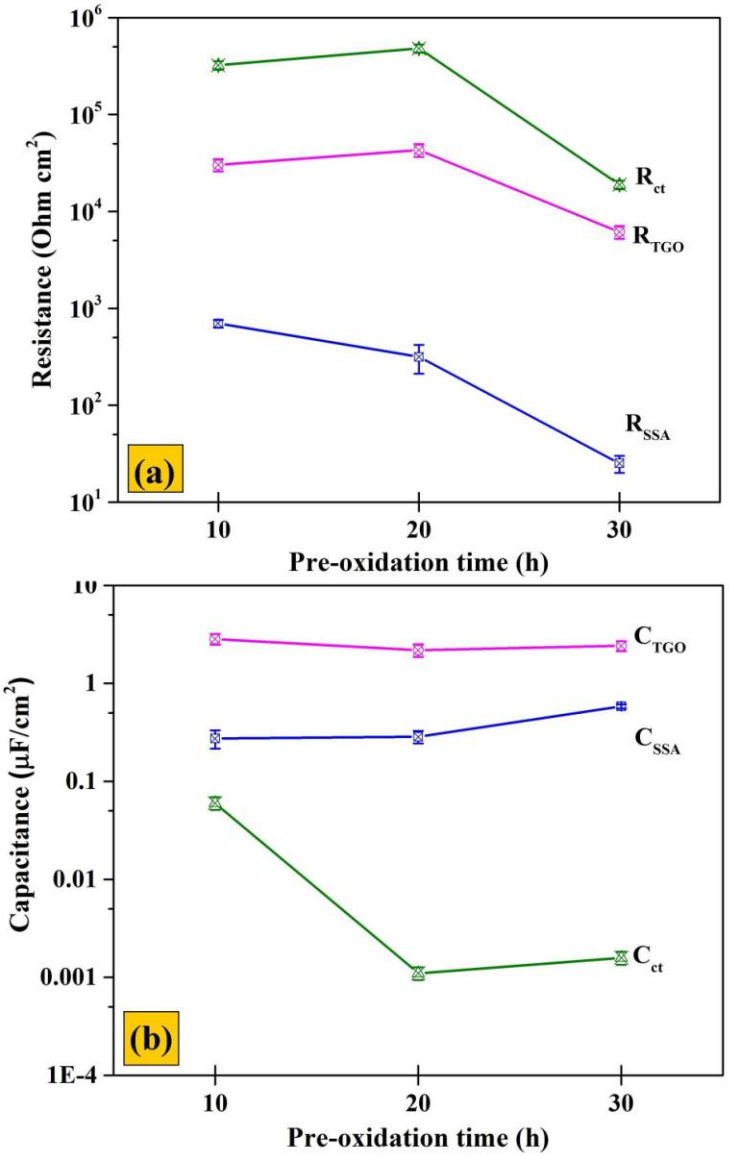

Fig. 5.6: Electrical properties of SSA top coat and TGO (a) resistance; and (b) capacitance as a function of pre-oxidation time after exposure to 1050 ºC in argon atmosphere.

A similar type of results was reported by Song et al. (2005) that impedance increased gradually from 15 to 100 cycles and then to 250 cycles of heating and cooling at 1030 and 200 ºC, respectively. But the specimen subjected to 400 cycles, the impedance decreased rapidly due to degradation of TGO in terms of changes of microstructures and compositions (Zhang et al. 2005 and Song et al. 2005).

The electrochemical impedance kinetic parameters were obtained from fitting of EIS curves using aforesaid equivalent circuits (Fig. 5.3). The electrical properties such as polarization resistance (R_{SSA}) and capacitance (C_{SSA}) of SSA top coat at the different pre-oxidation time is shown in Fig. 5.6 (a and b). The plot clearly shows the initial increase in R_{SSA} up to 20 h followed by reduction at 30 h [Fig. 5.6 (a)]. At the same time, a gradual decrease in C_{SSA} is observed up to 20 h, and then there is an abrupt increase in capacitance indicates failure of top coat occurs only after exposure to 30 h [Fig. 5.6 (b)]. Byeon et al. (2005) have studied EIS of multilayered YSZ TBCs by atmospheric plasma spray and electron-beam physical vapor deposition (EB-PVD) techniques. They found that an increasing oxidation time led the initial increase in resistance of YSZ and TGO. But further increase in time caused to decrease the resistance of YSZ and TGO with an abrupt increase in capacitance due to generation of defects (Jayaraj et al. 2004). These results are good agreement with the present results obtained for SSA TBCs. The resistivity of SSA top coat can be evaluated by

$$R = \frac{\rho.\delta}{S} \tag{5.2}$$

Where R is the resistance; ρ is resistivity; δ is TGO thickness and S is the area of the electrode. The calculated resistivity values of pre-oxidized SSA top coat were found to be 1.4×10^5, 6.3×10^4 and 5×10^3 Ohm cm, for 10, 20, and 30 h respectively. In general, the electrochemical impedance response of thermal barrier coatings depends on the penetration of conductive electrolyte through the pores of ceramic top coat layer. The effective resistivity of SSA coatings during impedance measurement can be expressed as

$$\rho^{eff} = \rho_{SSA} V_{SSA} + \rho_{electrolyte} V_{electrolyte} \tag{5.3}$$

Where, ρ_{SSA} and $\rho_{electrolyte}$ are the resistivities of SSA ceramic and electrolyte (~10^{-2}-10^{-3} Ohm cm), respectively (Zhang et al. 2005). V_{SSA} and $V_{electrolyte}$ denote the volume fraction of SSA and electrolyte, respectively. The resistivity gradually decreases from 10 to 30 h due to the higher volume of conductive electrolyte penetration through

more pores and cracks containing SSA top ceramic layer. After 30 h, SSA top ceramic layer becomes porous and contributes to lower effective resistivity with the decrease in volume fraction of SSA according to Eq. (5.3).

5.1.3 Growth kinetics and compositional changes of SSA TGOs

The growth of TGO and its composition is most important for the understanding of oxidation characteristics of TBCs (Ni et al. 2011). The continuous TGO layer could be seen at the interface between NiCrAlY bond coat and SSA top coat after exposure to 1050 ºC for different pre-oxidation times of 10, 20, and 30 h in the argon atmosphere [Fig. 5.4]. The thickness of TGO was measured using SEM micrographs and found to be about 4±1, 5±1 and 6±2 µm. It is observed that the growth of oxide layers increased with an increasing pre-oxidation time which is more consistent with the previous investigations (Nath et al. 2014 and Ahmadian 2014). The growth of TGO layer was found to be dependent on the oxidation temperature and duration due to the phase transformations from γ to θ to α-Al_2O_3 phases at 1000-1200 ºC (Fox et al. 2004). In this work, an instantaneous increment of TGO thickness was found to be about 4 µm in the onset of pre-oxidation treatment corresponded to nucleation and growth of α-Al_2O_3 at different sites of bond coat and top coat interface. This process was continued until a thin layer of TGO covering the entire bond coat surface up to 10 h. Once the TGO layer is formed at the interface, it protects the bond coat from further oxidation. Only a slight increment in TGO thickness from 4 to 5 µm was observed at 20 h due to the presence of protective Al_2O_3 scale. When the oxide scale thickens from 5 to 6 µm at the end of 30 h, the growth stresses caused to form defects such as porosity and cracks inside the TGO layer.

The detailed EDS analysis at TGO-top coat interface of TBCs is well explained in chapter 4 (section 4.3). The shifting of relaxation frequency zone (10^0-10^1 Hz) for TGO layer is observed in Fig. 5.1 (d), which indicates the impedance of TGO layer increases with increasing pre-oxidation time from 10 to 20 h. In other words, an increasing pre-oxidation duration increases the TGO thickness which caused to increase impedance from 10 to 20 h according to Eq. 5.3. But further

increasing the time to 30 h caused to reduce the impedance due to microstructure and compositional changes of TGO layer. The relation between the maximum of the absolute values of phase angles (Φ) and respective frequencies (f) with polarization resistance (R_p) are given by the following Eqs. (5.4 and 5.5)

$$f_{\max} = \frac{1}{2\pi C R_p}\left[1+\frac{R_p}{R_s}\right] \tag{5.4}$$

$$\varphi_{\max} = \arctan\frac{R_p}{2\left[R_s(R_s+R_p)\right]^{1/2}} \tag{5.5}$$

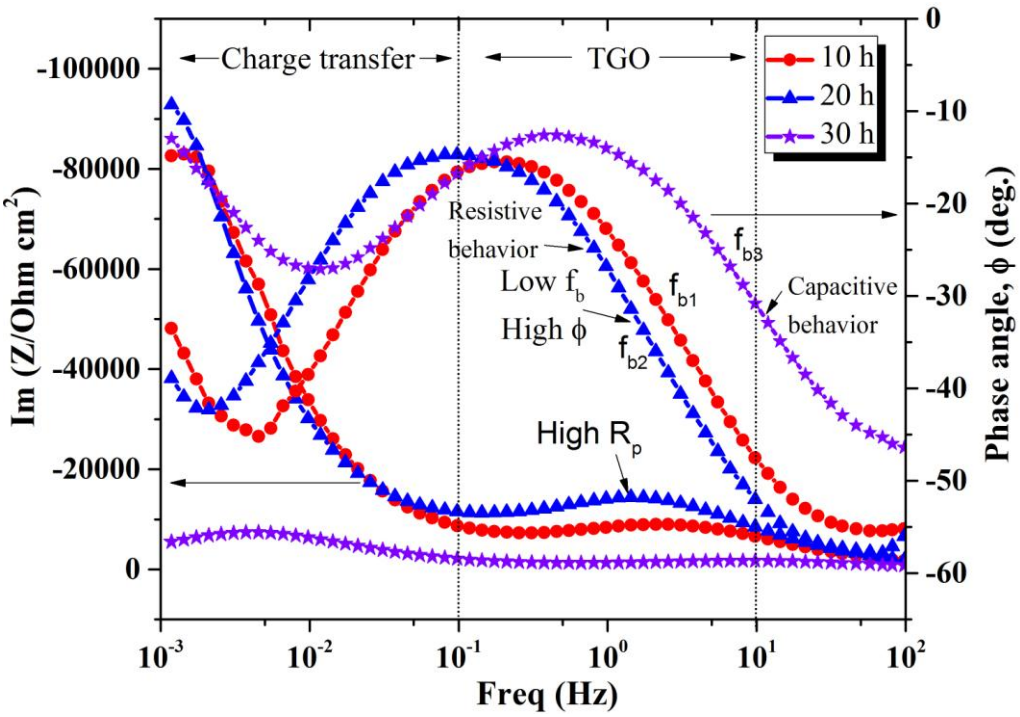

Fig. 5.7: Frequency dependence of -Im (Z) and Φ for pre-oxidized SSA TBCs after exposure to 1050 ºC.

According to Eq. 5.4 it is observed that an increase of R_p at constant C and R_s moves f_{max} to lower frequency. Similarly, an increase of R_p at constant R_s moves Φ_{max} to higher phase angle (Marcus et al. 2006). In the present study, the obtained modulus of impedance and corresponding phase angle values were plotted with respect to frequency as shown in Fig. 5.7. The highest modulus of impedance was found for

20 h in both TGO and charge transfer region as compared to 10 and 30 h of pre-oxidation, which indicates a reduction in R_p from 20 to 30 h caused to shifts the frequency from f_{b2} to f_{b3}. The variation in phase angle (Φ_{TGO}) with respect to polarization resistance (R_{TGO}) were also seen at the frequency of 10^0 and 10^{-3} Hz in TGO zone and TGO-bond coat interface, respectively which were reported in Table 5.1.

Table 5.1: Fitting data from EIS spectra of the pre-oxidized SSA TBCs after pre-oxidation at 1050 ºC.

Pre-oxidation time (h)	Region	Phase angle, Φ (deg.)	Polarization resistance, R_p ($Ohm.cm^2$)
10	TGO	22	3.0×10^4
	TGO/BC interface	33	3.2×10^5
20	TGO	27	4.3×10^4
	TGO/BC interface	39	4.8×10^5
30	TGO	14	6.2×10^3
	TGO/BC interface	13	1.9×10^4

The highest phase angle was found for 20 h (Φ=27º) showed R_{TGO} is about 4.3×10^4 Ohm cm^2 due to the presence of pure Al_2O_3 protective layer at the interface. The lowest phase angle was found for 30 h (Φ=14º) showed R_{TGO} is about 6.1×10^3 Ohm cm^2 mainly due to the presence of conductive oxides and defects in the TGO. In general, the shift of phase angle towards 90º indicates the presence of the resistive type of oxide film and vice versa. Zhang et al. (2017) have investigated anodization of two industrial aluminium alloys (AA 6082 and 7075) using EIS technique. The anodization result two layer structures on Al alloys which consist of a barrier inner layer and porous outer layer. The EIS fitting was done using CPE_1/R_1 and CPE_2/R_2 series model which represents outer layer close to the electrolyte and inner layer close to the metal substrate, respectively. The inner layer exhibited high capacitance as compared to outer layer due to thin resistive anodic oxide (Zhang et al. 2017). So,

based on these observations it is understood that specimen pre-oxidized at 20 h exhibited the pure resistive type of TGO and capacitive type was observed in the case of 10 and 30 h.

The variation in resistance and capacitance of the SSA TGOs are shown in Fig. 5.6 as a function of pre-oxidation time. Capacitance behavior of SSA TGOs decreases with increasing time and an abrupt increase in capacitance for 30 h indicates there may be a failure or compositional changes in the TGO region. The resistivity of SSA TGOs was found to be 1.5×10^{8}, 1.7×10^{8}, and 2.05×10^{7} Ohm cm for 10, 20, and 30 h, respectively. The resistance and capacitance from the charge transfer effect (R_{ct} and C_{ct}) are shown in Fig. 5.6 (a and b). The maximum charge transfer resistance was found at 20 h over 10 and 30 h of pre-oxidation. Higher capacitance for the charge transfer effect was noticed for 10 and 30 h, where the failure actually occurred as shown in Fig. 5.6 (b). Close observation of Fig. 5.6 (a) indicates that the resistance from charge transfer effect changes in the same order of resistance from SSA top coat and TGO. Hence, the resistance from charge transfer effect can be used to reflect the changes of overall resistance in the TBCs components.

The thickness of TGO was calculated using the capacitance values obtained from EIS fitted plots. The capacitance of TGO with their thickness can be related by the following formula

$$C = \frac{\varepsilon\varepsilon_o S}{\delta} \qquad (5.6)$$

Where ε is dielectric constant of α-Al_2O_3; ε_o is vacuum dielectric constant; δ is the TGO thickness and S is the area of the electrode. The calculated values of TGO thickness is shown in Fig. 5.7. So it is evident the thickness of TGO layer increased with pre-oxidation time and followed a parabolic kinetics. An empirical relationship between TGO thickness and pre-oxidation time (t) can be obtained by polynomial fitting from Fig. 5.8 and given as Eq. (5.7).

$$\delta = -0.0025t^2 + 0.097t + 0.74 \qquad (5.7)$$

It shows that a calculated value of TGO thickness from EIS is smaller than the TGO thickness which is obtained from SEM measurements. This is probably due to the presence of Ni and Cr based oxides, which are more conductive than pure Al_2O_3, leads to increasing the capacitance. From the above Eq. 8, it can be said that the time increased from t to t+1 (h), the TGO growth changes by 0.097-0.0025× (2t+1) µm. An increasing trend of TGO thickness was found up to 20 h and followed by reduction at 30 h due to the increasing capacitance behavior (Fig. 5.8).

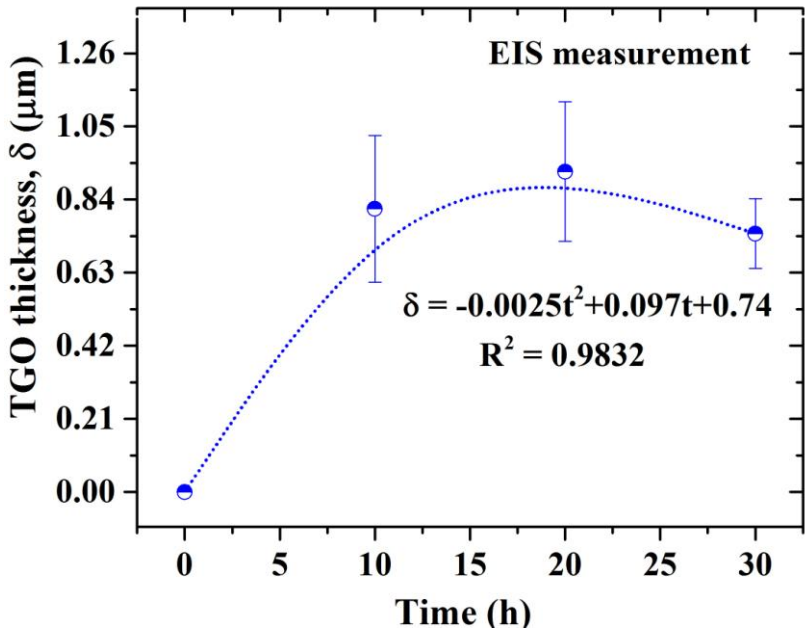

Fig. 5.8: Thickness of SSA TGOs as a function of pre-oxidation time calculated from EIS measurement after exposure to 1050 ºC.

5.1.4 Breakpoint frequency of pre-oxidized SSA TBCs

The breakpoint frequency method has been widely used to evaluate the performance of coatings (Feng et al. 2016). The breakpoint frequency is defined as the frequency at which phase angle 45º and it can be expressed as,

$$f_{45} = K\frac{A_d}{A} \qquad (5.8)$$

Where $\mathbf{A_d}$ and **A** are the delaminated area or reactive area and total exposed area of the sample, respectively. K is the material constant for the coating under study and is equal to $1/2\varepsilon\varepsilon_0\rho_0$. Where ε is the dielectric constant of the coating, ε_0 is the vacuum permittivity and ρ_0 is the ionic resistance of the coating. Since the exposed area is same for all the tested samples, it can be said that the reactive area is directly proportional to the breakpoint frequency at 45º. In the present work the breakpoint frequency is calculated from frequency vs. phase angle plot of SSA TBCs after pre-oxidation at 1050 ºC and it is shown in Fig. 5.9.

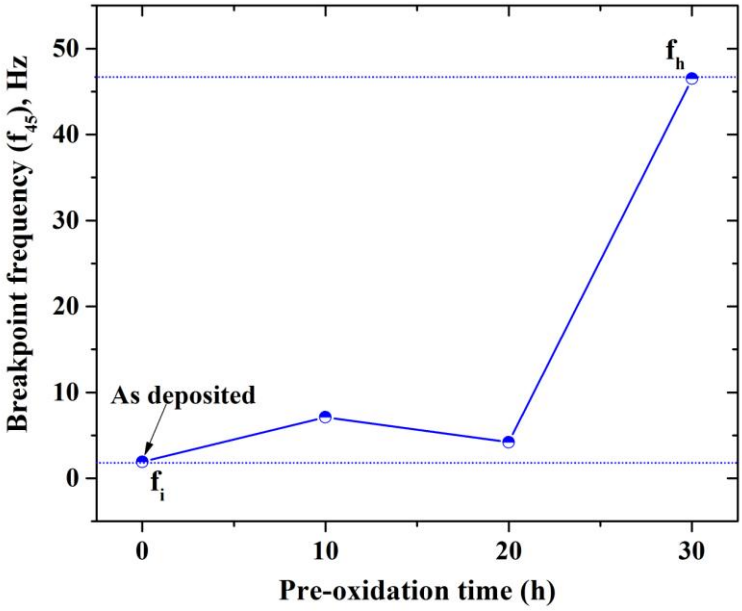

Fig. 5.9: Breakpoint frequency vs. pre-oxidation time of SSA TBCs after exposure to 1050 ºC.

After pre-oxidation treatment, the lowest breakpoint frequency was observed at 20 h than 10 and 30 h which indicated more reactive area was found for 30 h followed by 10 h [Fig. 5.1 (a)]. The 10 and 30 h pre-oxidized samples showed more delaminated and reactive area than 20 which is also supported by porosity and EDX results [Figs. (5.4 and 5.5)].

5.1.5 Residual stresses in the SSA top coat after pre-oxidation treatment

The Raman spectra obtained from the SSA top coat after pre-oxidation treatment at 1050 ºC for different exposure time is shown in Fig. 5.10 (a). In general, Raman spectroscopy is very sensitive to the structure and metal-oxygen stretching modes of oxides. The spectrum indicates that TBC layer is a single phase BCT structure as confirmed by XRD pattern [Fig. 5.10 (b)]. No Raman study of SSA compounds have been reported to date, but for the doped $SrAl_2O_4$ ceramic has been reported by previous researchers (Ayvacıklı et al. 2011 and Escribano et al. 2005). The spectrum exhibited peaks at 108, 195, 224 (low intense) 320 and 465 cm^{-1} (strong intense) attributed to the Sr-Al-O bond in the SSA crystal structure. After pre-oxidation treatment, the frequency shift was observed from 320 to 314.8, 315.4 and 317.9 cm^{-1} for 10, 20, and 30 h of treatment at 1050 ºC.

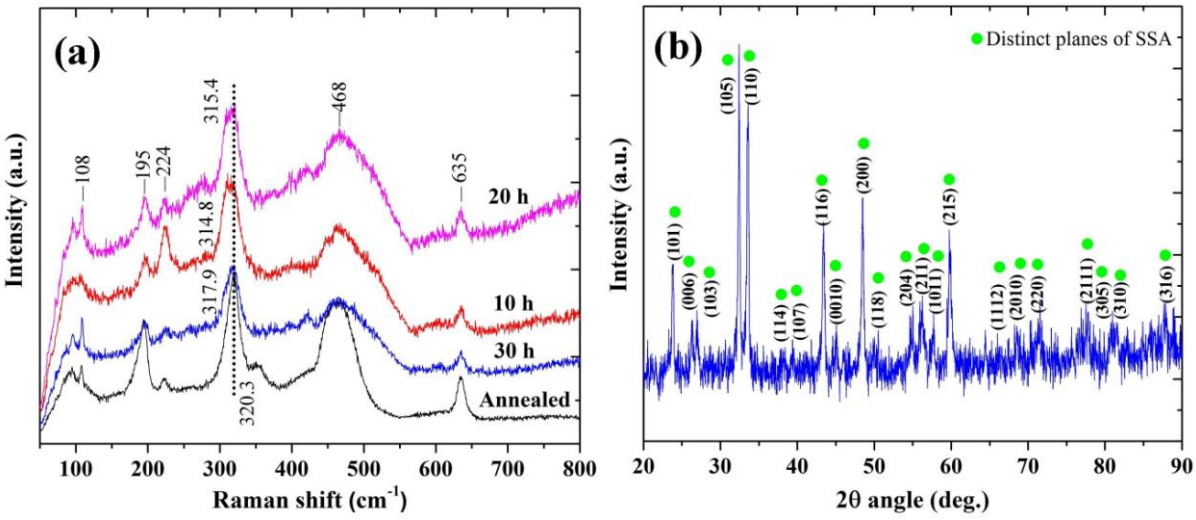

Fig. 5.10: (a) Raman spectra of the SSA top coat after pre-oxidation treatment for different exposure time; and (b) XRD pattern of 30 h pre-oxidized SSA top coat at 1050 ºC in argon atmosphere.

The spectral shift ($\Delta\Omega$) between stress-free and pre-oxidized SSA TBC samples is shown in Table 5.2.

Table 5.2: Spectral shift ΔΩ of the band at 320 cm^{-1} in the SSA top coat.

Pre-oxidation time (h)	Bi-axial residual stress (GPa)
10	5.57
20	4.96
30	2.39

It could be seen that the positive shift increased with increasing pre-oxidation duration. So, it is understood that the residual tensile stresses decreased in the SSA top coat with increasing pre-oxidation time at 1050 ºC. Generally, TGO layer posses larger residual compressive stresses due to thermal expansion mismatch with the ceramic top coat when its cools down to atmospheric temperature. Tomimatsu et al. (2003) have studied the residual stress distribution of Electron beam-physical vapor deposited (EB-PVD) deposited YSZ TBCs by Raman spectroscopy. It was proved that stress in the TBC layer has a distribution (compressive and tensile) and maximum stress was observed at the bond coat and top coat interface and gradually decreased towards top coat.

It is also obvious that an increasing TGO growth induces higher residual stresses in the top coat. But in the present study, the 30 h treated SSA TBC samples showed almost 59% lower tensile stress as compared to 10 and 20 h due to the presence of more porosities and cracks in the SSA top coat (Fig. 5.5). The presence of defects in the SSA top coat was helped to mitigate the residual stresses for 30 h of pre-oxidized specimens. A relationship between the polarization resistance and residual stress formation of SSA top coat as a function of different pre-oxidation duration is shown in Fig. 5.11.

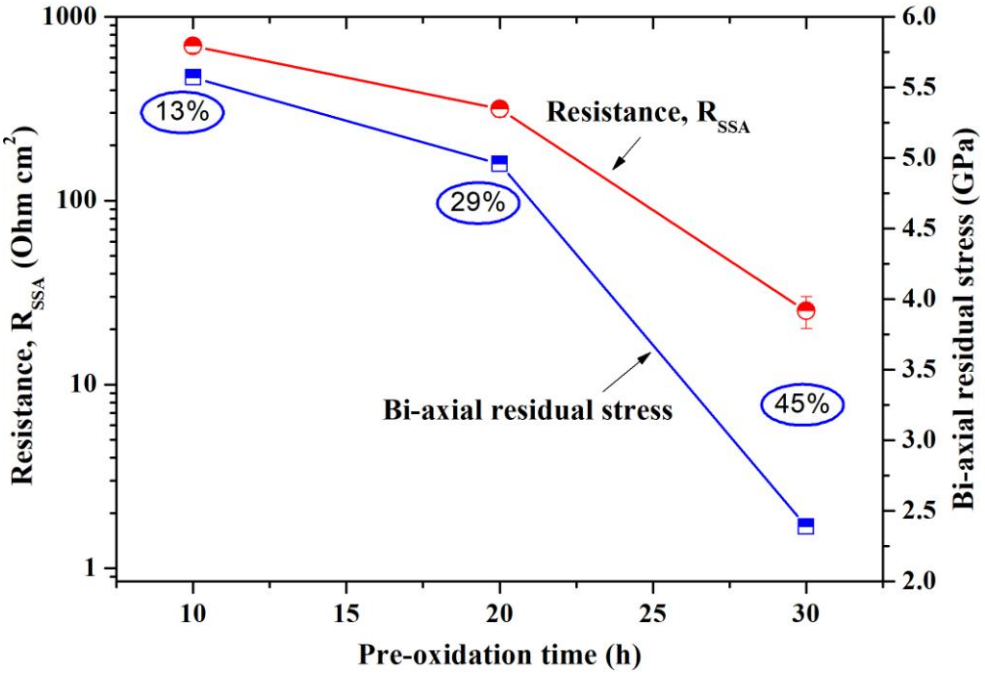

Fig. 5.11: Polarization resistance and bi-axial residual stress of SSA top coat after exposure to pre-oxidation at 1050 ºC for different duration.

As discussed above, a decreasing trend of R_{SSA} and residual stresses was observed with an increase in pre-oxidation times of 10, 20 and 30 h which mainly due to increasing porosities of the top coat (13, 29 and 45%). It was well proved that the ceramic top coat defects such as pores and micro-cracks play a vital role on thermal insulation and thermal shock resistance of the coatings at the higher temperature.

5.2 Microstructure and electrical property relation of pre-oxidized SSA TBCs

5.2.1 Microstructure of SSA top coat and TGO after oxidation test in air

Fig. 5.12 shows the SEM cross-sectional micrographs and respective EDS micro-region analysis of oxidized SSA TBCs after exposure to 1100 ºC in the air. Severe coating damages were observed in the 10 h pre-oxidized SSA TBCs [Fig. 5.12 (a)] than that of 20 and 30 h [Fig. 5.12 (b and c)]. The top coat microstructure of 30 h pre-oxidized specimens showed more interconnected vertical cracks as compared to 20 h due to sintering of SSA ceramic at 1100 ºC.

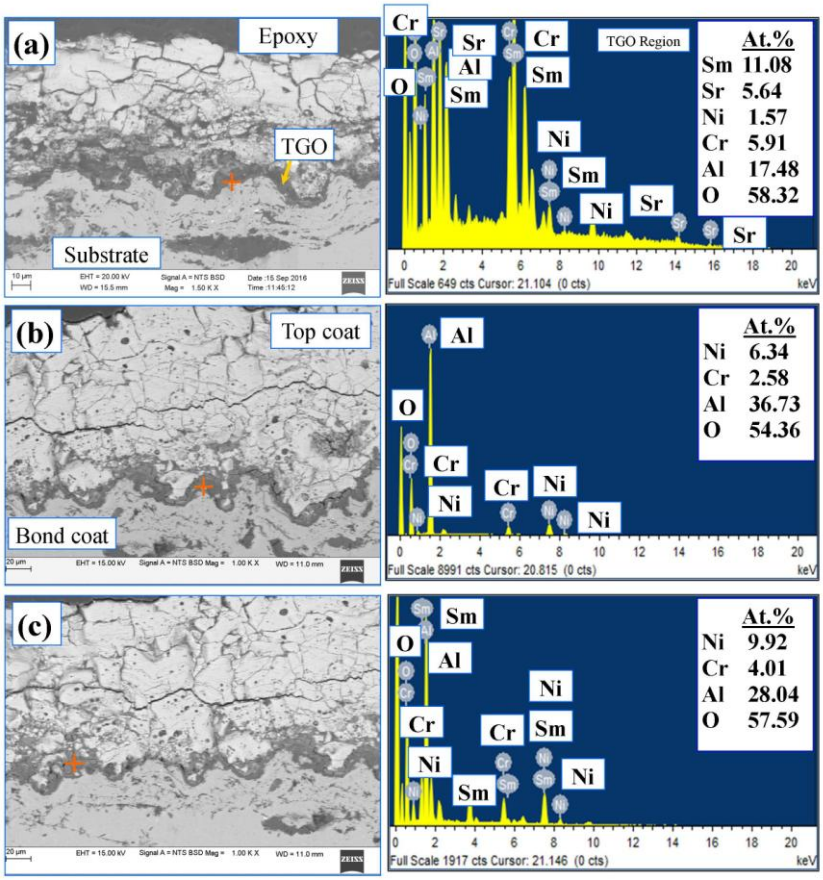

Fig. 5.12: Cross-sectional SEM micrographs and corresponding EDS micro-region analysis of oxidized SSA TBCs at 1100 ºC for 15 h in air; (a) SSA TBCs 10 h; (b) SSA TBCs 20 h; and (c) SSA TBCs 30 h pre-oxidized at 1050 ºC.

The thickness of TGO varies as 9.5±2, 6±2, and 8±3 µm, for 10, 20, and 30 h pre-oxidized specimens, respectively. The lowest growth of TGO was observed at 20 h than 10 and 30 h because of stable and high pure α-Al_2O_3 TGO obtained during pre-oxidation treatment at 1050 ºC. EDS analysis was conducted near to TGO-top coat interface of all pre-oxidized specimens, which revealed the presence of Al and O elements with an atomic ratio of (Al: O=0.299; 10 h), (Al: O=0.666; 20 h) and (Al: O=0.486; 30 h) for Al_2O_3 TGO scale. The suitable atomic ratio for Al_2O_3 was found at 20 h, indicates higher chemical stability of TGO at 20 h. In addition to Al and O elements, the other elements such as Ni, Cr, and Sm are also found at the interface between TGO and top coat.

Fig. 5.13 (a and b) shows the Nyquist and Bode impedance plots of SSA TBCs after exposure to 1100 ºC in the air.

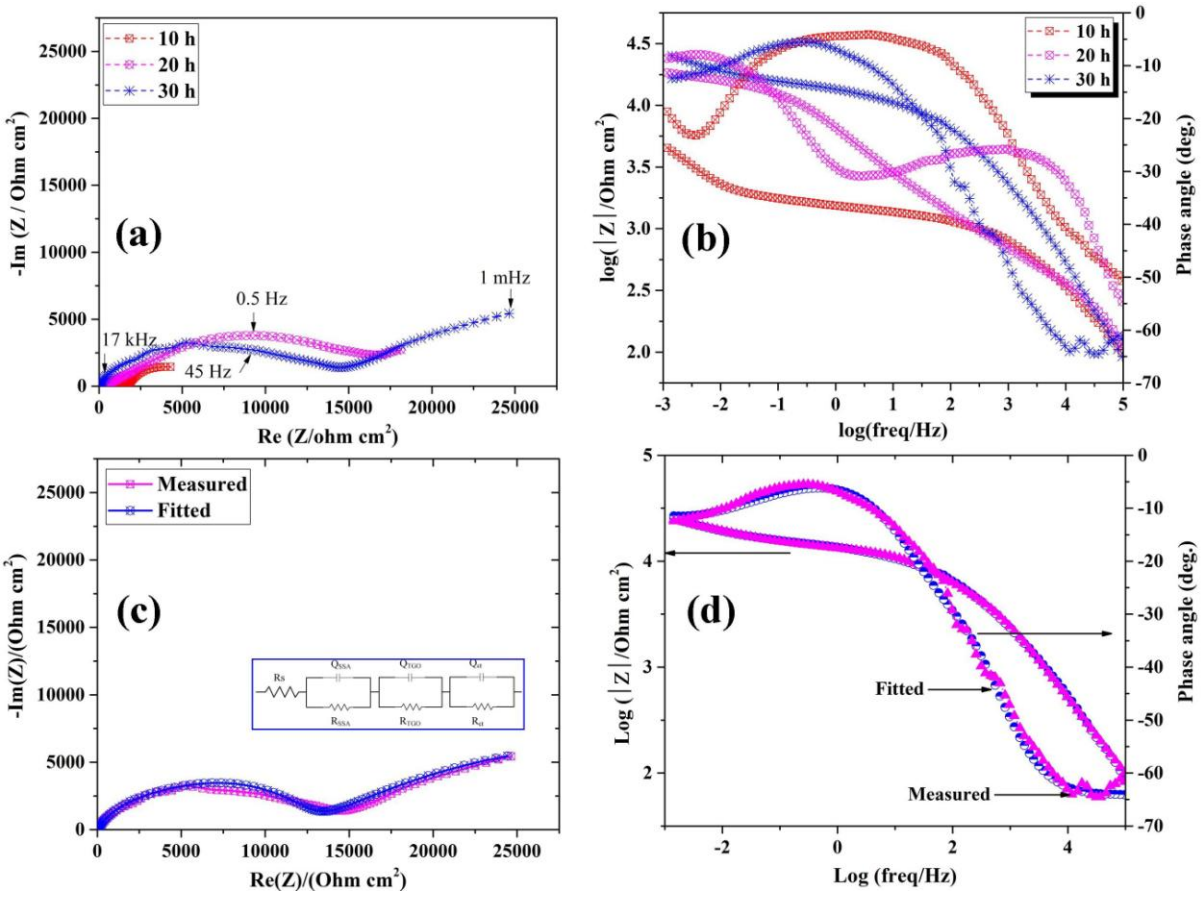

Fig. 5.13: (a) Nyquist impedance; and (b) Bode phase angle plot as a function of frequency of pre-oxidized SSA specimens after exposure to oxidation of 1100 ºC for 15 h in air.

With an exception of the charge transfer effect in the low-frequency zone, the overall resistance of TBCs characterized by the intercept of the real part impedance, which is higher for 20 h pre-oxidized specimens followed by 30 and 10 h [Fig. 5.13 (a)]. The typical relaxation frequency for the TGO layer is about 10^0-10^1 Hz and this response can be clearly seen in the case of 20 h than 30 and 10 h [(Fig. 5.13 (b)] due to the presence of continuous TGO layer at the interface between bond coat and top coat [Fig. 5.12 (b)]. The Nyquist plot was fitted based on a model of 3 R/CPE in the series connection as shown in Fig. 5.13 (c and d).

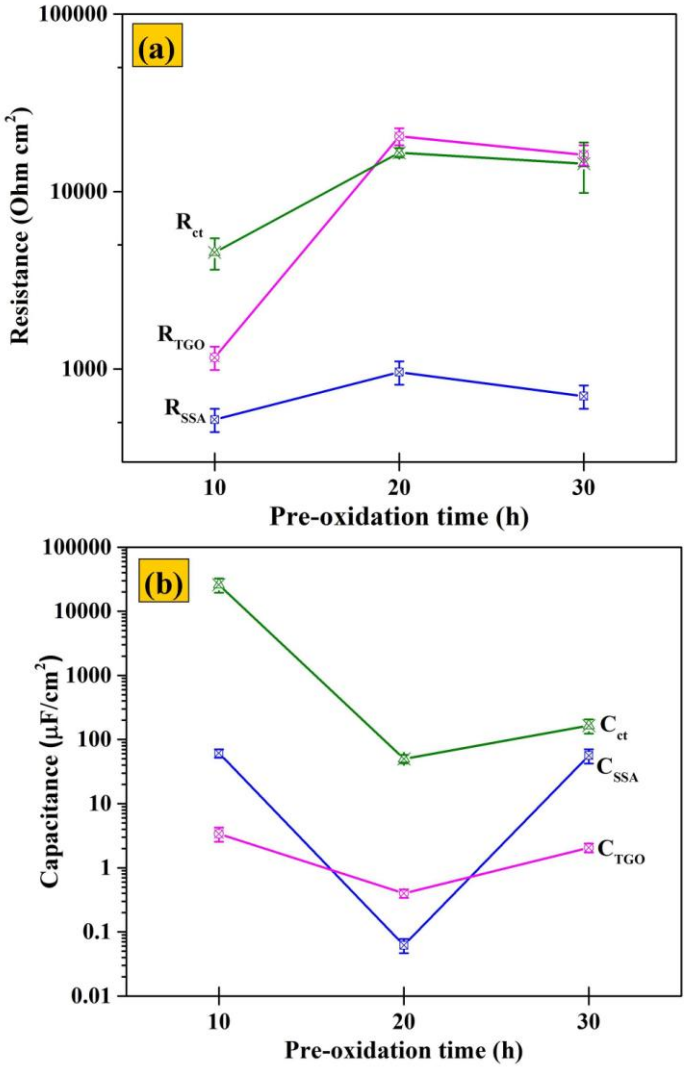

Fig. 5.14: Resistance and capacitance of SSA TGO after isothermal oxidation as a function of different pre-oxidation duration at 1100 ºC for 15 h in air.

It is evident that measured impedance results are well matched with simulated results. Fig. 5.14 (a) showed 20 h pre-oxidized specimen exhibited highest top coat and TGO resistance. It is also indicated the resistance changes from charge transfer effect are in the same order of changes in resistance of SSA top coat and TGO.

Fig. 5.14 (a) also revealed highest charge transfer resistance for 20 h pre-oxidized samples which caused by the presence Al_2O_3 insulator at the interface.

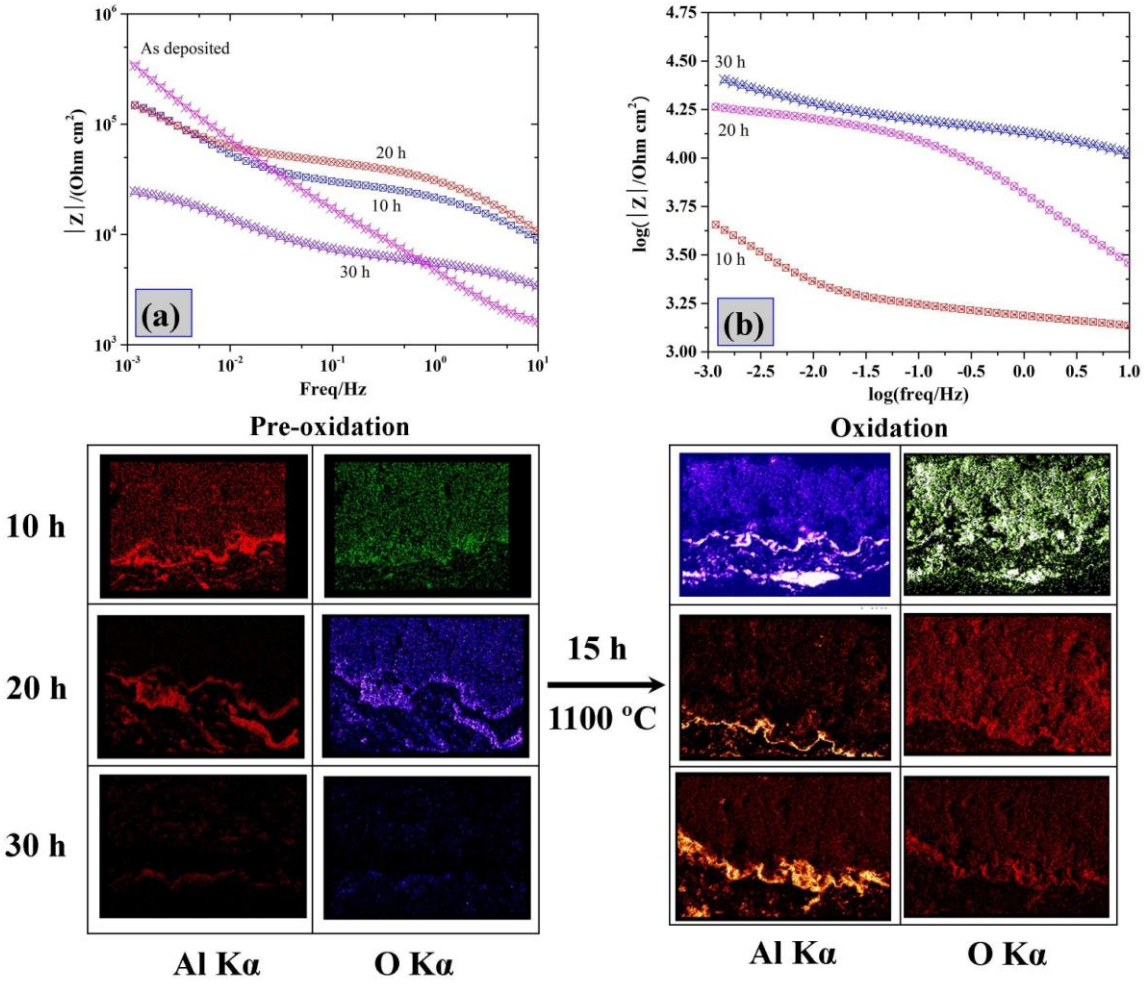

Fig. 5.15: Bode modulus impedance plots and corresponding cross-sectional elemental mapping of the SSA TBCs after exposure to (a) pre-oxidation treatment at 1050 ºC; and (b) oxidation treatment at 1100 ºC.

But in other cases such as 10 and 30 h, the presence of conductive NiO, Cr_2O_3, and $NiCr_2O_4$ which act as a p-type semiconductor, increases the charge transfer due to the presence of more vacancy sites. The highest capacitance of SSA top coat, TGO and charge transfer effect were noticed for 10 h pre-oxidized specimens [Fig. 5.14 (b)], at which the failure of TBCs occurred as shown in [Fig. 5.12 (a)]. According to Eq.5.6 the capacitance of TGO is inversely proportional to thickness. Even though the specimens subjected to 10 and 30 h pre-oxidation exhibited much higher TGO thickness than 20 h, it showed higher capacitance due to the degradation of protective Al_2O_3 TGO into conductive mixed oxides at the interface. Fig. 5.15 shows the magnified low-frequency regimes of Bode modulus impedance plots and

corresponding X-ray elemental mapping of both pre-oxidized and oxidized SSA TBCs after exposure to 1050 and 1100 ºC, respectively. It showed that the charge transfer resistance of 20 h pre-oxidized SSA TBCs is higher than 10 and 30 h due to the presence of pure Al_2O_3 at the interface [Fig. 5.15 (a)].

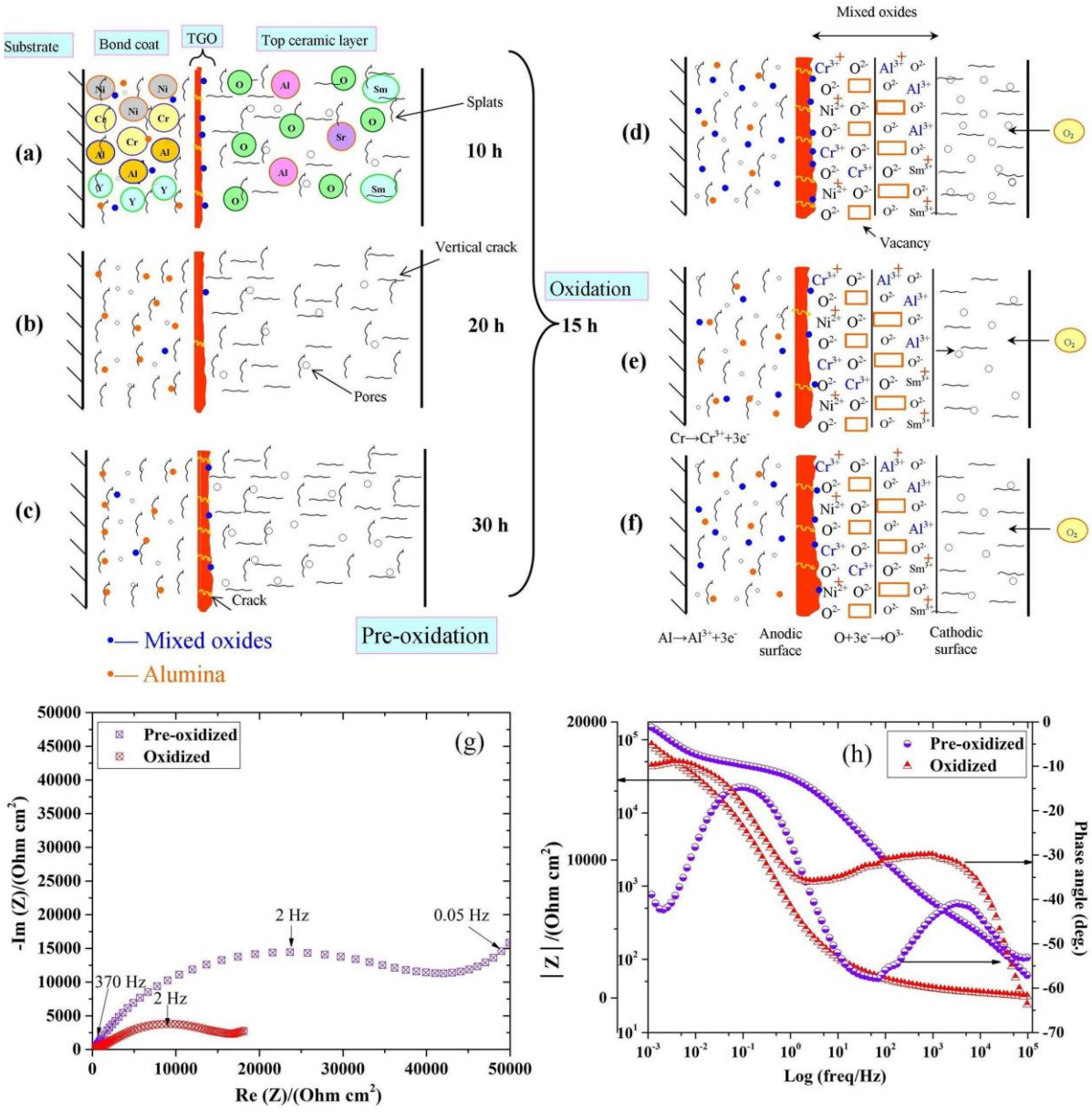

Fig. 5.16: Schematic illustration of formation of TGO after pre-oxidation at 1050 ºC for (a) 10; (b) 20; (c) 30 h; (d, e and f) defect oxide structure of TGO after oxidation at 1100 ºC for 15 h in air, (g) Nyquist; and (h) Bode impedance plots of 20 h pre-oxidized specimen after oxidation in the air.

The respective EDS mapping analysis of SSA TBCs after pre-oxidation, Al and O elements with large concentrations are present at the interface of bond coat and TGO indicates a larger content of Al_2O_3 (20 h) which offered more resistance against current flow. Similarly, pre-oxidized SSA TBCs exposed to oxidation at 1100 ºC in the air, 10 h treated specimen showed lower charge transfer resistance [Fig. 5.15 (b)] than 20 and 30 h, due to the presence of discontinuous Al_2O_3 at the interface of TGO-bond coat and degraded top coat.

Fig. 5.16 shows the schematic representation of electrochemical redox reactions of SSA TBCs after exposure to pre-oxidation and oxidation treatment at 1050 [Fig. 5.16 (a-c)] and 1100 ºC [Fig. 5.16 (d-f)], respectively. During the initial stages of the pre-oxidation process, the metallic aluminium in the bond coat reacted with atmospheric oxygen to form the aluminum oxide at 1050 ºC. The formed oxide ligands grow in the lateral direction and form continuous TGO layer at the bond coat and top coat interface. Further, degradation of TGO layer in the microstructure and composition led diffusion of Ni and Cr from metallic bond coat to TGO-top coat interface. The higher percentage of Ni (7.05 at.%) and Cr (2.27%) were seen for the pre-oxidation treatment of 10 h followed by 30 h (1.30 at.% Ni and 0.53 at.% Cr) and 20 h (1.17 at.% Ni and 0.00 at.% Cr) at the TGO-top coat interface due to the absence of high purity TGO after pre-oxidation test at 1050 ºC [Fig. 5.16 (a-c)]. The presence of NiO and Cr_2O_3 play an important role in the formation of mixed oxides after oxidation test at 1100 ºC for 15 h in the air which directly affects diffusivity of metallic ions and oxygen.

In presence study, 20 h pre-oxidized sample exhibited significantly the lowest percentage of Cr (2.58 at.%) at the top coat-TGO interface than 10 h (5.91 at.%) and 30 h (4.01 at.%) due to the presence of highly enriched α-Al_2O_3 TGO after oxidation test at 1100 ºC for 15 h in air. The variation of Ni was also seen in the TGO-top coat interface as 1.57, 6.34, and 9.92 at. % for the pre-oxidation treatment times of 10, 20, and 30 h, respectively after oxidation test. It seems low Ni availability for 10 h; however, the highest presence of Cr was found for the same pre-oxidized specimens after oxidation test at 1100 ºC. So, it is interesting to understand the role of Cr^{3+} ions

diffusion into the NiO lattice after exposure to oxidation test in the air. It is well known that the minimum $3Cr^{3+}$ ions require to form an extra metal vacancy sites in the NiO lattice (Greskovich, 1970) and it can be represented by the Kroger-Vink notation (Eq. 5.9) [Fig. 5.16 (d-f)].

$$3NiO \xrightarrow{3Cr_2O_3} V_{Ni}^{\bullet\bullet} + 6O_O^x + Ni_{Ni}^{\bullet} \qquad (5.9)$$

Where, $V_{Ni}^{\bullet\bullet}$ is a nickel vacancy with positive charges, O_O^x an oxygen ion sitting on an oxygen lattice, with a neutral charge and $Ni_{Ni}^{\bullet}$ is a nickel ion sitting on a nickel lattice site, with single positive charge.

The value of diffusion coefficient of Cr^{3+} ions into NiO lattice through the protective TGO layer at the interface can be calculated using Wagner's oxidation theory (Moore, 1981). The parabolic rate constant can be directly related to diffusion coefficient as follows (Fox et al. 2004):

$$\left(\frac{\Delta m}{A}\right)^2 = \left(\frac{D_{Cr^{3+}} M_{Al_2O_3} \rho_{Al_2O_3} dc_{Ni^{2+}}}{jA_m}\right) t \qquad (5.10)$$

Where $(\Delta m/A)^2$ / t is the parabolic rate constant ($g^2\ cm^{-4}\ s^{-1}$), $D_{Cr^{3+}}$ is the diffusion coefficient ($m^2\ s^{-1}$) of Cr metal ions, M and ρ are the molar mass (102 g mol^{-1}) and density (3.97 g cm^{-3}) of α-Al_2O_3, respectively, dc is the concentration of Ni^{2+} vacancies (g m^{-3}), j is the no of atoms of O^{2-} required to form 1 mole of Al_2O_3 and A_m is the atomic mass of oxygen.

In chapter 4 the parabolic rate constant (k_p) was calculated to be 6.08×10^{-11}, 3.90×10^{-11} and 4.55×10^{-11} $mg^2\ cm^{-4}\ s^{-1}$ for 10, 20, and 30 h of pre-oxidation treatment after exposure to oxidation test at 1100 ºC for 15 h in the air (Baskaran et al. 2017). These values were substituted into Eq. 11 and the corresponding values of the $D_{Cr^{3+}}$ ions in NiO lattice were calculated and reported in Table 5.3. The lowest

$D_{Cr^{3+}}$ was found at 20 h of pre-oxidation (2.28×10^{-15} m^2 s^{-1}) over 10 and 30 h due to the presence of highly enriched α-Al_2O_3 TGO layer at the interface or the presence of lowest amounts of Cr_2O_3 (5.6 mol.%). A slightly higher $D_{Cr^{3+}}$ observed at 10 (4.0×10^{-15} m^2s^{-1}) and followed by 30 h (3.1×10^{-15} m^2s^{-1}) due to the formation of higher amounts of 8.9 mol. % and 7.8 mol. % Cr_2O_3 respectively. Hence, the lowest $D_{Cr^{3+}}$ in the NiO which reduced the formation of more metal ion vacancies after exposure in the air at 1100 ºC for 15 h caused to exhibit highest oxidation resistance (lowest k_p value) for 20 h of pre-oxidized specimens as compared to 10 and 30 h (Baskaran et al. 2017). However, in the case of 10 and 30 h pre-oxidized specimens exhibited significantly higher k_p values due to the greater $D_{Cr^{3+}}$ values which increased the formation of more metal vacancies. As a result, the 10 and 30 h treated SSA TGO allowed more oxygen diffusion towards the metallic bond coat which caused higher oxidation at 1100 ºC for 15 h.

Table 5.3: Diffusion coefficients of Cr^{3+} in NiO through TGO layer at the interface after exposure to 1100 ºC in the air.

Pre-oxidation time (h)	Oxidation temperature (ºC)	Oxidation time (h)	Parabolic rate constant k_p (mg^2 cm^{-4} s^{-1}) $\times10^{-5}$	Cr_2O_3 in NiO (mol.%)	Diffusion coefficient (m^2 s^{-1})$\times10^{-15}$
10	1100	15	6.08	8.9	4.0
20	1100	15	3.90	5.6	2.3
30	1100	15	4.55	7.8	3.1

Fig. 5.15 (g and h) shows the Nyquist and Bode plots of the sample exposed to 20 h of pre-oxidation at 1050 ºC followed by oxidation test at 1100 ºC for 15 h in the air. Both the plots clearly revealed that pre-oxidized sample showed higher

polarization resistance than those of oxidized one which is mainly due to the presence of insulator type Al_2O_3 in the TGO. After oxidation test, the formed conductive mixed oxides of Ni and Cr at the TGO-top coat interface make TGO more conductive than pure Al_2O_3. These observations clearly revealed that an increasing metal ion vacancy sites in the mixed oxides decreased the impedance response after exposure to 1100 ºC. At the TGO-top coat interface, the Sm_2O_3 reacted with Al_2O_3 to form $SmAlO_3$ when exposed to the higher temperature at 1100 ºC (Eq. 5.11) (Nijdam et al. 2005 and Zhao et al. 2011)

$$Sm_2O_3 + Al_2O_3 \rightarrow 2SmAlO_3 \quad (5.11)$$

$$NiO + Cr_2O_3 \rightarrow NiCr_2O_4 \quad (5.12)$$

Subsequently, the rate of diffusion of Ni and Cr from the metallic bond coat might be quite faster through already degraded TGO layer and formed NiO and Cr_2O_3 just beneath the top coat ceramic layer. These oxides reacted themselves to form $NiCr_2O_4$ at the interface of TGO-top coat (Eq. 13) (Yuan et al. 2008). A plot of polarization resistance of TGO and diffusion coefficient of Cr^{3+} ions in the NiO at the TGO-top coat interface of pre-oxidized SSA TBCs after exposure to oxidation at 1100 ºC is shown in Fig. 5.17.

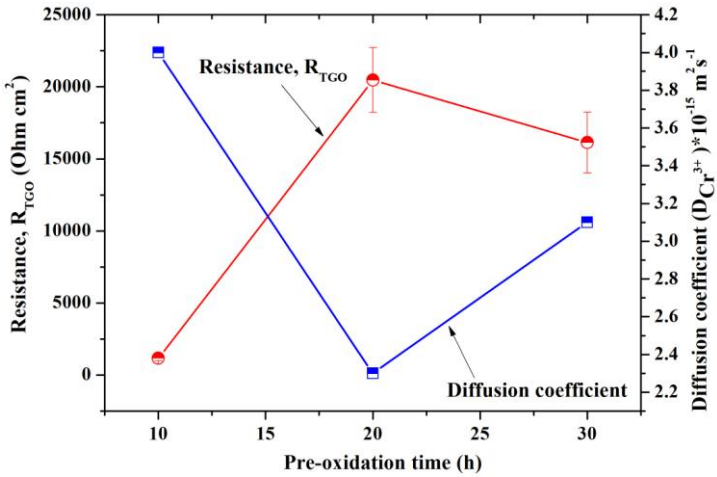

Fig. 5.17: Polarization resistance of TGO and diffusion coefficient of Cr^{3+} ions in the NiO at the TGO-top coat interface of pre-oxidized SSA TBCs after exposure to oxidation at 1100 ºC in the air.

An increase in polarization resistance of TGO is about 94% being found from 10 to 20 h of pre-oxidized SSA TBCs due to the lowest $D_{Cr^{3+}}$ in the NiO at the TGO-top coat interface. This observation clearly indicated that the presence of lowest content of mixed oxides in the TGO (at 20 h) considerably increases the polarization resistance of TGO after oxidation at 1100 ºC. From these observations, it is understood that the total resistance of SSA TGO is more susceptible to compositional changes rather than thickness during oxidation at 1100 ºC in the air. Based on the impedance study of oxidized SSA TBCs, it can be concluded that 20 h pre-oxidation time would be sufficient enough to provide defect-free protective TGO layer at the interface for extended thermal exposure in air at the higher temperature.

Summary of EIS study

- The impedance response of SSA TBCs was reduced significantly after oxidation test due to the compositional change of pure α-Al_2O_3 based TGO into more conductive $NiCr_2O_4$.
- The formation of metal ion vacancies at the TGO-top coat interface play a significant role on TGO resistance after exposure to oxidation at 1100 ºC.

CHAPTER 6

6 HOT CORROSION STUDIES OF SSA AND YSZ TBCs

One of the primary tasks for thermal barrier coating is to efficiently protect the underlying superalloy substrate from aggressive corrosive molten salt at high temperature. Hot corrosion is a serious problem in power generation equipment, gas turbines, internal combustion engines, fluidized bed combustion, industrial waste incinerators and the paper and pulp industries. In this chapter hot corrosion study of newly developed SSA TBC and conventional YSZ using air plasma processed were performed in two different environments such as aviation (i) 50 wt.% Na_2SO_4 + 50 wt.% V_2O_5 (Vanadates) and marine (ii) 90 wt.% Na_2SO_4 + 5 wt.% V_2O_5 + 5 wt.% NaCl (Chlorides) environments. It is interesting to examine degradation characteristics of SSA TBC, as there are no reports exemplified the hot corrosion behaviors of SSA top coatings against vanadates and chlorides corrosive environments at elevated temperature.

6.1 Macroscopic observation and hot corrosion assessment

The hot corrosion test of SSA and YSZ TBCs was conducted in 50 wt. % Na_2SO_4 + 50 wt.% V_2O_5 environment at two different temperature 700 and 900 ˚C. The macroscopic images and time elapsed for visible coating failure of SSA and YSZ TBCs are shown in Fig. 6.1. Comparably, the both TBCs showed partial chipping of coating at 700 ˚C and complete spallation of top ceramic layer was observed at 900 ˚C. The SSA TBCs showed 8 and 22 % lower life time at 700 and 900 ˚C, respectively than YSZ TBCs.

Similarly, hot corrosion study of both the TBC was carried out in 50 wt.% Na_2SO_4 + 5 wt.% V_2O_5 + 5 wt.% NaCl environment and macroscopic images of SSA and YSZ TBCs showed the severity of hot corrosion at 900 than 700 ˚C [Fig. 6.2 (a-c)]. The hot corrosion life of SSA TBCs was found to be about 13 and 39% lower than YSZ TBCs [(Fig. 6.2 (d)]. Interestingly, it is observed that SSA TBCs, partial

chipping of ceramic layer occurred leaving an SSA TBCs intact on bond coat layer [Fig. 6.1 (a and b)] in both the temperatures 700 and 900 ˚C in 50 wt.% Na_2SO_4 + 50 wt. % V_2O_5 corrosive salt.

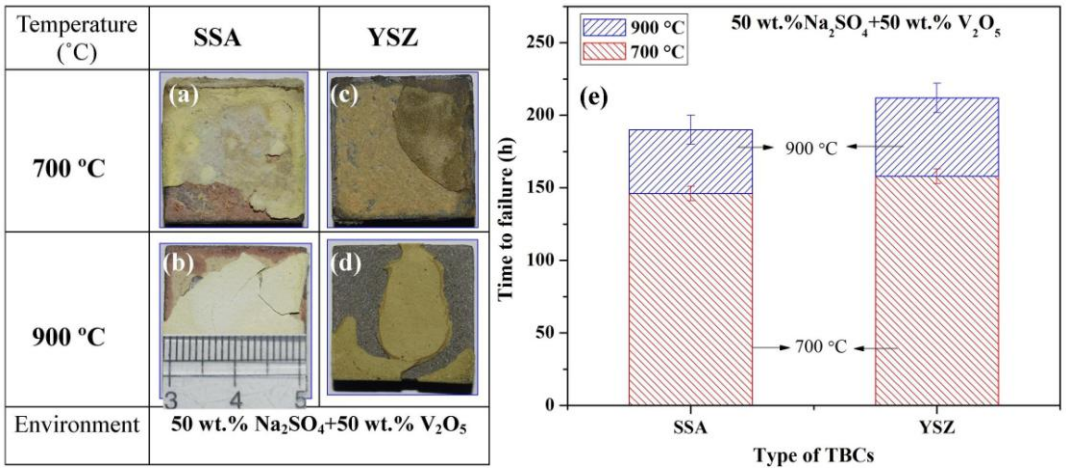

Fig. 6.1: Time elapsed for initial spallation of SSA and YSZ coatings subjected to hot corrosion in (a) 50 wt.% Na_2SO_4 + 50 wt.% V_2O_5 environment at 700 and 900 ˚C.

These observations suggests that findings require comprehensive phase and microscopic analysis in order to understand the possible cause of failure and mechanisms involved in both vanadates and chlorides containing environments at 700 and 900 ˚C for SSA TBC.

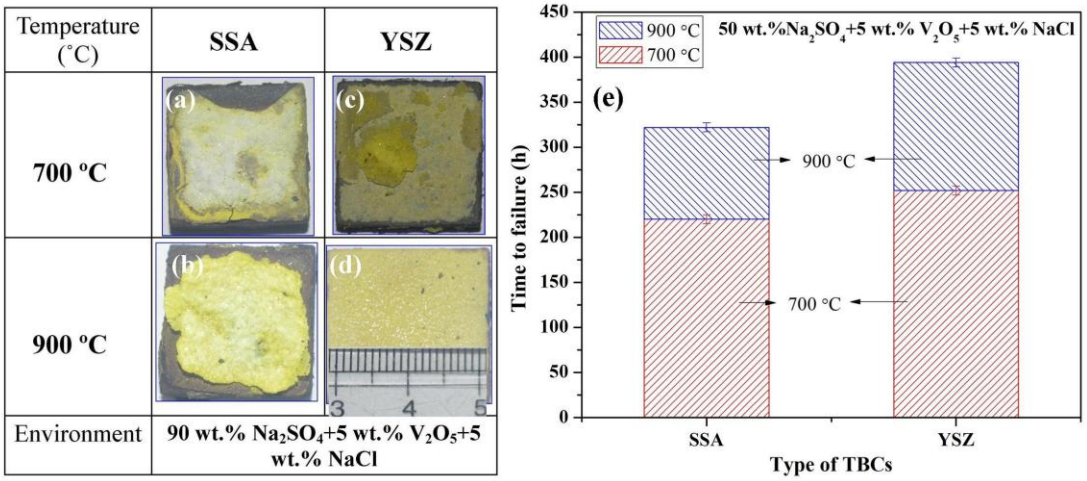

Fig. 6.2: Time elapsed for initial spallation of SSA and YSZ coatings subjected to hot corrosion in (a) 90 wt.% Na_2SO_4 + 5 wt.% V_2O_5 + 5 wt.% NaCl environment at 700 and 900 ˚C.

6.2 Characterization of SSA TBCs after hot corrosion in 50 wt.% Na_2SO_4 + 50 wt.% V_2O_5 atmosphere at 700 and 900˚C

An XRD characterization tool was used to study phase transformation of top coat ceramic before and after subjected to hot corrosion in vanadates and chlorides environments at 700 and 900 ˚C. Fig. 6.3 (a) shows the XRD pattern of as deposited SSA coatings and it was found a single phase body centered tetragonal phase which is already reported in previous chapter (Baskaran et al. 2017).

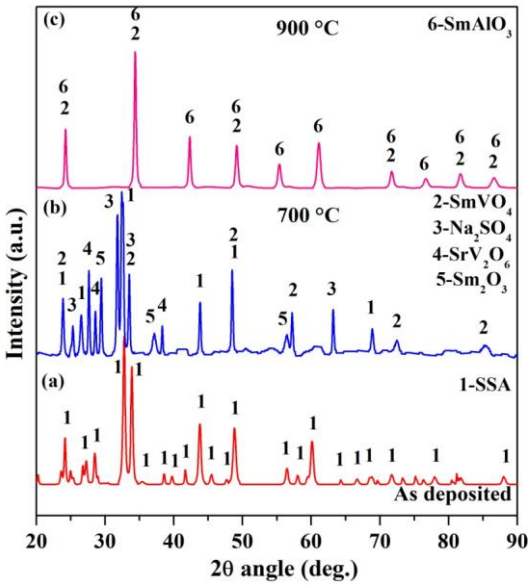

Fig. 6.3: XRD pattern of SSA TBCs; (a) as deposited; (b) and (c) after exposure to hot corrosion in 50 wt.% Na_2SO_4 + 50 wt.% V_2O_5 environment at 700 and 900 ˚C, respectively.

After exposure to molten vanadates and sulfates (equal molar ratio) corrosive salt at 700 and 900 ˚C, it showed additional peaks in the XRD pattern which are recognized $SmVO_4$, SrV_2O_6 and un-melted sulfate salt at 700 ˚C [(Fig. 6.3 (b)] and $SmVO_4$ and $SmAlO_3$ at 900 ˚C [(Fig. 6.3 (c)]. An observation of Na_2SO_4 peaks in Fig. 6.3 (b) indicating that Na_2SO_4 has not been consumed completely at 700 ˚C. But these diffraction peaks disappeared at 900 ˚C due to complete melting of Na_2SO_4. A typical surface morphology of SSA TBCs after hot corrosion test in 50 wt. % Na_2SO_4 + 50 wt. % V_2O_5 atmosphere at 700 ˚C is shown in Fig. 6.4 (a-c). The higher magnification images of selected regions in Fig. 6.4 (a) are shown in Fig. 6.4 (b and c), it is clearly

exhibited the formation of new rods type structures and pyramid like crystals. EDS analysis was performed at different regions of hot corroded surface of SSA TBCs to find out the chemical compositions which is reported in Table 6.1. EDS analysis performed in selected region in Fig. 6.4 (b and c), it is typically composed of Sm, V and O with the suitable atomic ratio equivalent to $SmVO_4$ phase (Table 6.1). Fig. 6.4 (c) also confirmed the presence of um-melted sodium salt along with Sr, V and O with the atomic ratio equivalent to SrV_2O_6. XRD analysis also established the formation of $SmVO_4$ and SrV_2O_6 formation at 700 which supports the EDS results.

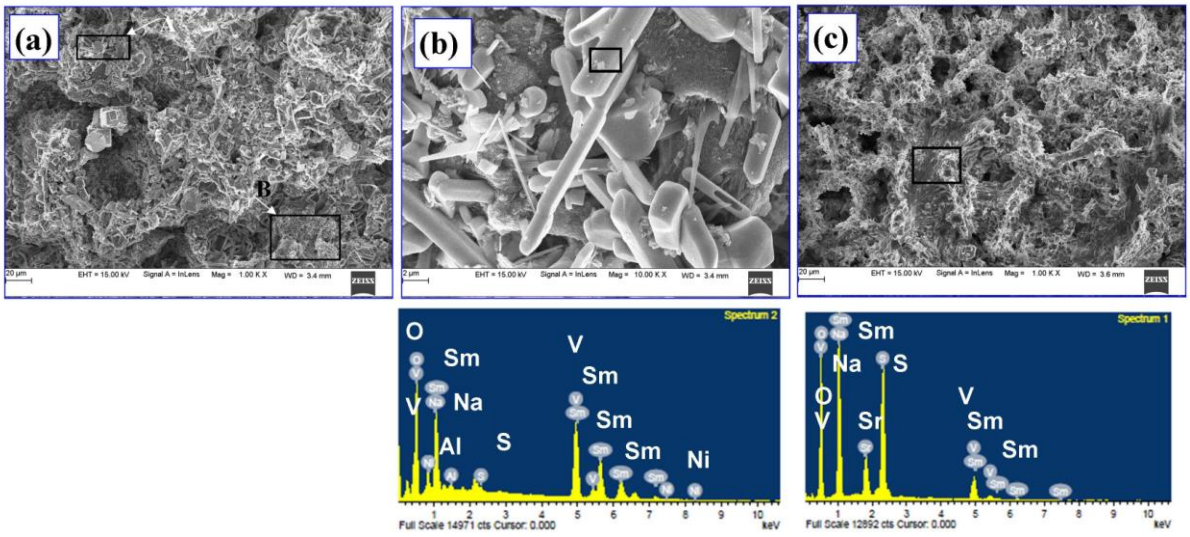

Fig. 6.4: SEM surface morphology of SSA TBCs after exposure to hot corrosion in 50 wt.% Na_2SO_4 + 50 wt.% V_2O_5 environment at 700 ˚C. The higher magnification images of selected region of A and B in (a) are shown in (b), and (c) respectively. Note: EDS maps of selected regions in 6.4 (b) and (c) are also shown here.

Table 6.1: EDS compositions of SSA TBCs after exposure to hot corrosion in 50 wt.% Na_2SO_4 + 50 wt.% V_2O_5 atmosphere at 700 ˚C (at.%).

Fig. 6.4	Sm	V	Sr	Na	O	S	Al	Ni	Cr
(b)	15.25	16.31	0.00	0.00	68.44	0.00	0.00	0.00	0.00
(c)	0.00	6.86	3.16	15.28	66.14	8.56	0.00	0.00	0.00

Surface morphology of SSA TBCs after exposure to hot corrosion in 50 wt.% Na_2SO_4 + 50 wt.% V_2O_5 atmosphere at 900 ˚C is shown in Fig. 6.5 (a and b). Fig. 6.5 (b) at higher magnification of Fig. 6.5 (a) is shown an interesting features, containing

a large quantity of nano sized rods on the coating surface after hot corrosion test [Fig. 6.5 (b)]. EDS analysis was demonstrated on the selected area of Fig. 6.5 (b) and chemical compositions values are given in Table 6.2. It evidenced the presence of only Sm, V and O which further confirmed the formation of $SmVO_4$ phase at higher temperature of 900 ˚C.

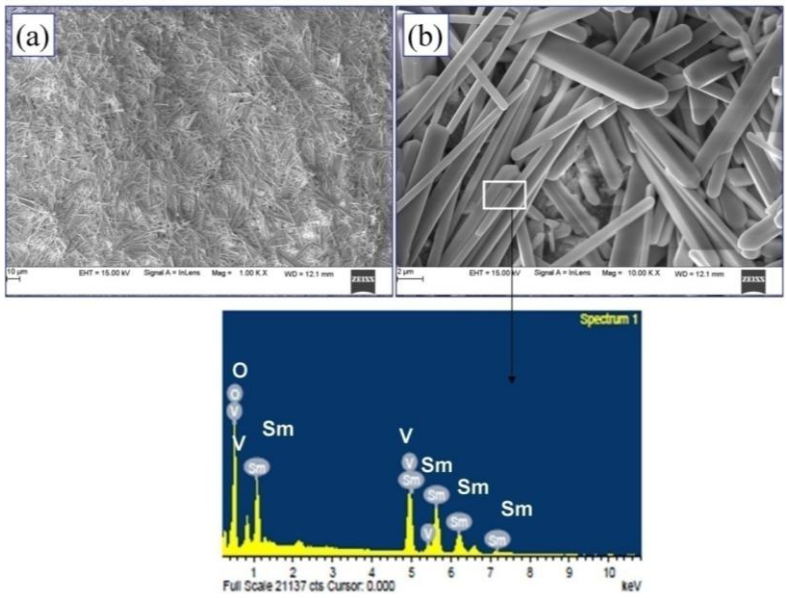

Fig. 6.5: SEM surface morphology of SSA TBCs (a) lower magnification; and (b) higher magnification of (a) after exposure to hot corrosion in 50 wt.% Na_2SO_4 + 50 wt.% V_2O_5 atmosphere at 900 ˚C. Note: EDS analysis was done in selected region of (b) and the result is shown here.

Table 6.2: EDS compositions of SSA TBCs after exposure to hot corrosion in 50 wt.% Na_2SO_4 + 50 wt.% V_2O_5 atmosphere at 900 ˚C (at.%).

Fig. #	Sm	V	Sr	Na	O	S	Al	Ni	Cr
Fig. 6.5 (b)	15.06	16.89	0.00	0.00	68.05	0.00	0.00	0.00	0.00

The possible chemical reaction can be proposed due to reactions between the top coat ceramic and high vanadates molten salt at higher temperature as follows:

Na_2SO_4 (l) $+V_2O_5$ (l) $\rightarrow 2NaVO_3$ (l) + SO_3 (g) (6.1)

$Sm_2SrAl_2O_7$ (s) $\rightarrow SmAlO_3$ (s) + SrO (s) (6.2)

Sm_2O_3 (s) + $2NaVO_3$ (l) $\rightarrow 2SmVO_4$ (s) + Na_2O (l) (6.3)

SrO (s) + $2NaVO_3$ (l) $\rightarrow SrV_2O_6$ (s) + Na_2O (l) (6.4)

According to the literature, the dissociation reaction of Na_2SO_4 liberated a higher amount of SO_3 gas to form Na_2O liquid at elevated temperature and this liquid tends to react with available molten V_2O_5 to form $NaVO_3$ according to Eq. 1 (Habibi et al. 2014). The hot corrosion mechanisms of SSA ceramic with $NaVO_3$ can be explained with the help of phase diagrams. However, due to the unavailability of literatures on phase equilibria of $Sm_2SrAl_2O_7$ - $NaVO_3$, the compound SSA can be assumed as the combination of Sm_2O_3, SrO and Al_2O_3 at a molar ratio of 1:1:1. So, the mechanisms can be explained in present study by the chemical reactions between Sm_2O_3-V_2O_5 and SrO-V_2O_5 binary phase diagrams (Zhu et al. 2011 and Ropp 2013). The presence of hot corrosion product $SmVO_4$ is observed in both 700 and 900 ˚C temperatures due to its thermal stability up to 1440 ˚C. But it is interesting to note that SrV_2O_6 phase was completely vanished at higher temperature of 900 ˚C due to complete melting at 778 ˚C. The hot corrosion mechanisms of SSA TBCs in molten salt could be also explained by Lewis-acid base theory. As per this mechanism the acid vanadium compounds readily react with ceramic top coats due to higher basicity. It is well known that the higher ionic radius, the stronger is the basicity (Xu et al. 2010). In this study Sr^{2+} has (132 pm) larger ionic radius than Sm^{3+} (96 pm) and Al^{3+} (68 pm). So the basicity of SrO is much higher as compared to Sm_2O_3 and Al_2O_3, which indicates SrO has higher tendency followed by Sm_2O_3 to react with molten $NaVO_3$ at 700 ˚C (Eq. 6.3 and 6.4). The presence of $AlVO_4$ has not been detected in XRD patterns due to its lesser reactivity with vanadates salt.

Fig. 6.6 shows the surface morphology of SSA TBCs after delamination of some portion of top ceramic top coat after exposure to hot corrosion in 50 wt.% Na_2SO_4 + 50 wt.% V_2O_5 atmosphere at 900 ˚C. The higher magnification image of Fig. 6.6 (a) is shown in Fig. 6.6 (b), which clearly revealed the porous TBC layer and hot corrosion products [Fig. 6.6 (c)].

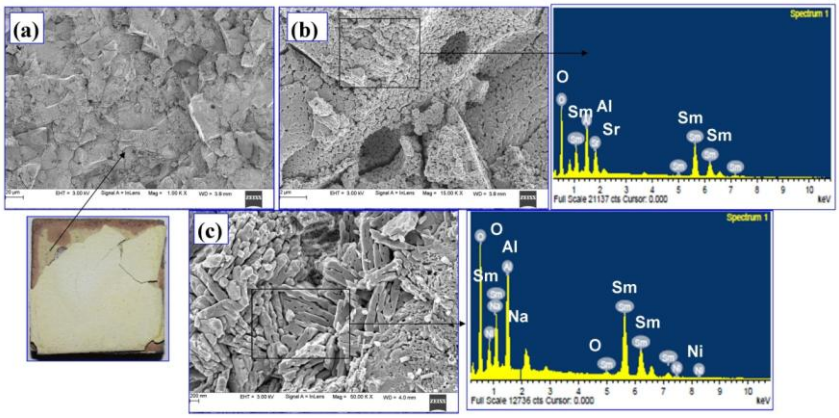

Fig. 6.6: SEM surface morphology of ceramic top coat after delamination of corroded layer (a) at lower magnification; and (b and c) high magnification images of (a) after exposure to 50 wt.% Na_2SO_4 + 50 wt.% V_2O_5 atmosphere at 900 ˚C. Note: EDS results of selected regions in (b) and (c) are also shown here.

The EDS analysis was performed on both porous TBC layer and corroded areas which are revealed that the presence of pure Sm, Sr, Al and O (atomic ratio of $Sm_2SrAl_2O_7$) and Sm, Al and O respectively is shown in Table 6.3. The considerable amounts of Ni and Cr were also observed and results are reported in Fig. 6.6 (c) and Table 6.3. It is may be due to the diffusion of bond coats elements at the bond coat and top coat interface after hot corrosion test in 50 wt.% Na_2SO_4 + 50 wt.% V_2O_5 atmosphere at 900 ˚C.

Table 6.3: EDS compositions of SSA TBCs after exposure to hot corrosion in 50 wt.% Na_2SO_4 + 50 wt.% V_2O_5 atmosphere at 900 ˚C (at.%).

Fig. #	Sm	V	Sr	Na	O	S	Al	Ni	Cr
Fig. 6.6 (b)	16.23	0.00	7.57	0.00	59.26	0.00	17.01	0.00	0.00
Fig. 6.6 (c)	16.80	0.00	0.00	0.00	50.13	0.00	17.83	9.27	6.01

6.3 Characterization of YSZ TBCs specimens after hot corrosion in 50 wt.% Na_2SO_4 + 50 wt.% V_2O_5 environment at 700 and 900˚C

The XRD analysis was demonstrated on YSZ TBCs before and after exposure to hot corrosion environment (50 wt. % Na_2SO_4 + 50 wt. % V_2O_5) is shown in Fig. 6.7 (a-c). All the XRD peaks in Fig. 6.7 (a) were indexed to t-ZrO_2 before exposed to hot corrosion.

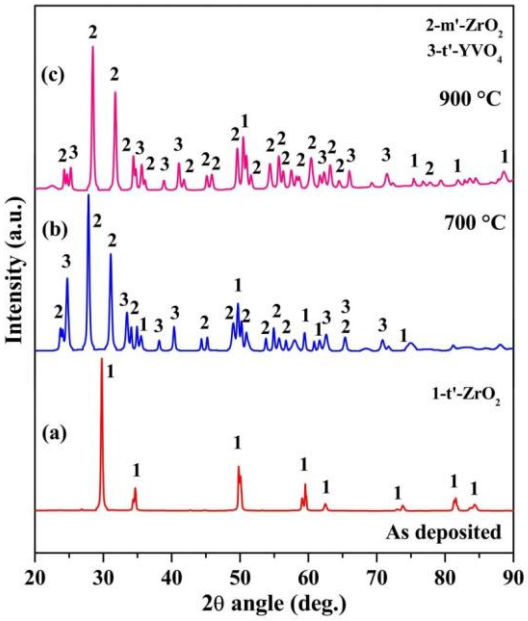

Fig. 6.7: XRD pattern of YSZ TBCs; (a) as deposited; (b) and (c) after exposure to hot corrosion in vanadates environment at 700 and 900 ˚C, respectively.

After YSZ TBCs exposed to high vanadate environment at 700 ˚C, the t-ZrO_2 peaks completely disappeared to form m-ZrO_2 due to the leaching of Y_2O_3 from YSZ. The new peak YVO_4 was also observed in the XRD pattern due to the chemical reaction between Y_2O_3 and vanadate molten salt. As the temperature increased from 700 to 900 ˚C, the intensity of m-ZrO_2 phase increased remarkably (4 times higher than 700 ˚C) due to excess leaching of Y_2O_3 stabilizer (Xu et al. 2010). This degradation behavior of YSZ top coat by $NaVO_3$ can be explained by

$$Y_2O_3\ (t\text{-}ZrO_2)\ (s) + NaVO_3\ (l) \rightarrow YVO_4\ (s) + m\text{-}ZrO_2\ (s) + Na_2O\ (l) \qquad (6.5)$$

It is well documented that zirconium meta-vanadate (ZrV_2O_7) compound is exist in the ZrO-V_2O_5 system and further it is destabilized into ZrO and V_2O_5 at a temperature of 750 ˚C (Mohan et al. 2007). However, it is interesting note that there is no reaction product of ZrO and V_2O_5 are observed in 50 wt. % Na_2SO_4 + 50 wt. % V_2O_5 atmosphere at 700 ˚C.

Typical surface morphology (SEM image) and respective EDS analysis of YSZ TBCs after exposure to hot corrosion in 50 wt. % Na_2SO_4 + 50 wt. % V_2O_5 environment at 700 ˚C are presented in Fig. 6.8 (a-d). The top surface of YSZ TBCs is

completely covered with new needle like crystals [Fig. 6.8 (b)]. This hot corrosion product was formed due to the interaction between Y_2O_3 and vanadates molten salt at 700 ˚C (Mohan et al. 2007).

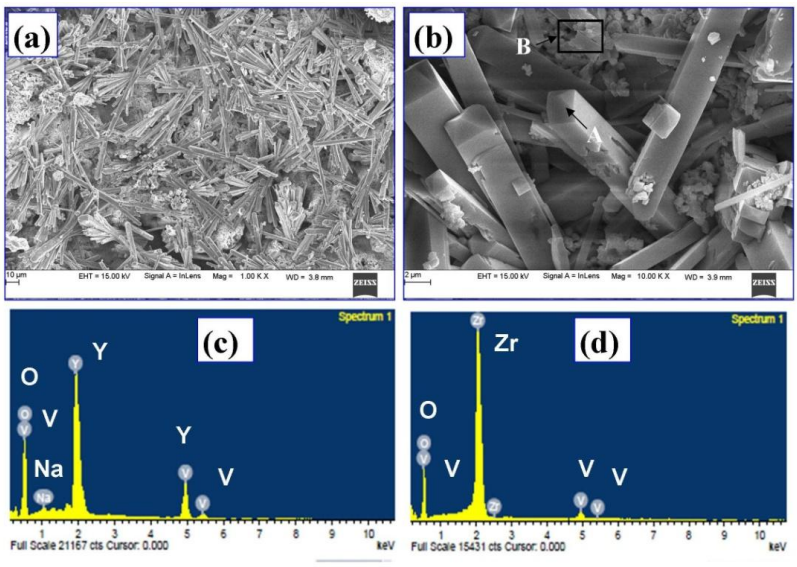

Fig. 6.8: SEM surface morphology of (a) YSZ TBCs; and (b) high magnification image of (a) after exposure to hot corrosion in 50 wt. % Na_2SO_4 + 50 wt. % V_2O_5 environment at 700 ˚C. Note: EDS analysis of image (b) at selected regions (A and B) is shown in 6.8 (c and d) respectively.

EDS analysis was performed to confirm the chemical compositions and it is composed of Y, V and O. Similarly, XRD analysis also confirmed the combination of Y, V and O corresponded to YVO_4 after hot corrosion test at 700 ˚C. The selected region B in Fig. 6.8 (b) revealed the composition of Zr and O in EDS analysis which corresponded to m-ZrO_2 (Table 6.4) (Afrasiabi et al. 2008).

Table 6.4: EDS compositions of YSZ TBCs after exposure to hot corrosion in 50 wt.% Na_2SO_4 + 50 wt.% V_2O_5 atmosphere at 700 ˚C (at.%).

Fig. 6.8 (b)	Y	V	Zr	Na	O
Region A	19.12	20.87	0.00	0.00	60.01
Region B	0.00	1.34	36.47	0.00	62.19

The surface morphology of YSZ TBCs exposed to hot corrosion at 900 ˚C is shown in Fig. 6.9 (a-b). The surface consisted of porous area and agglomerated lace-

like crystals (Batista et al. 2006). The EDS analysis was performed on these regions to identify the compositions and it is reported in Fig. 6.9 (c and d) and Table 6.5. The region A and B in Fig. 6.9 (a) majorly composed of Zr and O and Y, V and O respectively.

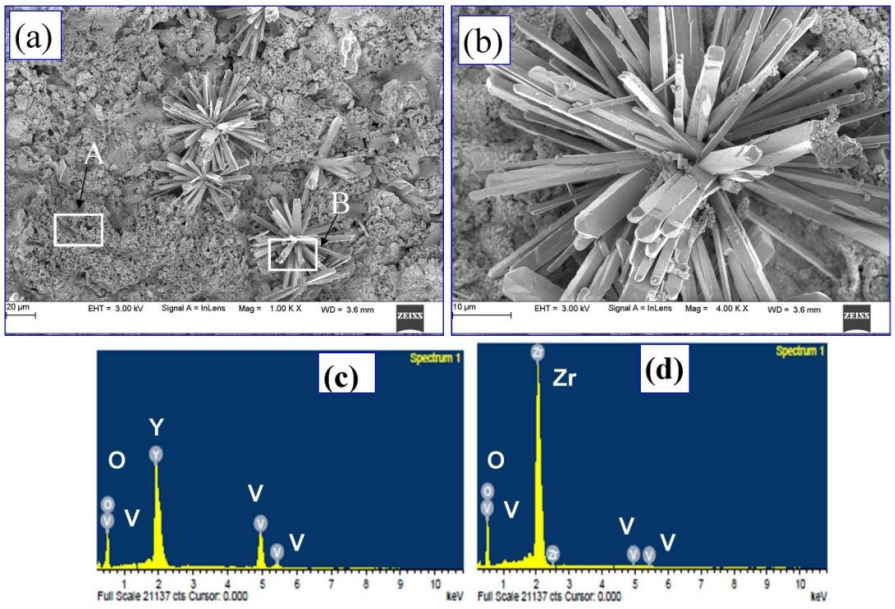

Fig. 6.9: SEM surface morphology of (a) YSZ TBCs; and (b) high magnification image of (a) after exposure to hot corrosion in 50 wt. % Na_2SO_4 + 50 wt. % V_2O_5 environment at 900 ˚C. Note: EDS analysis of image (a) at selected regions (A and B) is shown in 6.9 (c and d) respectively.

XRD results confirmed the formation of YVO_4 and m-ZrO_2. The failure of YSZ TBCs in 50 wt.% Na_2SO_4 + 50 wt.% V_2O_5 environment is mainly caused by losing Y_2O_3 from YSZ which caused t-ZrO_2 to m-ZrO_2 transformation. As a result this transformation further created 3-5% volume expansion, leading to cracks and spallation of TBCs (Ajay et al. 2015).

Table 6.5: EDS compositions of YSZ TBCs after exposure to hot corrosion in 50 wt.% Na_2SO_4 + 50 wt.% V_2O_5 atmosphere at 900 ˚C (at.%).

Fig. 5.11 (b)	Y	V	Zr	Na	O
Region A	19.05	21.75	0.00	0.00	59.20
Region B	0.00	1.34	33.50	0.00	65.16

6.4 Characterization of SSA and YSZ specimens after hot corrosion in 90 wt.% Na_2SO_4 + 5 wt.% V_2O_5 + 5 wt.% NaCl atmosphere at 700 and 900 ˚C

The XRD pattern of SSA and YSZ TBCs after exposure to hot corrosion in low vanadate environment at 700 and 900 ˚C are shown in Fig. 6.10 and 6.11 respectively.

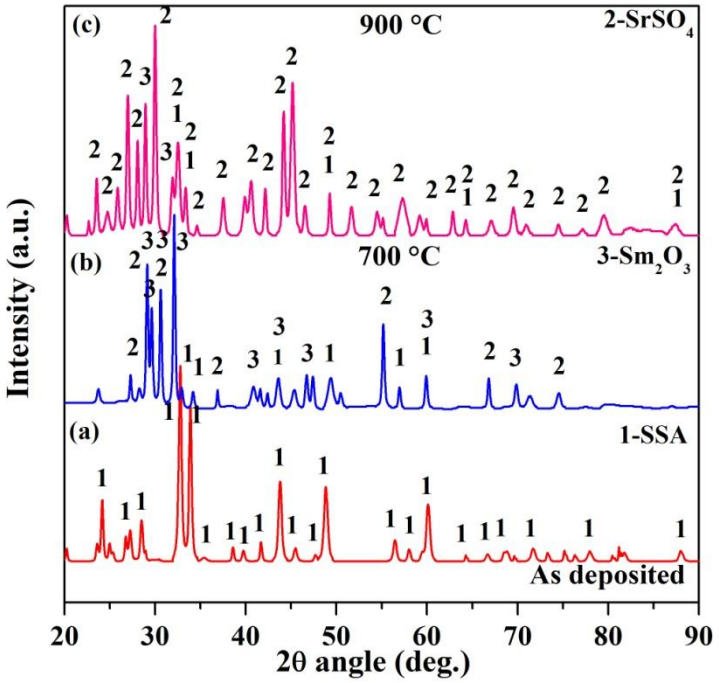

Fig. 6.10: XRD pattern of SSA TBCs; (a) as deposited; (b) and (c) after exposure to hot corrosion in 90 wt.% Na_2SO_4 + 5 wt.% V_2O_5 + 5 wt.% NaCl at 700 and 900 ˚C, respectively.

In the as deposited SSA TBCs showed the presence of single phase BCT structure, while YSZ TBCs showed the presence of t-ZrO_2 phase. After exposure to hot corrosion testing, the SSA TBCs exhibited the presence of new phases such as $SrSO_4$ (in both the temperature of 700 and 900 ˚C) and Sm_2O_3 due to the chemical reaction with 90% Na_2SO_4 molten salt. However, YSZ TBCs is revealed the presence of $Zr(SO_4)_2$ phase at 900 ˚C, apart from YVO_4 and m-ZrO_2 phases. The surface morphologies of SSA and YSZ TBCs after hot corrosion in chloride environment at 700 ˚C are represented in Fig. 6.12. SSA TBCs revealed the presence of several rod shaped crystals as compared to YSZ TBCs. EDS analysis was carried out on the

selected areas of Fig. 6.12 (b and d) and found that mostly composed of Sr, S and O (Table 6.6) and Y, V and O (Table 6.7) respectively. In addition, a traceable amount of Cr, Al, and Cl were also observed. These observations seen in combinations with XRD results which suggested that the rod shaped crystals in SSA and YSZ TBCs corresponded to $SrSO_4$ and YVO_4 respectively. The chemical reaction between SrO and Na_2SO_4 can be expressed as

$$SrO\ (s) + Na_2SO_4\ (s) \rightarrow SrSO_4\ (s) + Na_2O\ (l) \qquad (6.6)$$

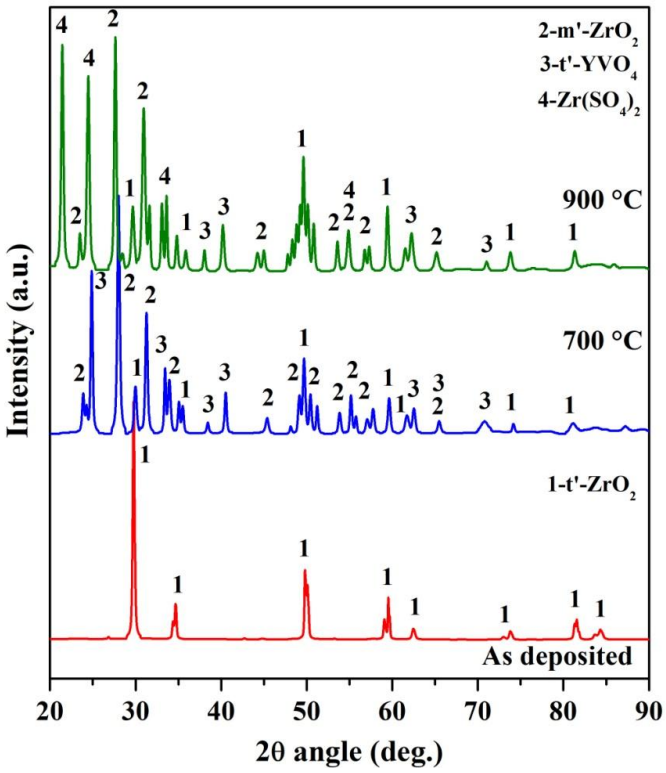

Fig. 6.11: XRD pattern of YSZ TBCs; (a) as deposited; (b) and (c) after exposure to hot corrosion in 90 wt.% Na_2SO_4 + 5 wt.% V_2O_5 + 5 wt.% NaCl at 700 and 900 ˚C, respectively.

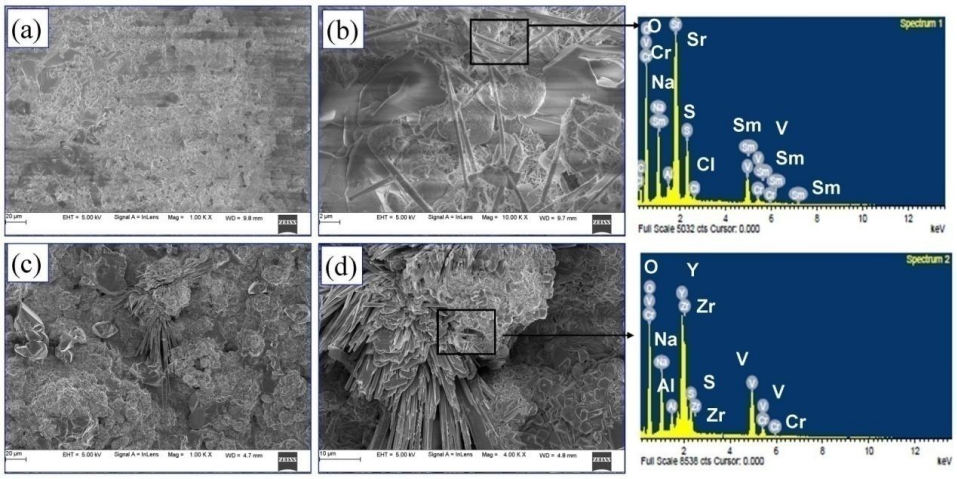

Fig. 6.12: SEM surface morphology of (a and b) SSA; and (c and d) YSZ TBCs after exposure to hot corrosion in 90 wt.% Na_2SO_4 + 5 wt.% V_2O_5 + 5 wt.% NaCl environment at 700 ˚C.

Table 6.6: EDS compositions of SSA TBCs after exposure to hot corrosion in chlorides atmosphere at 700 ˚C (at.%).

Region	Sm	V	Sr	Na	O	S	Cl	Al	Cr
Fig. 6.12 (b)	1.33	5.43	7.56	5.49	72.74	6.51	0.33	0.84	0.31

Table 6.7: EDS compositions of YSZ TBCs after exposure to hot corrosion in chlorides atmosphere at 700 ˚C (at.%).

Region	Y	V	Zr	Na	O	S	Cl	Al	Cr
Fig. 6.12 (d)	12.69	11.58	17.53	6.05	48.91	2.33	0.00	0.66	0.25

Surface morphologies of SSA and YSZ TBCs after hot corrosion testing in chloride environment at 900 ˚C are presented in Fig. 6.13. It is interestingly observed that a rigorous degradation of SSA and YSZ TBCs. Porous layers and rods like structures were also observed on the surface of YSZ TBCs. Further, an EDS analysis was performed on the selected areas in Fig. 6.13 (b) and (d) and results are reported in Tables 6.8 and 6.9.

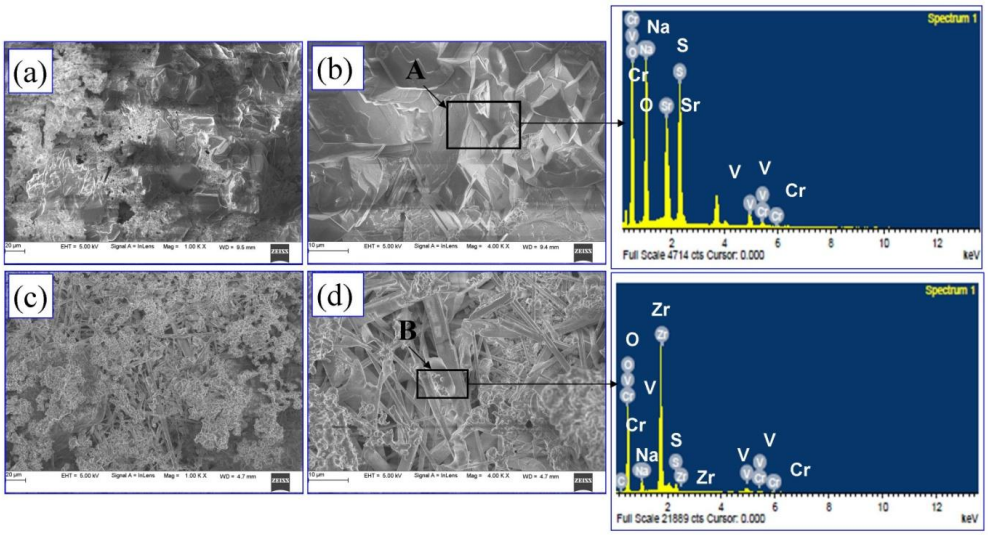

Fig. 6.13: SEM surface morphology of (a and b) SSA; and (c and d) YSZ TBCs after exposure to hot corrosion in chlorides environment at 900 ˚C. (Note: EDS analysis is performed at selected regions in 6.13 (b and d) and it is shown here).

The selected region in Fig. 6.13 (b) and 6.13 (d) consisted of mainly Sr, S and O and Zr, S and O respectively. Comparison to XRD pattern of SSA and YSZ TBCs after hot corrosion test in chlorides environment at 900 ˚C, the identified compositions corresponded to $SrSO_4$ and $Zr(SO_4)_2$ phases. The destabilized m-ZrO_2 reacted with highly enriched Na_2SO_4 at 900 ˚C to form $Zr(SO_4)_2$

$$m\text{-}ZrO_2\ (s) + 2Na_2SO_4\ (s) \rightarrow Zr(SO_4)_2\ (s) + 2Na_2O\ (l) \qquad (6.7)$$

Xu et al. (2010) have also found the formation of sulfates compounds of $La_2Zr_2O_7$ after exposure to 60 wt.% Na_2SO_4 + 40 wt.% V_2O_5 environment at 900 ˚C. The La_2O_3 leached out and reacted with Na_2SO_4 to form $La_2O_2SO_4$ and $La_2(SO_4)_3$ after exposure to 100 h of hot corrosion test.

Table 6.8: EDS compositions of SSA TBCs after exposure to hot corrosion in chlorides atmosphere at 900 ˚C (at. %).

Region	V	Sr	Na	O	S	Cr
Fig. 6.13 (b)	2.29	7.12	16.55	65.62	8.24	0.18

Table 6.9: EDS compositions of YSZ TBCs after exposure to hot corrosion in chlorides atmosphere at 900 ˚C (at. %).

Region	V	Zr	Na	O	S	Cr
Fig. 6.13 (d)	1.38	7.10	7.43	69.69	14.17	0.23

Fig. 6.14 shows the cross sectional SEM images coatings after hot corrosion testing in 50 wt.% Na_2SO_4 + 50 wt.% V_2O_5 (a) SSA; (b) YSZ TBCs; and (c) SSA and (d) YSZ TBCs in 90 wt.% Na_2SO_4 + 5 wt.% V_2O_5 + 5 wt.% NaCl at 900 ˚C. It is expected that the high vanadate environment (50 wt. % V_2O_5) should lead more degradation of coatings than chlorides at 900 ˚C due to elemental leaching from original phase to form vanadates. But from the cross sectional microstructure, it is observed that chlorides caused severe coating degradation in both TBCs than vanadates in the bond coat and top coat interface at 900 ˚C.

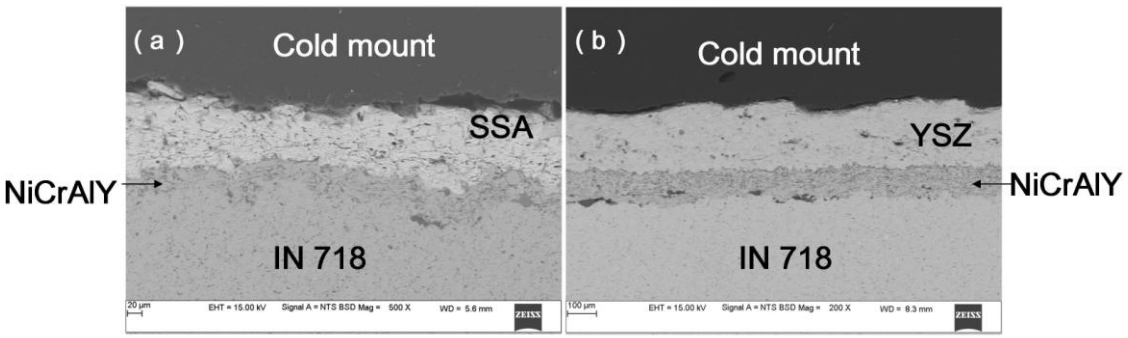

Fig. 6.14: Cross sectional SEM images of failed coatings of (a) SSA; and (b) YSZ TBCs after hot corrosion testing in 50 wt.% Na_2SO_4 + 50 wt.% V_2O_5 at 900 ˚C.

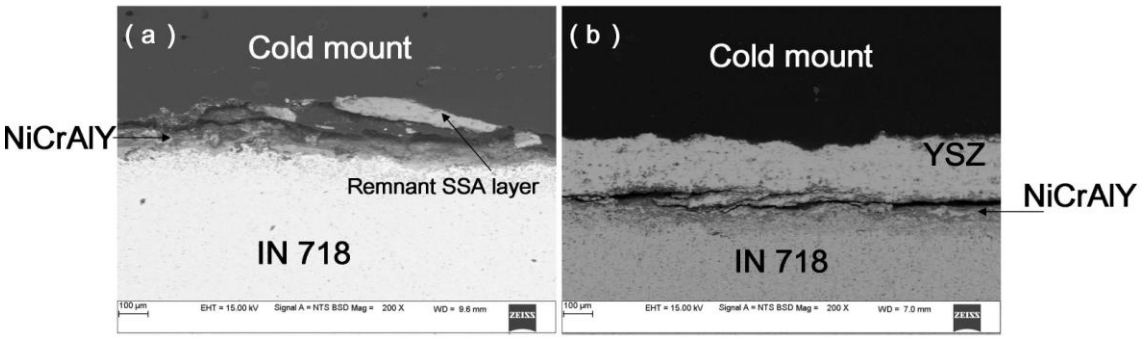

Fig. 6.15: Cross sectional SEM images of failed coatings of (a) SSA; and (b) YSZ TBCs after hot corrosion testing in 90 wt.% Na_2SO_4 + 5 wt.% V_2O_5 + 5 wt.% NaCl at 900 ˚C.

It is mainly due to the volatile nature of chlorides which can easily penetrate into defects of ceramic top coat and results the formation of more volatile corrosion products (chloride salt of metals) at the interface. The leaching of ion has significantly low influence as compared to attack by chloride ions at the bond coat-top coat interface in the presence of chloride environments at 900 ˚C. In contradictory, this leaching of ions has lesser impact than chloride ion attack at the bond coat-top coat interface in the chloride environments.

6.5 Role of combined inhibitors (MgO and NiO) on SSA TBCs in 50 wt.% Na_2SO_4 + 50 wt.% V_2O_5 at 900 ˚C

It has been reported literature that the hot corrosion effect of vanadate can be reduced using of chemical additives (inhibitors) such as MgO and NiO by forming stable vanadates such $Mg_3V_2O_8$ and $Ni_3V_2O_8$ respectively at elevated temperature. In this present study the failure time of SSA TBCs was significantly improved with the addition of MgO and NiO in 50 wt. % Na_2SO_4 + 50 wt. % V_2O_5 at 900 ˚C.

Fig. 6.16 (a) shows the time to failure of SSA TBCs after exposure to vanadate environment with and without inhibitor at 900 ˚C.

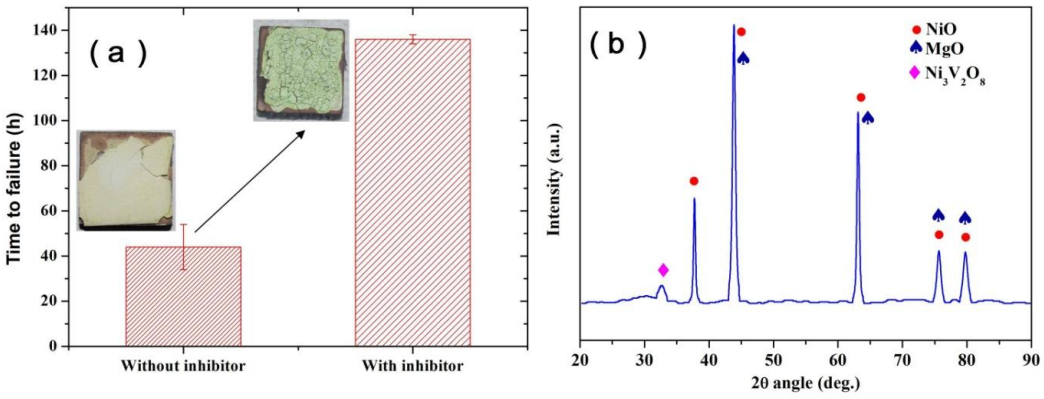

Fig. 6.16: (a) Time to failure of SSA TBCs with and without inhibitor in 50 wt.% Na_2SO_4 + 50 wt.% V_2O_5 at 900 ˚C and (b) XRD pattern of exposed SSA TBCs specimens in the presence of inhibitor in vanadate atmosphere at 900 ˚C.

Results revealed that the initial spallation of specimens was observed after 120 h of hot corrosion testing. The spallation of SSA TBCs improved three times higher than without inhibitor at 900 ˚C. The XRD analysis was undertaken on exposed SSA

TBCs specimens to know the phases present at the surface. The obtained results are reported in Fig. 6.16 (b) indicated that the presence of $Ni_3V_2O_8$ phase at 31.5˚ diffraction angle along with MgO and NiO phases. The SEM surface analysis was also conducted on exposed SSA TBCs specimens to see the severity of coating degradations in the presence of MgO and NiO inhibitors in high vanadate environments at 900 ˚C [Fig. 6.17)].

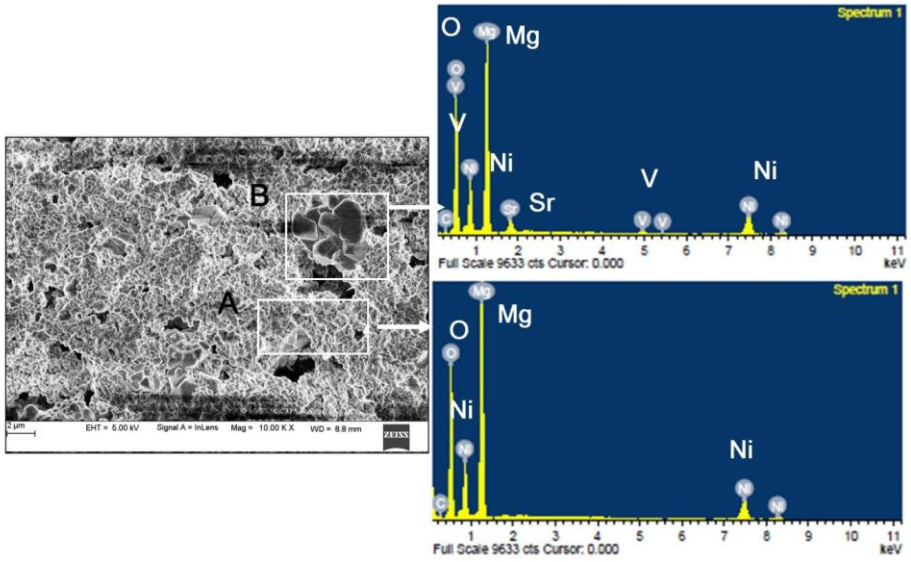

Fig. 6.17: SEM surface morphology of SSA TBCs exposed to hot corrosion test in 50 wt.% Na_2SO_4 + 50 wt.% V_2O_5 environment with MgO and NiO inhibitors at 900 ˚C.

It also revealed that surface consists of several pores and club shaped crystals. EDS analysis was performed on the selected regions composed of Mg, Ni and O (region A) and Mg, Ni, V and O (region B). These results are viewed in comparison with XRD results suggested that club shaped crystals made of $Ni_3V_2O_8$ (Rocca et al. 2003). The chemical reaction between vanadate and NiO on SSA TBCs samples can be expressed as

$$3NiO\ (s) + 2NaVO_3\ (l) \rightarrow Ni_3V_2O_8\ (s) + Na_2O\ (l) \qquad (6.8)$$

So it is understood that the vanadate attack on SSA TBCs can be significantly nullified with the help of combined inhibitors by forming stable $Ni_3V_2O_8$ phase at the SSA TBCs surface.

Summary of hot corrosion study

- SSA based TBCs degrades severely by hot corrosion in vanadates and chlorides environments at elevated temperatures.
- However, it shows better performance in the presence of combined inhibitors such as MgO + NiO.

CHAPTER 7

7 HIGH TEMPERATURE EROSION BEHAVIOR OF SSA AND YSZ TBCs

The erosion failure of turbine components mainly failed by the solid particle impingement has paid more attention in recent years. The particle velocity, impingement angle, particle properties and operating temperature play an important role on the erosion behavior of TBCs. Since, erosion failure mainly caused by the failure of ceramic top coat, some post heat treatment techniques such as pre-heat treatment and some surface modification process have also been conducted to improve the erosion resistance of TBCs (Janos et al. 1999 and Tsai et al. 2007). Hence, in the present study, pre-oxidation test was conducted on as deposited SSA and YSZ TBCs at 1050 ˚C for 10 h to enhance the microstructure integrity of ceramic top layer.

7.1 Macroscopic examination of pre-oxidized SSA and YSZ TBCs

The high temperature erosion study was conducted on SSA and YSZ TBCs at impingement angles of 30 and 90˚ for the temperatures of 200, 500 and 800 ˚C. The macroscopic images of pre-oxidized SSA and YSZ TBCs showing scar produced on the sample surface at different impact angles of 30 and 90˚ are represented in Fig. 7.1.

The profile of an erosion scars on the sample are look like an ellipse. The major and minor axis of the scars increased with an increasing test temperature of both TBCs at an impact angle of 30˚ (Fig. 7.1).

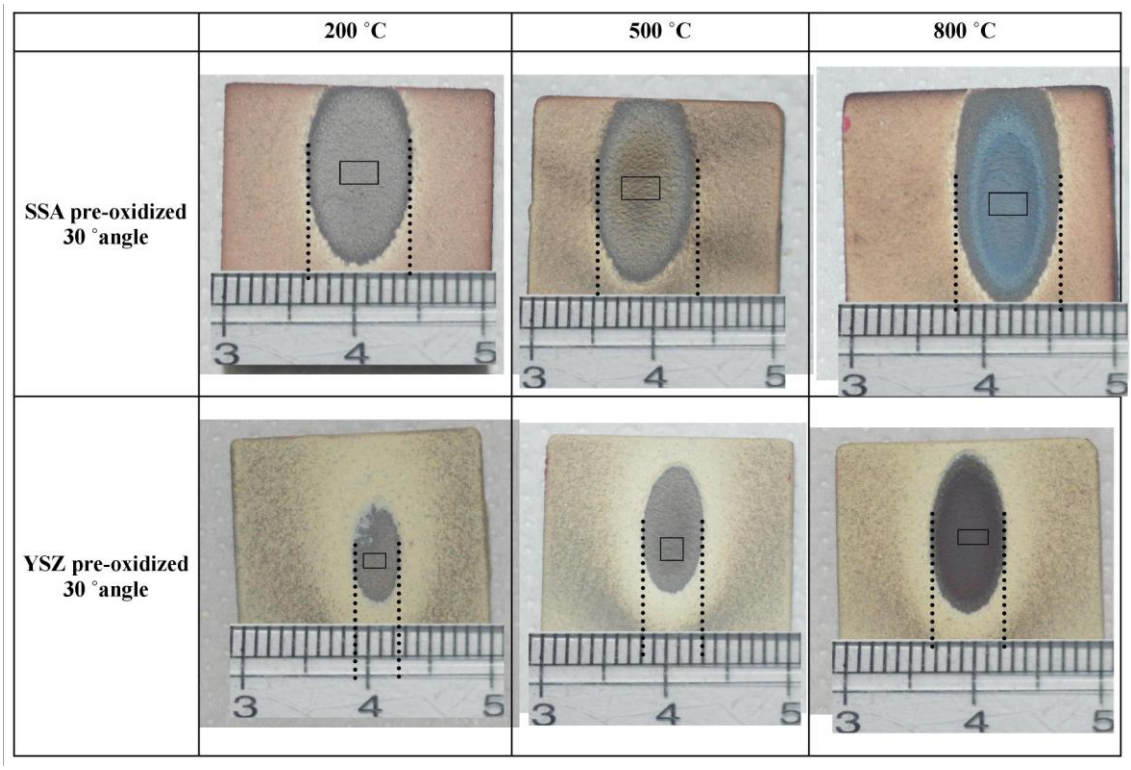

Fig. 7.1: Macroscopic images of pre-oxidized SSA and YSZ TBCs showing the erosion scar produced on the surface of TBCs specimens at an impact angle of 30˚ for different temperatures.

The length of major axis increased from 14, 15 to 17 mm for the temperatures of 200, 500 and 800 ˚C respectively for pre-oxidized SSA TBCs. There was no considerable variation in minor axis of eroded scars of SSA TBCs. The color of eroded area was changed from grey to ash grey with an increasing temperature from 200 to 800 ˚C. In the YSZ TBCs, the length of major axis of scars was found about 7, 10 and 12 mm for 200, 500 and 800 ˚C respectively. The length of minor axis was also varied from 4-7 mm for 200 and 800 ˚C respectively. Unlike SSA TBCs, the YSZ TBCs showed black region of eroded area after exposure to 800 ˚C.

The profile of eroded area was circular shape and it is varied from 6-7 and 7-8 mm for YSZ and SSA TBCs, respectively at 90˚ impact angle (Fig. 7.2). Considerably more depth could be seen in SSA than YSZ TBCs at a maximum temperature of 800 ˚C.

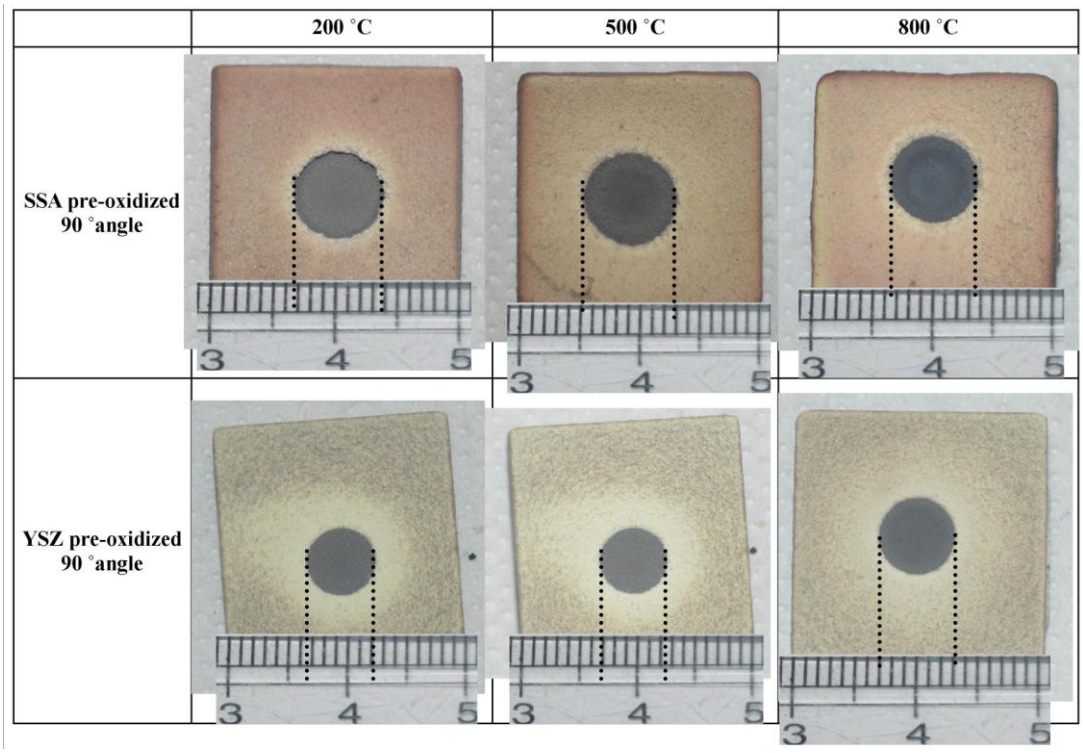

Fig. 7.2: Macroscopic images of pre-oxidized SSA and YSZ TBCs showing the erosion scar produced on the surface of TBCs specimens at an impact angle of 90˚ at different temperatures.

The erosion test was also conducted on as deposited SSA TBCs for the sake of comparison with pre-oxidized SSA TBCs (Fig. 7.3). Notably; an interesting observation was seen in the as deposited SSA TBCs at an angle of 30 and 90˚. The length of major and minor axis was measured about 11 and 6 mm respectively at 30˚ impact angle. At an angle of 90˚ impact the diameter of eroded scar was found about 7, 4 and 7 mm for 200, 500 and 800 ˚C respectively. The reduction in length of erosion scars at 500 ˚C may be due to better sintering as compared to 800 ˚C in both 30 and 90˚ impact angle.

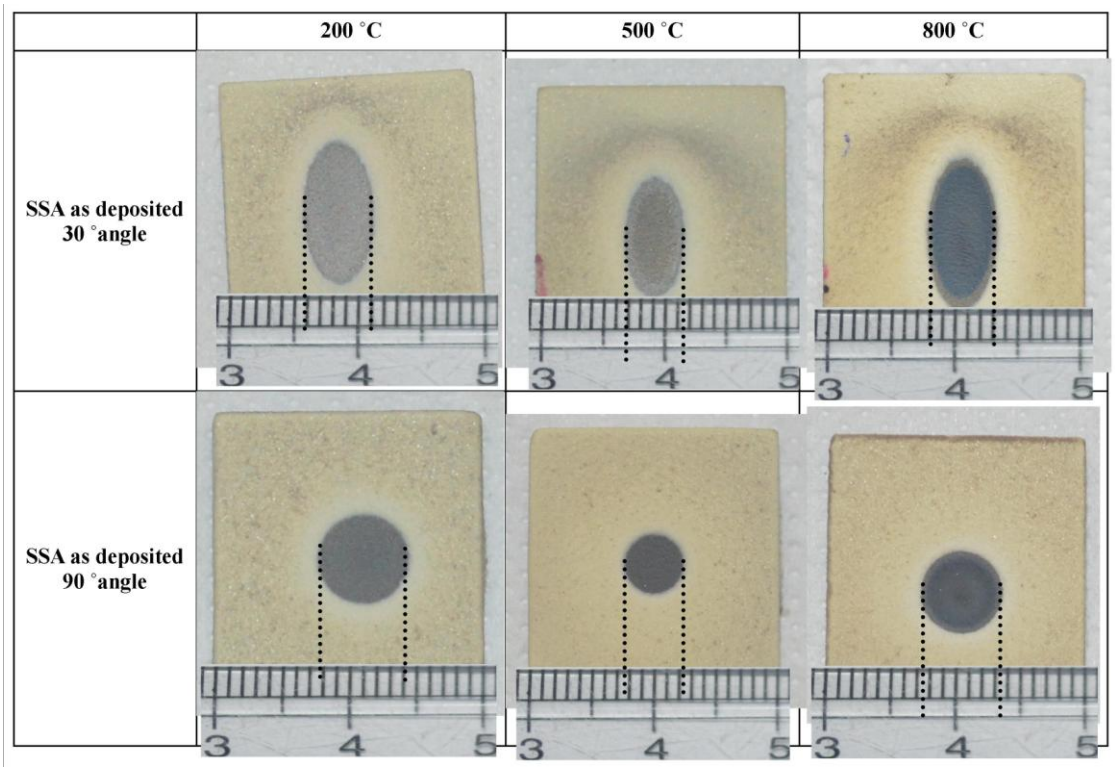

Fig. 7.3: Macroscopic images of as deposited SSA TBCs showing the erosion scar produced on the surface of TBCs specimens at an impact angle of 30 and 90˚ at different temperatures.

7.2 Erosion rate as a function of temperature

From Fig. 7.4 (a and b), it is observed that the pre-oxidized SSA TBCs exhibited 63, 30 and 32% more erosion rate than pre-oxidized YSZ TBCs at an angle of 30˚ impingement for 200, 500 and 800 ˚C respectively. At an angle of 90˚, SSA TBCs showed about 46, 15 and 57% higher than YSZ TBCs. The erosion loss of as deposited SSA TBCs showed 43% lower than pre-oxidized SSA TBCs at 30˚ impingement at 800 ˚C [Fig. 7.4 (a)]. In general, the erosion rate of ceramic top coat decreased with an increasing thermal aging temperature due to higher sintering effect. Janos et al. (1999) have reported the erosion resistance of plasma sprayed YSZ TBCs after thermal ageing at different temperatures. Results confirmed that relative improvement in erosion resistance was observed to be about 70 % after exposure to thermal ageing treatment at 1500 ˚C. The same thermal ageing treatment was performed on EB-PVD YSZ TBCs by Wellman et al. (2004) at two different

temperatures of 1100 and 1500 ˚C for 100 and 24 h respectively. The erosion results showed that both the heat treatment resulted significant increase in erosion rate as compared to as deposited samples mainly due to incomplete sintering YSZ columns. So based on these results it is clearly understood the top coat microstructure (splats and columns) play a significant role on the erosion resistance of TBCs at higher temperature. In the present study also pre-oxidized SSA TBCs showed considerable erosion loss as compared to as-deposited TBCs. The possible reason could be explained with the help of microstructure analysis which is shown in following sections.

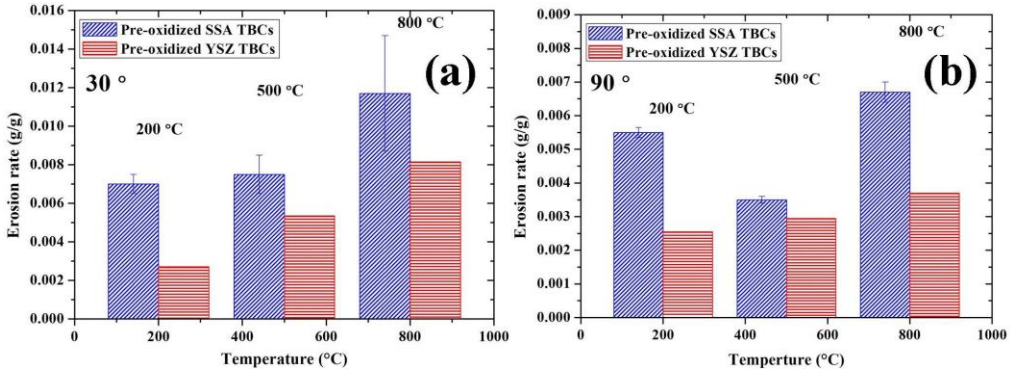

Fig. 7.4: Erosion rate of pre-oxidized (a) SSA and YSZ TBCs at an angle of 30˚; and (b) pre-oxidized SSA and YSZ TBCs at an angle of 90˚ for different testing temperatures.

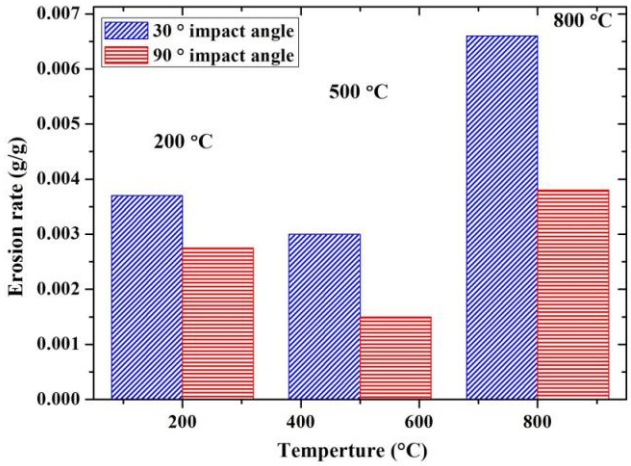

Fig. 7.5: Erosion rate of as-deposited SSA TBCs at an angle of 30˚; and (b) 90˚ angles for different testing temperatures.

7.3 Characterization of SSA and YSZ TBCs after erosion test

Fig. 7.6 shows the XRD patterns of (a) substrate (Inconel 718); (b) as deposited NiCrAlY; and erosion eroded area of pre-oxidized SSA TBCs for (c) 200; (d) 500 and (e) 800 ˚C at 30˚ angle. The substrate and as deposited NiCrAlY indicated the presence of only cubic γ'-Ni_3Al (JCPDS # 03-065-0712) peaks at diffraction angles of about 44 and 51˚. But the diffraction peaks of erosion tested SSA TBCs showed some slight peaks shift of diffraction peaks toward lower angle side. The diffraction peak values of SSA TBCs are reported in Table 7.1. It clearly revealed that the peak shift 43.56 to 42.8˚ and broadening of peaks (full width half maximum-FWHM) from 0.48 to 0.96 mainly due to the stresses generated by rapid heating and cooling of samples during erosion test. All the erosion tested SSA TBCs exhibited only the presence of γ'-Ni_3Al without any additional peaks indicating that complete removal of ceramic top coat and possibility of bond coat. The EDS analysis was also performed on the eroded surface of SSA TBCs and it's given in Table 7.2.

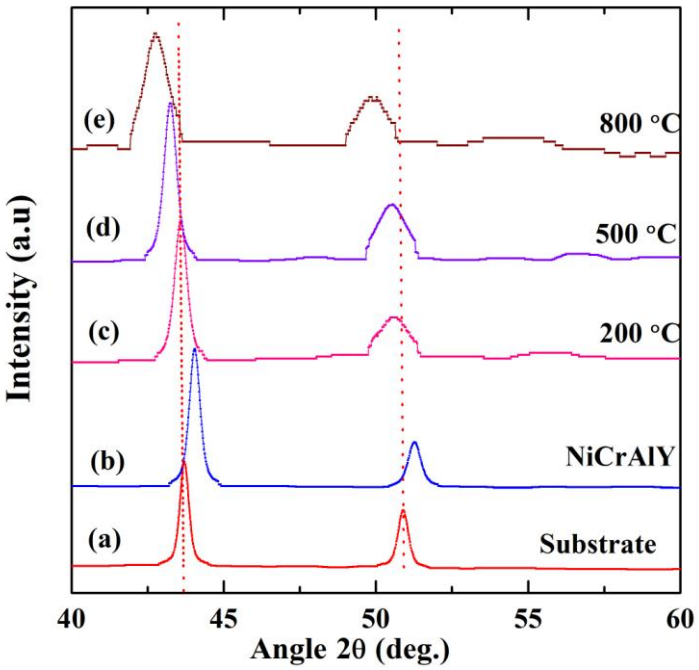

Fig. 7.6: XRD patterns of (a) substrate (Inconel 718); (b) as deposited NiCrAlY; and erosion tested pre-oxidized SSA TBCs at (c) 200; (d) 500 and (e) 800 ˚C at 30˚ angle. (Note: Patterns were taken on eroded areas of the sample).

Table 7.1: The peak position and FWHM values of erosion tested pre-oxidized SSA TBCs at 30˚ angle for different temperatures.

Temp.(˚C)	Position, 2θ (deg.)	FWHM, β (deg.)	Phases
200	43.56	0.4800	γ'-Ni_3Al
500	43.22	0.4800	γ'-Ni_3Al
800	42.81	0.9600	γ'-Ni_3Al

Table 7.2: EDS analysis of eroded areas of pre-oxidized SSA TBCs at an angle of 30˚ (at. %).

Temp.(˚C)	Ni	Cr	Al	Fe	Ti	O
200	22.52	10.25	18.09	4.97	0.41	43.83
500	18.50	7.83	17.92	7.74	0.50	47.51
800	5.73	3.65	26.03	4.51	0.51	59.57

The reduction in Ni and Cr percentage were found to be about 75 and 64 % respectively from 200 to 800 ˚C respectively. Similarly, an increasing percentage of Al (30%) and O (26%) were also observed with an increasing temperature up to 800 ˚C. Fig. 7.7 shows SEM image of pre-oxidized SSA TBCs after erosion test at 30˚ for 800 ˚C which is marked as point 1 and point 2.

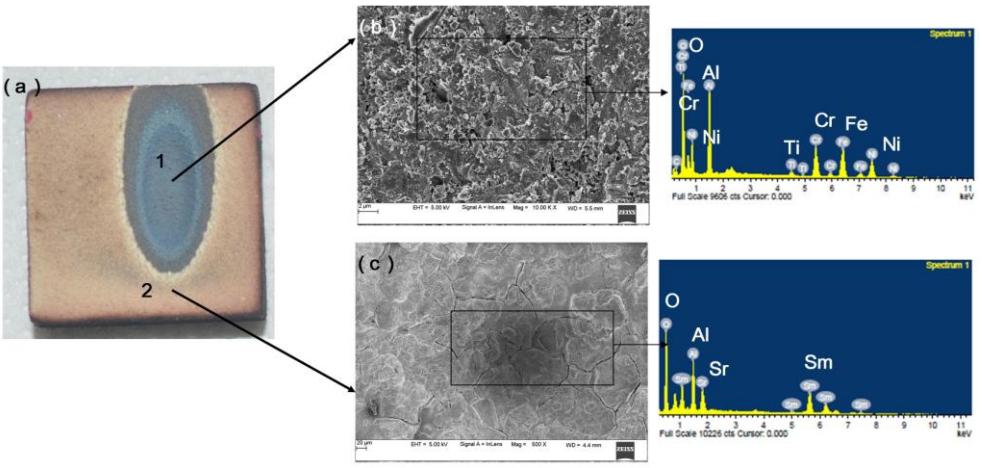

Fig. 7.7: Macroscopic image shows the pre-oxidized SSA TBCs after erosion testing at 30 ˚angle for 800 ˚C (a); higher magnification SEM images at selected region 1 (b); and region 2 (c). Note: EDS analysis of selected regions in (b) and (c) are also shown here.

A higher magnification SEM images at selected point 1 and 2 are presented in Fig. 7.7 (b) and 7.7 (c) respectively with their EDS maps. EDS analysis shows that the selected region in (b) mainly composed of Al, Ni, Cr, Fe, Ti and O and region 2 consists of Sm, Sr, Al and O (with 15.45 at.% Sm, 7.2 at.% Sr, 14.9 at.% Al and 62.67 at.% O). These observations confirmed that the stoichiometric ratio of pre-oxidized SSA remains same even after erosion testing at 800 ˚C (non-eroded area) but eroded area was completely composed of Ni, Cr, Al, Fe, Ti and O due to the loss of top ceramic coat. It is well proved that among all the elements in the NiCrAlY bond coat, aluminium has minimum thermodynamic activity required for the formation of its oxide at elevated temperature and P_{O2} = 1 atm (Gale et al. 2008). So, it can be concluded that aluminium is the preferred oxide to be formed on the eroded surface with an increasing temperature from 200 to 800 ˚C. Hence, the percentage of Ni and Cr got reduced due to an increasing percentage of Al and O. The presence of considerable percentage of Fe and Ti observed mainly due to diffusion from substrate to NiCrAlY bond coat after pre-oxidation test at 1050 ˚C for 10 h.

As similar to SSA TBCs, XRD pattern was done on eroded areas of pre-oxidized YSZ TBCs to examine the possible phase formation after erosion test at 30˚ angle for different temperature and it's reported in Fig. 7.8. Results showed that the presence of γ'-Ni_3Al peaks along with t'-ZrO_2 peaks around the diffraction angle of 60˚. As the testing temperature increases, intensity of peaks decreases and peak broadening increases due to increasing thermal stresses arises by sudden cooling of samples to room temperature (Table 7.3).

Table 7.3: The peak position and FWHM values of erosion tested pre-oxidized YSZ TBCs at 30˚ angle for different temperatures.

Temp.(˚C)	Position, 2θ (deg.)	FWHM, β (deg.)	Phases
200	43.51	0.3360	γ'-Ni_3Al
500	43.07	0.4800	γ'-Ni_3Al
800	43.06	1.1520	γ'-Ni_3Al

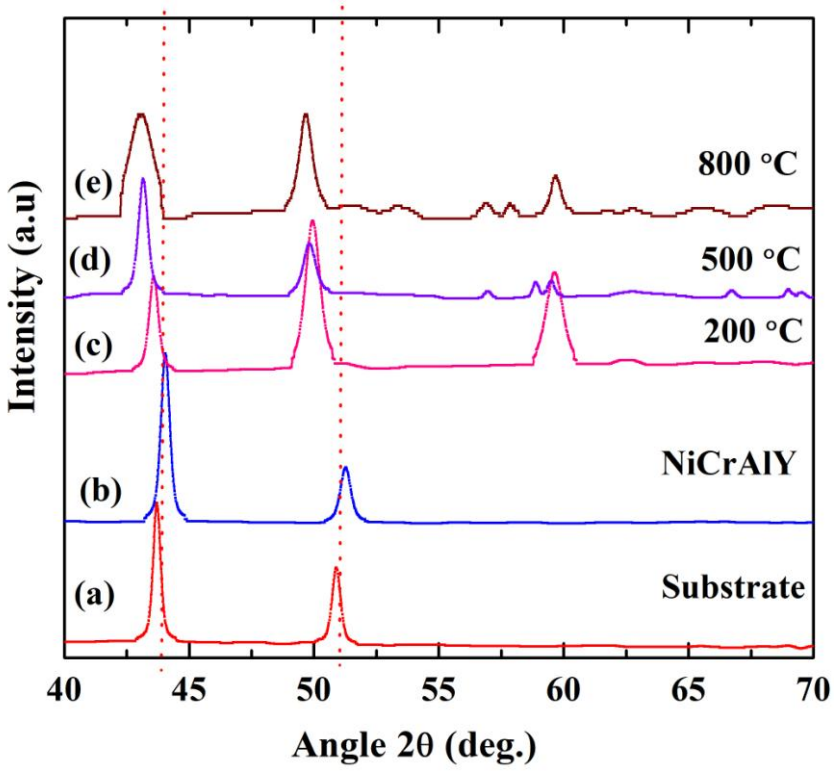

Fig. 7.8: XRD patterns of (a) substrate (Inconel 718); (b) as deposited NiCrAlY; and erosion tested pre-oxidized YSZ TBCs at (c) 200; (d) 500 and (e) 800 ˚C at 30˚ angle. Note: Patterns were taken on eroded areas of the sample.

EDS analysis was demonstrated on the eroded areas of YSZ TBCs and obtained results are shown in Table 7.4.

Table. 7.4: EDS analysis of eroded areas of pre-oxidized YSZ TBCs at an angle of 30˚ (at.%).

Temp.(˚C)	Zr	Ni	Cr	Al	Fe	Ti	O
200	5.75	18.05	6.86	15.07	0	0	54.27
500	0	14.92	6.52	19.71	6.72	0.53	51.60
800	0	16.68	6.80	16.27	6.80	0.36	53.11

The samples treated at 200 ˚C showed considerable percentage of Zr along with Ni, Cr, Al and O due to attached small debris of ceramic top coat. With an increasing temperature to 500 and 800 ˚C, severity of erosion increased and thereby, the

percentage of Zr completely vanished and only bond coat elements were observed. These observations clearly showed that mass loss of SSA and YSZ TBCs during erosion test not only caused by ceramic top coat but it is also by loss of bond coat.

The sintering behavior of ceramic top coat during pre-oxidation and erosion test could be explained with the help of SEM morphologies and mechanical characterizations in the following sections.

7.4 Eroded and non-eroded surface morphology of pre-oxidized SSA and YSZ TBCs

The eroded surface morphology of pre-oxidized SSA TBCs clearly indicated that under the impact of Al_2O_3 particles, more micro-cracks formed and propagated with an increasing testing from 200 to 800 ˚C than YSZ TBCs [Fig. 7.9 (a-c)]. Splats morphology decreased and most splats were found to be damaged into smaller particles. The larger area spallation was observed in the case of pre-oxidized SSA TBCs over pre-oxidized YSZ TBCs [Fig. 7.9 (d-e)]. The non-eroded SEM morphology of pre-oxidized SSA and YSZ TBCs after testing at different temperatures is represented in Fig. 7.10. Several mud cracks could be seen in the pre-oxidized SSA TBCs, while YSZ TBCs clearly revealed the surface free from any cracks and pores which indicated better sintering of ceramic top coat at 1050 ˚C for 10 h.

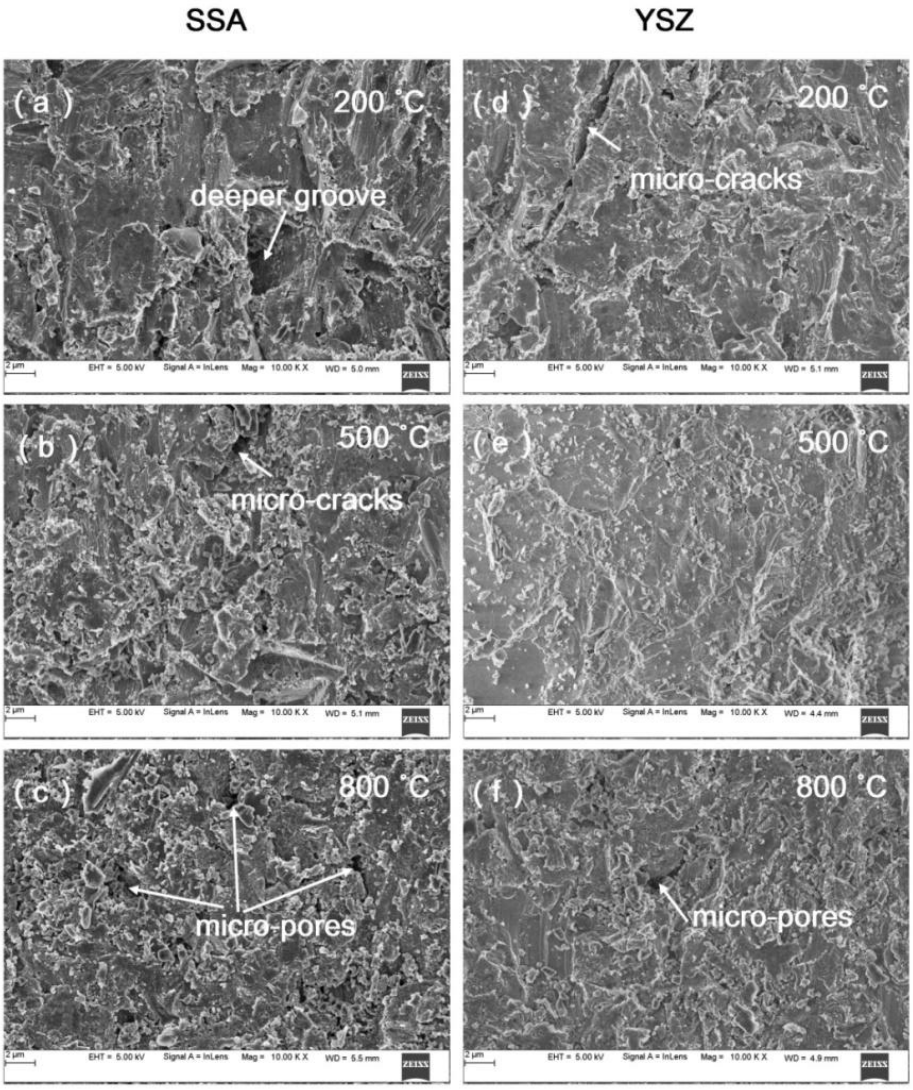

Fig. 7.9: SEM surface micrographs of showing eroded surface morphology of pre-oxidized SSA TBCs after tested at (a) 200; (b) 500; and (c) 800 ˚C and pre-oxidized YSZ TBCs after tested at (d) 200; (e) 500; and (f) 800 ˚C at an impingement angle of 30˚.

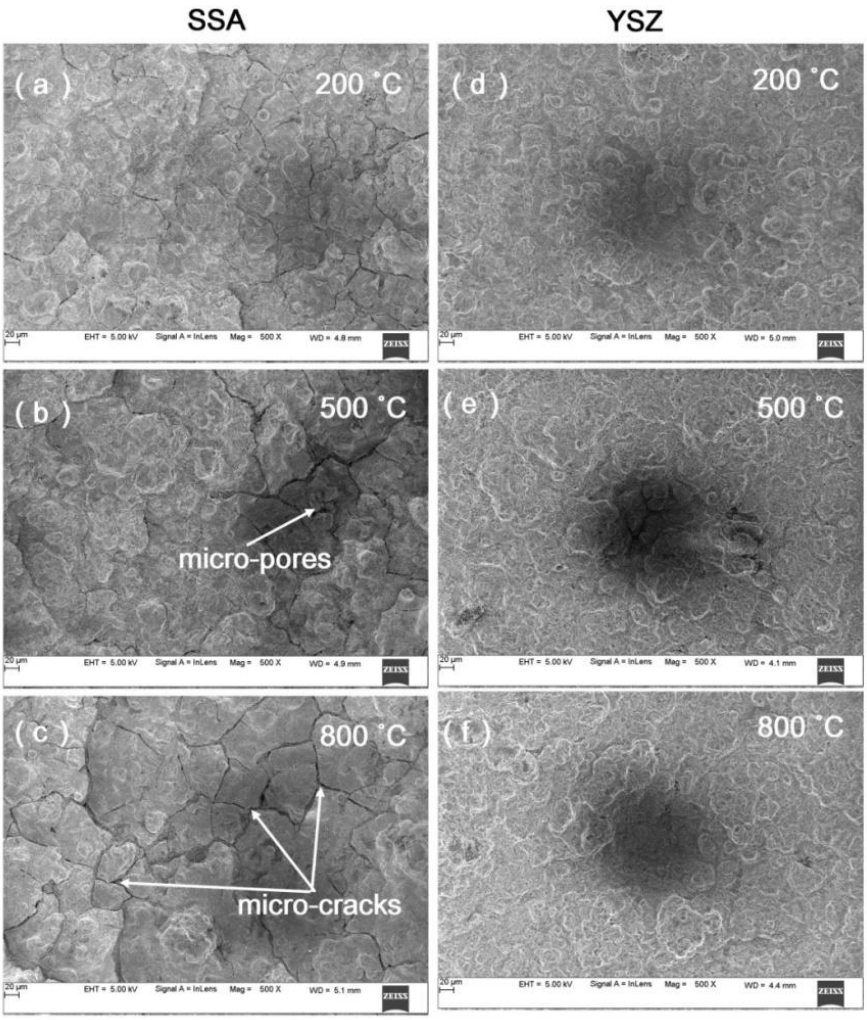

Fig. 7.10: SEM surface micrographs of un-eroded areas of pre-oxidized SSA TBCs showing several microcracks and pores in the surface after exposure to (a) 200; (b) 500; (c) 800 ˚C and pre-oxidized YSZ TBCs after exposure to (a) 200; (b) 500; (c) 800 ˚C.

The mechanical properties of as-deposited; pre-oxidized and after erosion of pre-oxidized specimens at 800 ˚C for SSA and YSZ TBCs were examined by nano-indentation technique and results are reported in Fig. 7.11 and Table 7.5. The load and depth of penetration was continuously measured on the sample surface of SSA and YSZ TBCs during loading and unloading condition. No significant changes in the Young's modulus of as deposited SSA and YSZ TBCs was observed. It may be due to better mechanical interlocking of splats boundaries in ceramic top coat microstructure. But after exposure to pre-oxidation treatment at 1050 ˚C, an increment of Young's

modulus was found about 35% which is mainly caused by sintering of ceramic topcoat of SSA TBCs. The percentage increase in Young's modulus of about 76% for pre-oxidized YSZ TBCs indicates the better sinterability of ceramic top coat than SSA TBCs.

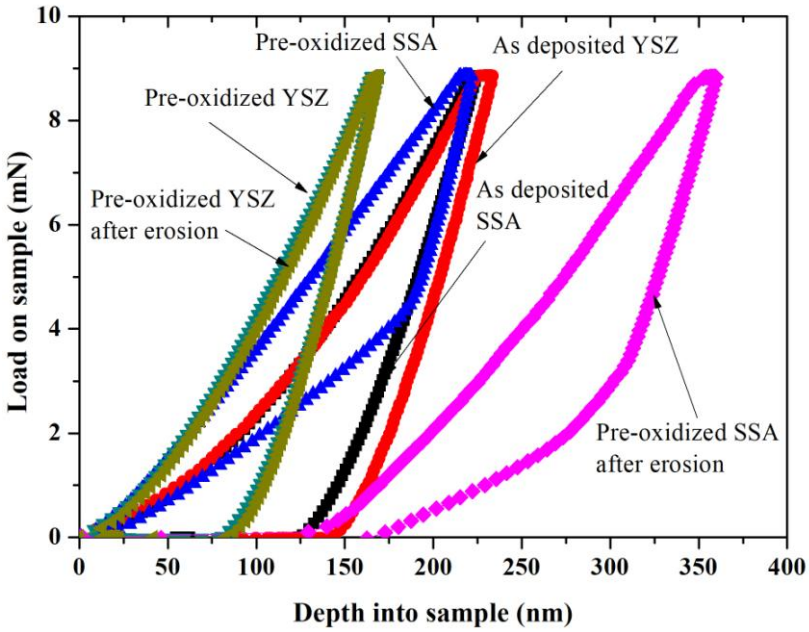

Fig. 7.11: Typical load-depth curves of as deposited and pre-oxidized SSA and YSZ TBCs before and after erosion test.

Table 7.5: Mechanical properties of as-deposited, pre-oxidized, and erosion tested SSA and YSZ TBCs.

Condition	Young's modulus, E (GPa)	Hardness, H (GPa)
As deposited SSA	131±10	11±1
As deposited YSZ	136±7	10±1
Pre-oxidized SSA	166±25	10±2
Pre-oxidized YSZ	239±20	20±5
Pre-oxidized SSA after erosion test at 800 ˚C	107±16	3±1.5
Pre-oxidized YSZ after erosion test at 800 ˚C	235±18	21±3

The Young's modulus (107 GPa) of pre-oxidized SSA TBCs were found about 2 times lower than Young's modulus (239 GPa) of YSZ TBCs after erosion test at 800 ˚C. The observed lower erosion resistance of SSA is due to the formation of mud-cracks during pre-oxidation treatment reduced the sintering process at 1050 ˚C for 10 h (Kumar et al. 2012). These results implies that any changes in the erosion rate was mainly due to microstructural changes as a result of sintering and mechanical properties such as Young's modulus and hardness of SSA and YSZ TBCs during pre-oxidation treatment. Shin et al. have studied the influence of microstructure on erosion resistance of plasma sprayed 7YSZ thermal barrier coatings under gas turbine operating conditions. The measured erosion rate increased with increasing porosity from 13 to 21 % for all the testing conditions such as temperature (980 ˚C), velocity (122, 231 and 305 m/s) and angle (20˚). The reduction in erosion rate was mainly due to the presence of larger volume of voids in porous plasma sprayed YSZ top coat decreased the cohesive strength of splats. As a result, chipping of splats layers occurred by continuous impact of solid particles at high temperature (Shin et al. 2018). The erosion behavior of plasma sprayed and EB-PVD YSZ TBCs were studied by Nicholls et al. (1999). It was concluded that EB-PVD TBCs showed more resistant (7-10 times) than air plasma sprayed TBCs at room temperature and 910 ˚C, when impacted with alumina particles due to poorly bonded splat boundaries. In EB-PVD coating the top coat ceramic is lost from the near surface region due to the presence of cracks within the columns under the normal impact. But in the case of APS TBCs, ceramic failure mainly occurred through crack networks of splats boundaries which are the characteristic features of plasma spray process. In the present study, the increase in erosion rate of pre-oxidized SSA over YSZ TBCs was mainly due to crack propagation along the splats region during pre-oxidation test at 1050 ˚C for 10 h and this resulted greater volume loss of ceramic per impact of Al_2O_3 particles.

Summary of high temperature erosion study

- The erosion rate of newly developed SSA TBCs exhibits better resistance at 90˚ as compared to 30˚ impact angle at elevated temperature.
- The formation of mud-cracks during pre-oxidation of SSA TBCs makes lesser erosion resistance than YSZ.

CHAPTER 8

8 CONCLUSIONS

Following are the salient features of the present investigations,

8.1 Oxidation studies of SSA and YSZ TBCs

Both SSA and YSZ TBCs were developed on NiCrAlY bond-coated Inconel 718 superalloy substrate using APS technique. TGOs with different thicknesses were prepared at 1050 ºC for different pre-oxidation duration and the oxidation behavior was studied at 1100 ºC for 15 h in air. The main conclusions of oxidation study are as follows:

1. The initially formed SSA TGOs predominantly consists of α-Al_2O_3 and increasing growth of TGO was observed with an increasing pre-oxidation time at 1050 ºC.
2. The increase in pre-oxidation time led to the increase in microstructural defects in the SSA top ceramic layer at 1050 ºC. The Young's modulus and hardness of the coatings decreased with an increasing pre-oxidation time and highest percentage (50%) of elastic recovery was found for 30 h pre-oxidized SSA TBCs.
3. The newly developed SSA TBCs showed 65% lower weight gain as compared to conventional YSZ TBCs after oxidation study at 1100 ºC in air due to highly enriched α-Al_2O_3 at the bond coat and top coat interface.
4. The threshold TGO thickness of SSA TBCs is about 5.3 to 5.8 µm over which the parabolic oxidation rate increases with the increase in TGO thickness.
5. Failure of SSA TBCs occurred near the TGO and top coat interface due to the formation of $SmAlO_3$.

8.2 Electrochemical impedance behavior of oxidized SSA TBCs

The microstructures of top coat and TGO have been studied after pre-oxidation and oxidation processes with the help of EIS. Based on the experimental observations the following conclusions are made:

1. After pre-oxidation there is an initial decrease in resistance of SSA top coat (R_{SSA}) and increase in capacitance was observed from 10, 20 and 30 h due to increase in the percentage of defects of about 13, 29 and 45, respectively at 1050 ºC.

2. The increase in pre-oxidation duration caused a gradual increase in TGO growth. The high resistivity of TGO (1.72×10^{8} Ohm cm) was found at 20 h of pre-oxidation.

3. The growth of SSA TGO during pre-oxidation and oxidation treatment was inversely proportional to the capacitance in the presence of highly enriched α-Al_2O_3 at the interface.

4. The impedance response of SSA top coat and TGO vanishes after oxidation at 1100 ºC for 10 h of pre-oxidized specimens as compared to 20 and 30 h due to the compositional change of pure α-Al_2O_3 TGO to more conductive $NiCr_2O_4$.

5. The polarization resistance of TGOs is more sensitive to compositional changes at the TGO-ceramic top coat interface during oxidation at 1100 ºC.

8.3 Hot corrosion study of SSA and YSZ TBCs in vanadates and chlorides environments at 700 and 900 ˚C

The hot corrosion study was conducted in molten mixtures of 50 wt.% Na_2SO_4 + 50 wt.% V_2O_5 and 90 wt.% Na_2SO_4 + 5 wt.% V_2O_5 + 5 wt.% NaCl environments at 700 and 900 ˚C. The high temperature erosion test was conducted in air jet erosion tester at an impingement angle of 30 and 90˚ for different testing temperatures of 200, 500, and 800 ˚C respectively. The main conclusions of the study are as follows:

1. The SSA TBCs showed 8-39% lower hot corrosion resistance than conventional YSZ in both the environments at elevated temperature.
2. Both the TBCs suffer a more severe attack in chloride environment at 900 ˚C. The SSA TBCs showed the formation of $SmVO_4$, SrV_2O_6 and $SrSO_4$ as major hot corrosion products in vanadate and chloride environments respectively.

3. Similarly YSZ TBCs also exhibited YVO_4 as hot corrosion product in both vanadates and chlorides environment due to leaching of Y_2O_3 stabilizer from YSZ.
4. The hot corrosion resistance of SSA TBCs improved 3 times higher in the presence of Mg and Ni inhibitor in vanadate environments at 900 ˚C by forming a stable $Ni_3V_2O_8$ phase at the surface.

8.4 High temperature erosion study of SSA and YSZ TBCs in vanadate and chloride environments at 700 and 900 ˚C

The high temperature erosion study was conducted on pre-oxidized SSA and YSZ TBCs at impingement angles of 30 and 90˚ for the temperatures of 200, 500 and 800 ˚C. The main conclusions of this study are as follows:

1. The pre-oxidized SSA TBCs exhibited 63, 30 and 32% more erosion rate than pre-oxidized YSZ TBCs at an angle of 30˚ impingement for 200, 500 and 800 ˚C respectively.
2. The erosion loss of as deposited SSA TBCs showed 43% lower than pre-oxidized SSA TBCs at 30˚ impingement at 800 ˚C.
3. The observed lower resistance of pre-oxidized SSA TBCs is mainly due to the formation of mud-cracks during pre-oxidation treatment.

Summary of the work

- The newly developed SSA TBCs exhibits 65% higher oxidation resistance than YSZ TBCs mainly due to the presence of enriched alumina TGO at the interface. The formation of mixed oxides makes YSZ TBCs less oxidation resistance than SSA TBCs at high temperatures.

- The impedance response of SSA TBCs was reduced significantly after oxidation test due to the compositional change of pure α-Al_2O_3 based TGO into more conductive $NiCr_2O_4$.

- The present study also shows that SSA based TBCs severely suffer by hot corrosion in vanadate and chloride environments at elevated temperatures. However, it shows better performance in the presence of combined inhibitors such as MgO + NiO.

- The formation of mud-cracks during pre-oxidation of SSA TBCs makes lesser erosion resistance than YSZ.

Scope for future work

1. Oxidation studies can be conducted on the same SSA TBCs system for extended period of time.
2. Compositionally graded thermal barrier coating can be developed using SSA + NiCrAlY to improve the erosion performance of ceramic top coat.

REFERENCES

Ajay, A. Raja, V.S., Sivakumar, G., and Joshi, S.V. (2015). "Hot corrosion behavior of solution precursor and atmospheric plasma sprayed thermal barrier coatings". *Corros. Sci.,* 98, 271-279.

Ahmadian, S., and Jordan, E.H., (2014). "Explanation of the effect of rapid cycling on oxidation, rumpling, micro-cracking and lifetime of air plasma sprayed thermal barrier coatings". *Surf. Coat. Technol.* 244, 109-116.

Afrasiabi, A. Saremi, M. and Kobayashi, A. (2008). "A comparative study on hot corrosion resistance of three types of thermal barrier coatings YSZ, YSZ+Al_2O_3 and YSZ/Al_2O_3." *Mat. Sci. Eng. A.,* 478(1-2), 264-269.

Ahmadi-pidani, Shoja-Razavi, R. Mozafariania, R. and Jamali, H. (2012). "Evolution of hot corrosion behavior of plasma sprayed ceria and yttria stabilized zirconia thermal barrier coatings in the presence of Na_2SO_4 + V_2O_5 molten salt". *Ceram. Int.,* 38(8), 6613-6620.

Ayvacıklı, M., Ege, A., Yerci, S., and Can, N., (2011). "Synthesis and optical properties of Er^{3+} and Eu^{3+} doped $SrAl_2O_4$ phosphor ceramic", *J. of Lumin.* 131(11), 2432-2439.

Amaral, S.T., and Muller, I.L., (1999). "Effect of silicate on passive films anodically formed on iron in alkaline solution as studied by electrochemical impedance spectroscopy", *Corrosion,* 55(1), 17-23.

Berndt, C.C., (1985). "Acoustic emission evaluation of plasma sprayed thermal barrier coatings". *J. Eng. Gas Turbine and Power* 107, 142-146.

Byeon, J. W., Jayaraj, B., Vishwewaraiah, S., Rhee, S., Desai, V. H., and Sohn, Y. H., (2005). "Non-destructive evaluation of degradation in multi-layered thermal barrier coatings by electrochemical impedance spectroscopy", *Mat. Sci. Eng. A,* 407(1), 213-225.

Bajpai, P., Das, A., Bhattacharya, P., Madayi, S., Kulkarni, K., and Omar, S., (2015). "Hot corrosion of stabilized zirconia thermal barrier coatings and the role of Mg inhibitor*". J. Am. Ceram. Soc.*, 98(8), 2655-2661.

Baskaran, T. and Arya, S.B. (2017). "Role of thermally grown oxide and oxidation resistance of samarium strontium aluminate based air plasma sprayed ceramic thermal barrier coatings". *Surf. Coat. Technol.* 376, 299-309.

Baskaran, T. and Arya, S.B. (2018). "Influence of ceramic top coat and thermally grown oxide microstructures of air plasma sprayed $Sm_2SrAl_2O_7$ thermal barrier coatings on the electrochemical impedance behavior", *Surf. Coat. Technol.* doi.org/10.1016/j.surfcoat.2018.03.058

Batista, C., Portinha, A., Riberiro, R.M., Teixerira, V., and Oliveira, C.R., (2006). "Evaluation of laser glazed plasma sprayed thermal barrier coatings under high temperature exposure to molten salts". *Surf. Coat. Technol.*, 200(24), 6783-6791.

Bertrand, G., Bertrand, P., Roy, P., Rio, C., and Mevrel, R. (2008). "Low conductivity plasma sprayed thermal barrier coating using hollow PSZ spheres: Correlation between thermo-physical properties and microstructure". *Surf. Coat. Technol.* 202(10), 1994-2001.

Chen, X., Zhao, Y. Gu, L. Zou, B. Wang, Y. and Cao, X. (2011). "Hot corrosion behavior of plasma sprayed YSZ/$LaMgAl_{11}O_{19}$ composite coatings in molten sulfate-vanadate salt". *Corros.Sci.* 53(6), 2335-2343.

Chen, W.L., Liu, M., and Zhang, J.F., (2016). "Impedance analysis of 7YSZ Thermal barrier coatings during high-temperature oxidation". *J. Therm. Spray. Technol.*, 25 (8), 1596-1603.

Chen, W. R., Archer, R. and Huang, X., and Marple, B.R. (2008)."TGO Growth and Crack Propagation in a Thermal Barrier Coating". *J. Therm. Spray Technol.* 17(5-6), 858-864.

Cao, X.Q., Vassen, R. and Stover, D. (2004). "Ceramic materials for thermal barrier coatings". *J. Eur. Ceram. Soc.* 24(1), 1-10.

Cao, X.Q., Vassen, R., Jungen, W., Schwartz, S., Tietz, F., and Stöver, D., (2001). **"**Thermal stability of lanthanum zirconate plasma-sprayed coating", *J. Am. Ceram. Soc.* 84(9), 2086-2090.

David, R.S., Paul, M. and Yuriy, A.M. (2000)."Metallic article having a thermal barrier coating and a method of application". *U. S. Patent,* 6,025,078.

Darolia, R., (2003). "Post-deposition oxidation of a nickel-base superalloy protected by a thermal barrier coating". U.S. Patent 6,607,611.

Dong, H., Yang, G.J. Li, C.X. Luo, X.T. and Li, C.J. (2014). "Effect of TGO thickness on thermal cyclic lifetime and failure mode of plasma-sprayed TBCs". *J. Am. Ceram. Soc.,* 97(4), 1226-1232.

Dai, H., Zhong, X., Li, J., Meng, J., and Cao, X., (2006). "Neodymium-cerium oxide as new thermal barrier coating materials". *Surf. Coat. Technol.,* 201(6), 2527-2533.

Dong, H., Ren, Y., Wang, D., Li, X., Bai, Y., Wang, J., and Ma, W. (2014). "Hot corrosion behavior of $SrZrO_3$ ceramic co-doped with Y_2O_3 and Yb_2O_3 in molten Na_2SO_4, V_2O_5 and Na_2SO_4+V_2O_5 salts mixture". *J. Eur. Ceram. Soc.,* 34(15), 3917-3924.

Dong, H., Ren, Y., Wang, D., Li, X., Bai, Y., Wang, J., and Ma, W., (2014). "Hot corrosion behaviors of $SrZrO_3$ ceramic co-doped with Y_2O_3 and Yb_2O_3 in molten Na_2SO_4, V_2O_5 and Na_2SO_4+V_2O_5 salts mixture". *J. Eur. Ceram. Soc.* 34(15), 3917-3924.

Du, H., Shin, J. H., and Lee, S. W. (2005). "Study on porosity of plasma sprayed coatings by digital image analysis method". *J. Therm. Spray. Technol.* 14(4) 453-461.

Dwivedi, G., Viswanathan, V., Sampath, S., Shyam, A., and Lara-Curzio, E. (2014). "Fracture toughness of plasma-sprayed thermal barrier ceramics: Influence of processing, microstructure, and thermal aging". *J. Am. Ceram. Soc.* 97(9), 2736-2744.

Eliaz, N., Shemesh, G., and Latanision, R.M. (2002). "Hot corrosion of gas turbine components". *Eng. Fail. Anal.*, 9(1), 31-43.

Escribano, P., Marchal, M., Sanjuan, M.L., Gutierrez, P.A., Julian B., and Cordoncillo, E., (2005). "Low-temperature synthesis of $SrAl_2O_4$ by a modified sol–gel route: XRD and Raman characterization". *J. Solid State Chem.* 178(6), 1978-1987.

Evans, A.G., Gulden, M.E., and Rosenblatt, M.E. (1978). "Impact damage in brittle materials in the elastic-plastic response regime". *Proc. R. Soc. A*, 361(1706), 343.

Evans, A.G., Mumm, D.R. Hutchinson, J.W. Meier, G.H. and Petit, F.S. (2001). "Mechanisms controlling the durability of thermal barrier coatings". *Prog. Mater. Sci.*, 46(5), 505-553.

Feng, J., Xiao, B. Zhou, R. Pan, W. and Clarke, D.R. (2012). "Anisotropic elastic and thermal properties of the double perovskite slab–rock salt layer $Ln_2SrAl_2O_7$ (Ln = La, Nd, Sm, Eu, Gd or Dy) natural superlattice structure". *Acta Mater.* 60 (8), 3380-3392.

Feng, Z., and Frankel, G. S. (2016). "Evaluation of coated Al alloys using the break point frequency method", *Electrochim. Acta*, 187, 605-615.

Fletcher, J.G., West, A.R., and Irvine, J.T.S., (1995). "The AC-impedance response of the physical interface between yttria-stabilized zirconia and $YBa_2Cu_3O_7$-x". *J. Electrochem. Soc.* 142 (8), 2650-2654.

Fox, A.C., and Clyne, T.W., (2004). "Oxygen transport by gas permeation through the zirconia layer in plasma sprayed thermal barrier coating". *Surf. Coat. Technol.* 184 (2), 311-321.

Gale, W.F., and Totemeir, T.C. (2008). “Smithell metal reference book, eighth ed., Elsevier, Burlington, USA.

Gomez-García, J., Rico, A., Garrido-Maneiro, M.A., Munez, C.J., Poza P., and Utrilla, V., (2009). “Correlation of mechanical properties and electrochemical impedance spectroscopy analysis of thermal barrier coatings”. *Surf. Coat. Technol*. 204 (6), 812-815.

Golosnoy, I.O., Cipitria, A., and Clyne, T.W. (2009). “Heat transfer through plasma-sprayed thermal barrier coatings in gas turbines: A Review of recent work.” *J. Therm. Spray Technol.,* 18(5-6), 809-821.

Gillet, E., and Ealet, B. (1992). “Characterization of sapphire surfaces by electron energy loss spectroscopy”. *Surf. Sci.,* 273(3), 427-436.

Guo, S., and Yutaka, K., (2004). “Young's moduli of zirconia top-coat and thermally grown oxide in a plasma-sprayed thermal barrier coating system”. *Scr. Mater.* 50(11), 1401-1406.

Guo, H.B., Vaβen, R., and Stöver, D., (2004) “Atmospheric plasma sprayed thick thermal barrier coatings with high segmentation crack density”, *Surf. Coat. Technol.* 186 (3), 353-363.

Guo, H. B., Kuroda, S., and Murakami, H., (2006). “Microstructure and properties of plasma-sprayed segmented thermal barrier coatings”. *J. Am. Ceram. Technol.* 89(4), 1432-1439.

Greskovich, C. (1970). “Kinetics of $NiCr_2O_4$ formation and diffusion of Cr^{3+} ions in NiO”. *J. Amer. Ceram. Soc.* 53(9) 198-502.

Habibi, M.H., Wang, L. Liang, J. and Guo, S.M. (2013). “An investigation of hot corrosion behavior of YSZ-Ta_2O_5 in Na_2SO_4+V_2O_5 salt at 1100 ºC”. *Corros. Sci.* 75, 409-414.

Harada, S., Ikeda, Y., Mizuta, Y., Sugita, Y., and Ito, A., (1995). "The inspection of delaminated defects in ZrO_2 coated materials by infrared thermography techniques, Proceedings of the 1st Symposium on Thermographic NDT and E Techniques Symposium". 47-52.

Huang, H., Liu, C., Ni L., and Zhou, C., (2011). "Evaluation of microstructural evolution of thermal barrier coatings exposed to Na_2SO_4 using impedance spectroscopy". Corros. Sci., 53 (4), 1369-1374.

Habibi, M.H., Wang, L. and Guo, S.M. (2012)."Evolution of hot corrosion resistance of YSZ, $Gd_2Zr_2O_7$ and $Gd_2Zr_2O_7$+YSZ composite thermal barrier coatings in Na_2SO_4+V_2O_5 at 1050 ˚C". *J. Eur. Ceram. Soc.*, 32(8), 1635-1642.

Habibi, M.H., Wang, L. Liang, J. and Guo, S.M. (2013). "An investigation of hot corrosion behavior of YSZ-Ta_2O_5 in Na_2SO_4+V_2O_5 salt at 1100 ºC". *Corros. Sci.* 75, 409-414.

Habibi, M.H., Wang, L. and Guo, S.M. (2012)."Evolution of hot corrosion resistance of YSZ, $Gd_2Zr_2O_7$ and $Gd_2Zr_2O_7$+YSZ composite thermal barrier coatings in Na_2SO_4+V_2O_5 at 1050 ˚C."*J. Eur. Ceram. Soc.*, 32(8), 1635-1642.

Habibi, M.H. Yang, S., and Guo, S.M. (2014). "Phase stability and hot corrosion behavior of ZrO_2–Ta_2O_5 compound in Na_2SO_4–V_2O_5 mixtures at elevated temperatures."*Ceram. Int.* 40 (3), 4077-4083.

Hecht, D.L., Rohrmann, K., Stocker, T., and Thiel, W. (2007). "XPS investigations of ink-jet printed paper". *Surf. Interface Anal.*, 2007, 39(11), 845-851.

Jamali, H. Mozafarinia, R. Shoja-Razavi, R. and Ahmadi-Pidani, R. (2014). "Comparison of hot corrosion behavior of plasma sprayed nanostructured and conventional YSZ thermal barrier coatings exposure to molten vanadium and sodium sulfate". *J. Eur. Ceram. Soc.*, 34(2), 485-492.

Jayaraj, B., Desai, V.H., Lee, C.K., and Sohn, Y.H., (2004). "Electrochemical impedance spectroscopy of porous ZrO_2-8 wt.% Y_2O_3 and thermally grown oxide on nickel aluminide". *Mat. Sci. Eng. A*, 372(1), 278-286.

Jayaraj, B., Vishweswaraiah, S., Desai, V.H., and Sohn, Y.H., (2004). "Electrochemical impedance spectroscopy of thermal barrier coatings as a function of isothermal and cyclic thermal exposure". *Surf. Coat. Technol.* 177-178, 140-151.

Jones, R.L. (1997). "Some aspects of the hot corrosion of thermal barrier coatings". *J. Therm. Spray Technol.* 6(1-4), 77-84.

Janos, B.Z., Lugscheider, E., and Remer, P., (1999). "Effect of thermal aging on the erosion resistance of air plasma sprayed zirconia thermal barrier coating", *Surf. Coat. Technol.,* 113, 278-285.

Jones, R. L., and Williams, C.E. (1987). "Hot corrosion studies of zirconia ceramics". *Surf.Coat. Technol.* 32(5-6), 349-358.

Khajavi, M.R., and Shariat, M.H. (2004). "Failure of first stage gas turbine blades". *Eng. Fail. Anal.,* 11(4), 589-597.

Karaoglanli A.C., Ogawa, K., Turk, A., and Ozdemir, I., (2013). "Thermal Shock and cycling behavior of thermal barrier coatings (TBCs) used in gas turbines". Progress in Gas Turbine Performance, Dr. Ernesto Benini (Ed.), InTech, DOI: 10.5772/54412.

Karger, M., Vaβen, R., and Stöver, D., (2011). "Atmospheric plasma sprayed thermal barrier coatings with high segmented crack densities: Spraying process, microstructure and thermal cycling behavior". *Surf. Coat. Technol.,* 206(1), 16-23.

Konter, M., and Thumann, M., (2001). "Materials and manufacturing of advanced industrial gasturbine components". *J. Mater. Process Technol.* 117, 386-390.

Kimura, T., (2011). Molten salt synthesis of ceramic powders, advances in ceramics - synthesis and characterization, processing and specific Applications, Sikalidis, C., (Ed.), InTech, DOI: 10.5772/20472.

Kim, D.J., Cho, S.K., Choi, J.H., Koo, J.M., Seok, C.S., and Kim, M.Y. (2009). "Evaluation of the degradation of plasma sprayed thermal barrier coatings using nano-indentation". *Amer. Sci. Pub.,* 9(12), 7271-7277.

Keyvani, A., Saremi, M. and Sohi, M.H. (2011). "Oxidation resistance of YSZ-alumina composites compared to normal YSZ TBC coatings at 1100 ˚C". *J. Alloys and Compd.* 509(33), 8370-8377.

Kerby, R.C., and Wilson, J.R. (1973). "Solid-liquid phase equilibria for the ternary systems V_2O_5-Na_2O-Fe_2O_3, V_2O_5-Na_2O-Cr_2O_3, and V_2O_5-Na_2O-MgO". *Can. J. Chem.,* 51(7) 1032-1040.

Kulkarni, A., Vaidya, A., Goland, A., Sampath, S., and Herman, H., (2003). "Processing effects on porosity-property correlations in plasma-sprayed yttria stabilized zirconia coatings", *Mater. Sci. Eng. A,* 359(1), 100-111.

Kovacik, J., (1999). "Correlation between Young's modulus and porosity in porous materials", *J. Mat. Sci. Lett.* 18(13), 1007-1010.

Kumar, S., and Cocks, A.C.F. (2012). "Sintering and mud-cracking of EB-PVD thermal barrier coatings". *J. Mech. Phy. Sol.* 60 (4), 723-749.

Liu, H. F., Xiong, X. Li, X. B. and Wang, Y. L. (2014). "Hot corrosion behavior of Sc_2O_3–Y_2O_3–ZrO_2 thermal barrier coatings in presence of $Na_2SO_4 + V_2O_5$ molten salt". *Corros. Sci.* 85, 87-93.

Li, Y., Xie, Y., Huang, L., Liu, X., Liu, X., and Zheng, X. (2012). "Effect of physical vapour deposited Al_2O_3 film on TGO growth in YSZ/CoNiCrAlY coatings". *Ceram. Int.,* 38(6), 5113-5121.

Li, Y., Li, C.J. Zhang, Q. Yang, G.J. and Li, C.X. (2010). "Influence of TGO composition on the thermal shock lifetime of thermal barrier coatings with cold-sprayed MCrAlY bond coat". *J. Therm. Spray. Technol.*, 19(1-2), 168-177.

Li, S., Liu, Z.G. and Ouyang, J.H. (2010). "Hot corrosion behavior of $Yb_2Zr_2O_7$ ceramic coated with V_2O_5 at temperatures of 600 - 800 ˚C in air". *Corros. Sci.*, 52(10), 3568-3572.

Lin, Y., Yang, H., Zhu, J., Wang, F., and Luo, H., (2008). "Low temperature rapid synthesis of $LiNbO_3$ powder by molten salt methods, *Mater. Manuf. Process.* 23(8), 791-795.

Lee, S.Y., Chamberlin, R.M., and Spengler, C.J., (1978). "Control of corrosion in combustion turbines with Mg-Cr combined fuel additives" presented at the Winter Annual meeting of the ASME, San Francisco, Calif. Dec. 10-15, USA.

Leckie, R. M., Kramer, S., Ruhle, M., and Levi, C. G., (2005). "Thermochemical compatibility between alumina and ZrO_2–$GdO_{3/2}$ thermal barrier coatings, *Acta Mater.* 53 (11), 3281-3292.

Ma, W., Mack, D.E. Vaßen, R. and Stöver, D. (2008)."Perovskite-Type Strontium Zirconate as a New Material for Thermal Barrier Coatings". *J. Am. Ceram. Soc.* 91(8), 2630-2635.

Marcus, P., and Mansfeld, F., (2006) "Analytical methods in corrosion science and engineering, CRC press, Florida.

Matsumoto, M., Hayakawa, K. Kitaoka, S. Matsubara, H. Takayama, H. Kagiya, Y. and Sugita, Y. (2006)."The effect of pre-oxidation atmosphere on oxidation behavior and thermal cycle life of thermal barrier coatings". *Mat. Sci. Eng. A.*,441(1-2), 119-125.

May, W.R., Zetlmeisl, M.J., and Annand, R.R., (1974). “High temperature corrosion in gas turbines and steam boilers by fuel impurities”. III Evaluation of Magnesium as a corrosion, *J. of Engineering for Power.,* April, pp 124-128, USA.

May, W. R., Zetlmeisl, M. J., Annand, R. R., and Laurence, D. F. (1976). “High temperature corrosion in gas turbines and steam boilers by fuel impurities. III. Evaluation of the effects of manganese, calcium and several heavy metals on corrosion and slag formation”; in Symposium on heavy fuel oil additives, April, New York City, New York.

MacDonald, J.R., (1987), “Impedance spectroscopy-emphasizing solid materials and systems”, Wiley, New York.

Moskal, G., Swadźba, L., Hetmańczyk, M., Witala, B., Mendala, B., Mendala, J., and Sosnowy, P., (2012). “Characterization of the microstructure and thermal properties of $Nd_2Zr_2O_7$ and $Nd_2Zr_2O_7$/YSZ thermal barrier coatings”, *J. Eur. Ceram. Soc.* 32 (9), 2035-2042.

Mohan, P., Yuan, B., Patterson, T., Desai, V.H., and Sohn, Y.H. (2007). “Degradations of yttria stabilized zirconia thermal barrier coatings by vanadium pentoxide, phosphorous pentoxide, and sodium sulfate”. *J. Amer. Ceram. Soc.,* 90(11), 3601-3607.

Meetham, G.W. (1988). “Requirements for and factors affecting high temperature capability”. *Mater.Des.* 9(5), 244-252.

Miller, R.A. (1997). “Thermal barrier coatings for aircraft engines: History and directions”. *J. Therm. Spray Technol.* 6(1), 35-42.

Miller, R.A. (1987). “Current status of thermal barrier coatings-an overvview”, *Surf. Coat. Technol.* 30(1), 1-11.

Moskal, G., Swadźba, L., Hetmańczyk, M., Witala, B., Mendala, B., Mendala, J., and Sosnowy, P., (2012). “Characterization of the microstructure and thermal properties

of $Nd_2Zr_2O_7$ and $Nd_2Zr_2O_7$/YSZ thermal barrier coatings". *J. Eur. Ceram. Soc.,* 32(9) 2035-2042.

Moore, J.J. (1981). "Chemical Metallurgy", Butterworth and Co.

Nath, S., Manna, I. and Majumdar, J.D. (2014). "Kinetics and mechanism of isothermal oxidation of compositionally graded yttria stabilized zirconia (YSZ) based thermal barrier coating". *Corros. Sci.* 88, 10-22.

Ni, L.Y., Liu, C. Huang, H. and Zhou, C.G. (2011)."Thermal cycling behavior of thermal barrier coatings with HVOF NiCrAlY bond coat". *J. Therm. Spray. Technol.* 20 (5), 1133-1138.

Nijdam, T.J., and Sloof, W.G. (2006). "Combined pre-annealing and pre-oxidation treatment for the processing of thermal barrier coatings on NiCoCrAlY bond coatings". *Surf. Coat. Technol.,* 201(7), 3894-3900.

Nijdam, T.J., Jeurgens, L.P.H., Chen, J.H., and Sloof, W.G., (2005). "On the microstructure of the initial oxide grown by controlled annealing and oxidation on a NiCoCrAlY bond coating", *Oxid. Met.* 64 (5), 355-377.

Nicholls, J.R., Deakin, M.J. and Rickerby, D.S. (1999), "A comparison between the erosion behavior of thermal spray and electron beam physical vapor deposition thermal barrier coatings", *Wear,* 233, 352-361.

Otsuka, N., and Rapp, R.A. (1990). "Effect of chromate and vanadate anions on the hot corrosion of preoxidized Ni by a thin fused Na_2SO_4 film at 900°C." *J. Electrochem. Soc.* 137(1), 53-60.

Ochrombel, R., Schneider, J., Hildmann, B., and Saruhan, B., (2010). "Thermal expansion of EB-PVD yttria stabilized zirconia". *J. Eur. Ceram. Soc.,* 30(12), 2491-2496.

Ogawa, K., Ito, K. Shoji, T. Seo, D.W. Tezuka, H. and Kato, H. (2006). "Effects of Ce and Si addition to CoNiCrAlY bond coat materials on oxidation behavior and crack propagation of thermal barrier coatings". *J. Therm. Spray Technol.,* 15(4), 640-651.

Padture,N.P., Gell, M. and Jordan, E.H. (2002)."Thermal barrier coatings for gas-turbine applications". *Science*, 296(5566), 280-284.

Petrov, D., Angelov, B., and Lovchinov, V. (2010). "Sol-gel synthesis, surface and magnetic properties of nanocrystalline $SmAlO_3$". *J. Rare Earths,* 28 (4), 603-605.

Perez, N., (2004). "Electrochemistry and corrosion science", first ed., Kluwer Academic Publishers, New Delhi, 301-320.

Qu, Z., Wan, C. and Pan, W. (2012). "Thermo-physical properties of rare-earth stannates: Effect of pyrochlore structure". *Act. Mater.* 60(6-7), 2939-2949.

Qu, Z., Cheng, X., Wu, J., He, R., Pei, Y., and Fang, D., (2016). "An investigation on erosion behaviour of nanostructured 7YSZ coatings at elevated temperature", *Surf. Coat. Technol.,* 299, 129-134.

Reddy, N., Bera, P., Reddy, V.R., Sridhara, N., Dey, A,. Anandan, C., and Sharma, A.K. (2014). "XPS study of sputtered alumina thin films". *Ceram. Int.,* 40(17-18), 11099-11107.

Rangaraj, S., and Kokini, K. (2003). "Estimating the fracture resistance of functionally graded thermal barrier coatings from thermal shock tests". *Surf. Coat. Technol.* 173(2-3), 201-212.

Raghavan, S., Wang, H. Dinwiddie, R.B. Porter, W.D. Vaβen, R.Stöver,D. and Mayo, M.Y. (2004).Ta_2O_5/Nb_2O_5 and Y_2O_3 Co-doped Zirconia for Thermal Barrier Coatings."*J. Am. Ceram. Soc.* 87(3), 431-437.

Rahaman, M.N., Gross, J.R. Dutton, R.E. and Wang, H. (2006). "Phase stability, sintering, and thermal conductivity of plasma-sprayed ZrO_2–Gd_2O_3 compositions for potential thermal barrier coating applications". *Acta Mater.* 54(6), 1615-1621.

Ramesh, M.R., Prakash, S., Nath, S.K., Sapra, P.K., and Venkataramanan, B. (2010). Solid particle erosion of HVOF sprayed WC-Co/NiCrFeSiB coatings", *Wear*, 269, 197-205.

Rocca, E., Steinmetz, P., and Moliere, M. (2003). "Revisiting the inhibition of vanadium-induced hot corrosion in gas turbines". *J. Eng. Gas Turbines Power*, 125(3), 664-669.

Roth, R.S., Negas, T., and Cook, L.P. (1981). "System Na_2O-V_2O_5". Phase diagrams for ceramists, Vol. IV, p-89, Fig. 5127, Ed. G. Smith, The ceramic society, Columbus, OH.

Ropp, R.C., (2013). "Encyclopedia of alkaline earth compounds". Elsevier, 701-794.

Shipway, P.H., and Hutchings, I.M. (1996)."The role of particle properties in the erosion of brittle materials". *Wear*, 193(1), 105-113.

Sohn, Y.H., Lee, E.Y., Nagaraj, B.A., Biederman, R.R., and Sisson Jr, R.D., (2001). Microstructural characterization of thermal barrier coatings on high pressure turbine blades, *Surf. Coat. Technol.* 146-147, 132-139.

Song, S.-H., Xiao, P., and Weng, L.-Q., (2005). "Evaluation of microstructural evolution in thermal barrier coatings during thermal cycling using impedance spectroscopy". *J. Eur. Ceram. Soc.* 25 (7), 1167-1173.

Soboyejo, W.O., Mensah, P. Diwan, R, Crowe, J. and Akwaboa, S. (2011). "High temperature oxidation interfacial growth kinetics in YSZ thermal barrier coatings in NiCoCrAlY with 0.25 Hf". *Mat. Sci. Eng. A.*, 528(6), 2223-2230.

Su, Y.J., Trice, R.W. Faber, K.T. Wang, H. and Porter, W.D. (2004). "Thermal conductivity, phase stability, and oxidation resistance of $Y_3Al_5O_{12}$ (YAG)/Y_2O_3-ZrO_2(YSZ) thermal barrier coatings". *Oxid. Met.* 61(3-4), 253-270.

Sohn, Y.H.,Vaidyanathan, K.Ronski, M. Jordan, E.H. and Gell, M. (2001). "Thermal cycling of EB-PVD/MCrAlY thermal barrier coatings: II. Evolution of photo-stimulated luminescence". *Surf. Coat. Technol.* 146-147, 102-109.

Schulz, U., Menzebach, M., Leyens, C., and Yang, Y. Q. (2001). "Influence of substrate material on oxidation behavior and cyclic lifetime of EB-PVD TBC systems". *Surf. Coat. Technol.*146-147, 117-123.

Schütze, M. (2000). "Corrosion and environmental degradations". Vol. II, Wiley-VCH.

Sikalidis, C., (2011). "Advances in ceramics - synthesis and characterization, processing and specific Applications". InTech, ISBN-978-953-307-505-1, DOI: 10.5772/20472.

Shin, D., and Hamed, A. (2018), "Influence of micro-structure on erosion resistance of plasma sprayed 7YSZ thermal barrier coatings under gas turbine operating conditions", *Wear,* 396-397, 34-47.

Tan, Y., Srinivasan, V., Nakamura, T., Sampath, S., Bertrand, P., and Bertrand, G., (2012). "Optimizing compliance and thermal conductivity of plasma sprayed thermal barrier coatings via controlled powders and processing strategies", *J. Therm. Spray Technol.* 21 (5), 950-962

Tang, F., Ajdelsztajn, L. and Schoenung, J.M. (2004). "Characterization of oxide scales formed on NiCrAlY coatings with various oxygen contents introduced during thermal spraying". *Script. Mater.* 51(1), 25-29.

Tomimatsu, T., Kagawa, Y., and Zhu, S. J., (2003). "Residual stress distribution in electron beam-physical vapor deposited ZrO_2 thermal barrier coating layer by raman spectroscopy", *Metall. and Mater. Trans. A,* 34(8), 1739-1741.

Tsai, P.C., Lee, J.H. and Hsu, C.S. (2007). "Hot corrosion behavior of laser glazed plasma sprayed yttria stabilized zirconia thermal barrier coatings in the presence of V_2O_5." *Surf.Coat.Technol.,* 201(9-11), 5143-5147.

Tsai, P.C., Lee, J.H., and Chang, C.L., (2007). "Improving the erosion resistance of plasma sprayed zirconia thermal barrier coatings by laser glazing", *Surf. Coat. Technol.,* 202, 719-724.

Tiwari, S., and Prakash, S. (1998). "Literature review magnesium oxide as inhibitor of hot oil ash corrosion." *Mat. Sci. Technol.,* 14(5) 467-472.

Toscano, J., Vaßen, R, Gil, A., Subanovic, M., Naumenko, D., Singheiser, L., and Quadakkas, W.J. (2006). "Parameters affecting TGO growth and adherence on *M*CrAlY-bond coats for TBC's". *Surf. Coat. Technol.* 201(7), 3906.

Uzun, A., Cevik, I. and Akcil, M. (1999). "Effect of thermal barrier coatings on a turbocharged diesel engines performance". *Surf. Coat. Technol.* 116(119), 505-507.

Vakilifard, H., Ghasemi, R., and Rahimipour, M. (2017). "Hot corrosion behavior of plasma sprayed functionally graded thermal barrier coatings in the presence of $Na_2SO_4 + V_2O_5$ molten salt". *Surf. Coat. Technol.,* 326, 238-246.

Vaβen, R., Cao, X. Tietz, F. Basu, D. and Stöver, D. (2000). "Zirconates as new materials for thermal barrier coatings". *J. Amer. Ceram. Soc.,* 83, 2023-2028.

Vaßen, R., Jarligo, M.O. Steinke, T. Mack, D.E. and Stöver, D. (2010)."Overview on advanced thermal barrier coatings". *Surf.Coat. Technol.* 205(4), 938-942.

Vassen, R., Cao, X., Tietz, F., Basu, D., and Stöver, D., (2000). "Zirconates as new materials for thermal barrier coatings". *J. Am. Ceram. Soc.,* 83, 2023-2028.

Vasquez, R.P. (1991). "X-ray photoelectron spectroscopy study of Sr and Be compounds". *J. Electron. Spectrosc. Relat. Phenom.*, 56(3), 217-240.

Wagner, C.D., Riggs, W.M., Davis, L.E., Moulder, J.F., and Mullenberg, G.E. (1979). "Handbook of X-ray photoelectron spectroscopy." Minnesota.

Wada, S., Ritter, J.E., (Ed.). (1992). "Erosion of ceramic materials." 71 Tech Publications, Zurich.

Wan, C., Sparks, T.D., Pan, W., and Clarke, D.R., (2010). "Thermal conductivity of the rare-earth strontium aluminates". *J. Amer. Ceram. Soc.,* 93(5) 1457-1460.

Wang, T.X., and Chen, W.W. (2008). "Solid phase preparation of submicron-sized $SrTiO_3$ crystallites from SrO nanoparticles and TiO_2 powders". *Mater. Lett.,* 2008, 62(17-18) 2865-2867.

Wang, Z., Kulkarni, A., Deshpande, S., Nakamura, T., and Herman, H., (2003). "Effect of pores and interfaces on effective properties of plasma sprayed zirconia coatings", *Acta Mater.* 51 (18), 5319-5334.

Wang, X., Mei, J., and Xiao, P., (2001). "Determining oxide growth in thermal barrier coatings (TBCs) non-destructively using impedance spectroscopy", *J. Mat. Sci. Lett.* 20 (1), 47-49.

Wellman, R.G., and Nicholls. (2004). "On the effect of ageing on the erosion of EB-PVD TBCs". Surf. Coat. Technol., 177-178, 80-88.

Weimer, M.J., Nagaraj, B.A., Schaeffer, J.C., and Heaney, J.A. (2003). "Pre-service oxidation of gas turbine disks and seals". U.S. Patent 6,532,657.

Wortman, D.J., Nagaraj, B.A. and Duderstadt, E.C. (1989)."Thermal barrier coatings for gas turbine use". *Mater. Sci. Eng. A,* 121(2), 433-440.

Wu, J., Wei, X.Z. Padture, N.P. Klemens, P.G. Gell. M. Garcia. E. Miranzo. P., and Osendi, M.I. (2002). "Low thermal conductivity rare earth zirconates for potential thermal barrier coating applications". *J. Am. Ceram. Soc.* 85(12), 3031-3035.

Wu, Y.N., Qin, M., Feng, Z.C., Liang, Y., Sun, C., and Wang, F.H. (2003). "Improved oxidation resistance of NiCrAlY coatings". *Mat. Lett.* 57(16-17), 2404-2408.

Weiderhorn, S.M., Hockey, B.J. (1983). "Effect of material parameters on the erosion resistance of brittle materials". *J. Mat. Sci.* 18(3), 766-780.

Xie, X., Guo, H. Gong, S.and Xu, H. (2011). "Thermal cycling behavior and failure mechanism of $LaTi_2Al_9O_{19}$/YSZ thermal barrier coatings exposed to gas flame". *Surf. Coat. Technol.* 205(17-18), 4291-4298.

Xialong, C., Yu, Z. Lijion, G. Binglin, Z. Ying, W., and Xueqiong, C. (2011). "Hot corrosion behavior of plasma sprayed YSZ/$LaMgAl_{11}O_{15}$ composite coatings in molten sulfate-vanadate salt". *Corros. Sci.* 53, 2335-2343.

Xu, Z., He, L., Mu, R., He, S., Huang, G., and Cao, X. (2010). "Hot corrosion behavior of rare earth zirconates and yttria partially stabilized zirconia thermal barrier coatings". *Surf. Coat. Technol.*, 204(21-22) 3652-3661.

Yuan, F. H., Chen, Z. X., Huang, Z. W., Wang, Z. G., and Zhu, S. J., (2008). "Oxidation behavior of thermal barrier coatings with HVOF and detonation-sprayed NiCrAlY bond coats", *Corros. Sci.* 50 (6), 1608-1617.

Yamanaka, S., Kurosaki1, K. Oyama, T. Muta, H. Uno, M. Matsuda, T. and Kobayashi, S.I. (2005)."Thermophysical Properties of Perovskite-Type Strontium Cerate and Zirconate". *J. Am. Ceram. Soc.* 88 (6), 1496-1499.

Zhang, J., and Desai, V., (2005), "Evaluation of thickness, porosity and pore shape of plasma sprayed TBC by electrochemical impedance spectroscopy". *Surf. Coat. Technol.* 190 (1) 98-109.

Zhang, F., Evertsson, J., Bertram, F., Rullik, L., Carla, F., Langberg, M., Lundgren, E., and Pan, J., (2017). "Integration of electrochemical and synchrotron-based X-ray techniques for in-situ investigation of aluminium anodization", *Electrochim. Acta,* 241, 299-308.

Zhao, S., Zhao, Y., Zou, B., Fan, X., Xu, J., Hui, Y., Zhou, X., Liu, S., and Cao, X., (2014). "Characterization and thermal cycling behavior of $La_2(Zr_{0.7}Ce_{0.3})_2O_7$/8YSZ functionally graded thermal barrier coating prepared by atmospheric plasma spraying", *J. Alloy. Compd.* 592 109-114.

Zhao, H., Begley, M.R., Heuer, A., Moshtaghin, R.S., and Wadley, H.N.G., (2011). "Reaction, transformation and delamination of samarium zirconate thermal barrier coatings", *Surf. Coat. Technol*. 205(19), 4355-4365.

Zhao, S., Li, Q., Wang, L., and Zhang, Y. (2006). "Molten salt synthesis of lead lanthanum zirconate titanate stannate powders and ceramics". *Mater. Lett.,* 60(3), 425-430.

Zhong, X.h., Wang, Y.M. Xu, Z.H. Zhang, Y.H. Zhang, J.H. and Cao, X.Q. (2010). "Hot corrosion behaviors of overlay-clad yttria stabilized zirconia coatings in contact with vanadate-sulfate salts." *J. Eur. Ceram. Soc.,* 30(6), 1401-1408.

Zhou, X., Xu, Z., He, L., Xu, J., Zou, B., and Cao, X. (2016). "Hot corrosion behavior of $LaTi_2Al_9O_{19}$ ceramic exposed to vanadium oxide at temperatures of 700–950 ˚C in air". *Corros. Sci.,* 104, 310-318.

Zhu, D., Lin, H.T., Zhou, Y., Widjaja, S., and Singh, D. (2011). "Advanced ceramic coatings and materials for extreme environments". Wiley, ISBN: 978-1-118-05988-3.

Zvereva, I., Smirnov, Yu., Gusarov, V., Popova, V., Choisnet, J., (2003). "Complex aluminates $RE_2SrAl_2O_7$ (RE=La, Nd, Sm-Ho): Cation ordering and stability of the double perovskite slab-rocksalt layer P_2/RS intergrowth", *Solid state Sci.* 5(2), 343-349.

Zvereva, I. A., Popova, V. F., Pylkina, N. S., Gusarov, V. V., (2003). "Kinetics of ruddlesden-popper phase formation: II. Mechanism of $Nd_2SrAl_2O_7$ and $Sm_2SrAl_2O_7$ formation", *Russ. J. Gen. Chem.* 73 (5), 43-47.

List of Publications based on the Ph.D. Research Work

Sl.No	Title of the paper	Authors name (In the same order as in the paper, underline the research scholar's name	Name of the Journal / Conference / Symposium, Vol., No., Pages	Month & Year Of Publication	Category*
1	Influence of ceramic top coat and thermally grown oxide microstructures of air plasma sprayed $Sm_2SrAl_2O_7$ thermal barrier coatings on the electrochemical impedance behavior	Baskaran T, Shashi Bhushan Arya	Surf. Coat. Technol. doi.org/10.1016/j.surfcoat.2018.03.058	April, 2018	1
2	Role of thermally grown oxide and oxidation resistance of Samarium Strontium Aluminate based air plasma sprayed ceramic thermal barrier coatings	Baskaran T, Shashi Bhushan Arya	Surf. Coat. Technol., 326 (2017) 299-309.	July, 2017	1
3	The impact of thermally grown oxide growth on the oxidation resistance of $Sm_2SrAl_2O_7$ based air plasma sprayed ceramic thermal barrier coatings	Baskaran T, Shashi Bhushan Arya	Indian Institute of Metals, NMD ATM 2017	November, 2017	4
4	Fabrication of samarium strontium aluminate ceramic and deposition of thermal barrier coatings by air plasma spray process	Baskaran T, Shashi Bhushan Arya	MATEC web of conferences, RiMES 2017, Manipal	December, 2017	3
5	Evaluation of microstructural changes and thermally grown oxide growth of oxidized $Sm_2SrAl_2O_7$ ceramic thermal barrier coatings for gas turbine applications	Baskaran T, Shashi Bhushan Arya	p. 106, Indian ceramic society International conference, (EH-TACAG'17), Pune	December, 2017	4

Category*

1 : Journal paper, full paper reviewed 2 : Journal paper, Abstract reviewed

3 : Conference/Symposium paper, full paper reviewed 4 : Conference/Symposium paper, abstract reviewed

5 : Others (including papers in Workshops, NITK Research Bulletins, Short notes etc.)

Name: Baskaran. T
Research Scholar
Department of Metallurgical and Materials Engineering
National Institute of Technology Karnataka Surathkal,
Mangaluru-575 025, Karnataka, India
Email: baskarannitk@gmail.com
Cell: +91-8747925955

Educational Qualifications			CGPA
Ph.D. (Metallurgical and Materials Engg.)	**NIT K, Surathkal**	**2014-2018**	**9.33**
M.Tech: Process Metallurgy	**NIT K, Surathkal**	**2014**	**8.69**
BE: Mechanical Engineering	**Anna University of Technology, Tiruchirappalli**	**2012**	**8.87**

Publications

1. **Baskaran T,** Shashi Bhushan Arya, Influence of ceramic top coat and thermally grown oxide microstructures of air plasma sprayed $Sm_2SrAl_2O_7$ thermal barrier coatings on the electrochemical impedance behaviour, Surf. Coat. Technol. 344 (2018) 601-613.
2. **Baskaran T,** Shashi Bhushan Arya, "Role of Thermally Grown Oxide and Oxidation Resistance of Samarium Strontium Aluminate based Air Plasma Sprayed Ceramic Thermal Barrier Coatings" Surf. Coat. Technol., 326 (2017) 299-309.
3. A. Gupta, A. Kumar, **T. Baskaran,** S.B. Arya, R.K. Khatirkar, Effect of heat input on microstructure and corrosion behaviour of duplex stainless steel shielded metal arc welding, Trans. Ind. Ins. Met. 2018, doi.org/10.1007/s12666-018-1294-z

4. Vishal Vats, **Baskaran T,** Shashi Bhushan Arya, "Tribo-corrosion study of nickel free, high nitrogen and high manganese austenitic stainless steel" Tribology International, 119 (2018) 659-666.
5. **Baskaran T,** Shashi Bhushan Arya, "Fabrication of Samarium Strontium Aluminate Ceramic Powder and Deposition of Thermal Barrier Coatings by Air Plasma Spray Process" MATEC Web of Conferences, 144 (2018), 02001. doi.org/10.1051/matecconf/201814402001
6. Gosipathala Sreedhar, A. Sivanantham, **T. Baskaran,** S. Vengatesan, and L. John Berchmans, Lithiated sarcosine templated synthesis of single crystalline $SrTiO_3$ nanocubes via hydrothermal method. Mater. Lett. 133 (2014) 127-131.
7. **T. Baskaran**, Gosipathala Sreedhar, S.B. Arya, "Hot corrosion stability of double perovskite and pyrochlore in sulfate solution of vanadates or chlorides at 900 ºC" Mater. Sci. Forum, 830-831 (2015), 695-698.

Conferences attended

1. **Baskaran T,** Shashi Bhushan Arya, "Evaluation of microstructural changes and thermally grown oxide growth of oxidized $Sm_2SrAl_2O_7$ ceramic thermal barrier coatings for gas turbine applications" International conference on Expanding Horizons of Technological Applications of Ceramics and Glasses (EH-TACAG'17), 14-16 December, College of Engineering, Pune, India **(Best poster award).**
2. **Baskaran T,** Shashi Bhushan Arya, "The impact of thermally grown oxide growth on the oxidation resistance of samarium strontium aluminate based air plasma sprayed ceramic thermal barrier coatings". NMD-ATM 2017, 11-14 November, Goa, India.
3. **Baskaran T,** Shashi Bhushan Arya, "Fabrication of Samarium Strontium Aluminate Ceramic Powder and Deposition of Thermal Barrier Coatings by Air Plasma Spray Process" International Conference on Research in Mechanical Engineering Sciences (RiMES 2017), 21-23 December, 2017, Manipal University, India.

4. **T. Baskaran,** G., S.B. Arya "Hot corrosion stability of double perovskite and pyrochlore in sulfate solution of vanadates or chlorides at 900 °C", ICAMPS 2015,Trivandrum
5. **Baskaran, T.,** Sreedhar, G., and S.B. Arya, "Hot corrosion of advanced ceramic oxides in gas turbine simulated environments at 900 ºC", CORCON 2014, Mumbai.
6. **T. Baskaran,** Shashi Bhushan Arya, Gosipathala Sreedhar, Hot corrosion behavior of $SrTiO_3$ perovskite in Na_2SO_4+50 wt.% V_2O_5 at 900 ºC. "International Corrosion Prevention Symposium for Research Scholars (CORSYM 2014)" 20-21 February 2014, IIT Bombay, India.

Awards/Recognition

1. **Instiutute 3rd rank in M.Tech (Process Metallurgy)** during Academic year 2012-2014, NIT K, Surathkal, Karnataka.
2. **University rank holder in BE (Mechanical Engineering)** during Academic Year 2009-2012, Anna University, Chennai, Tamilnadu.
3. **GATE Scholarship**, MHRD, Government of India (2012-2014).

Instruments/Machines handling

X-ray diffractometer, FTIR, Optical Microscopy, IC Engine Overhauling/assembling, Tensile, Impact, Hardness, Fatigue and CNC Machines.

Reference

Dr. Shashi Bhushan Arya
Assistant professor
Dept. of Metallurgical & Materials Engineering
National Institute of Technology Karnataka, Surathkal
Mangaluru, Karnataka-575 025, India
Email: sbhushanarya@gmail.com
Tel: +91-824-2473754; Mobile: +91-8762526500

Declaration

I hereby solemnly declare that all the information mentioned above is true and correct according to my knowledge.

Baskaran T